BERGISCHE
UNIVERSITÄT
WUPPERTAL

JÜLICH
FORSCHUNGSZENTRUM

Enhancing the Signal Interpretation and Microscopical Hardware Concept of 3D Polarized Light Imaging

Dissertation zur Erlangung des Doktorgrades:

Dr. rer. nat.

Fakultät für Mathematik und Naturwissenschaften
Bergische Universität Wuppertal

vorgelegt von:

Hendrik Wiese

August 2016

Prof. Dr. Uwe Pietrzyk

Dr. Markus Axer

Die Dissertation kann wie folgt zitiert werden:

urn:nbn:de:hbz:468-20170313-100800-9
[http://nbn-resolving.de/urn/resolver.pl?urn=urn%3Anbn%3Ade%3Ahbz3A468-20170313-100800-9]

Abstract

Three Dimensional Polarized Light Imaging (3D-PLI) is a neuroimaging technique that is used to study the structural connectivity of the human brain at the meso- and microscale. In 3D-PLI, the complex nerve fiber architecture of the brain is modeled by 3D orientation vector fields that are derived from polarimetric measurements of unstained histological brain sections.
In this thesis, a new algorithmic framework for an unbiased data interpretation of the polarimetric measurements at the mesoscale has been developed. By extending standard 3D-PLI measurements to include data acquired with a tiltable specimen stage, this new framework facilitates an enhanced accuracy of reconstructed orientation vectors. In a proof of concept study the capabilities of the new algorithms were explored and it has been shown how these algorithms can be employed to investigate the fiber architecture of the human brain.
In order to extend the developed framework to the microscale, the second part of this thesis is dedicated to the implementation of an oblique illumination system for 3D-PLI microscopy. For this purpose, the optical setup of the illumination has been designed and optimized. A proof of concept measurement provided evidence that the acquired data is equivalent to that acquired with a tiltable specimen stage. With this new capability in 3D-PLI microscopy it is now possible to extend the application of developed algorithms to the microscale and facilitate even more complex data analytics in the future.

Kurzzusammenfassung

3D Polarized Light Imaging (3D-PLI) ist ein bildgebendes Verfahren, das in den Neurowissenschaften benutzt wird um die anatomische Konnektivität des (menschlichen) Gehirns auf mesoskopischer und mikroskopischer Auflösung zu studieren. Dazu wird in 3D-PLI die komplexe Nervenfaserarchitektur des Gehirns durch 3D Vektorfelder modelliert, die auf Basis polarimetrischer Messungen von ungefärbten histologischen Gehirnschnitten berechnet werden.
In dieser Arbeit sind Algorithmen entwickelt worden, die eine unabhängige Datenanalyse der polarimetrischen Messungen auf der Mesoskala ermöglichen. Durch die Ergänzung der standardisierten 3D-PLI Messkette um Messungen mit einem verkippten Probentisch ermöglichen diese Algorithmen eine höhere Genauigkeit bei der Bestimmung von Orientierungsvektoren. In einer Machbarkeitsstudie wurde untersucht, wie diese Algorithmen die Erforschung der Faserarchitektur des menschlichen Gehirns unterstützen.
Um die entwickelten Algorithmen auch im mikroskopischen Bereich nutzen zu können, wurde im zweiten Teil dieser Arbeit ein Beleuchtungssystem mit schiefem Lichteinfall für die 3D-PLI Mikroskopie entwickelt. Hierzu wurde der optische Aufbau des Beleuchtungssystems entworfen und optimiert. In einer Machbarkeitsstudie wurde nachgewiesen, dass dieses Beleuchtungssystem eine Datenbasis liefert, die äquivalent zu den Daten genutzt werden kann, die mit Hilfe des verkippbaren Probentisches im mesoskopischen Bereich gemessen werden. Durch diese neuen Methoden in der 3D-PLI Mikroskopie ist es nun möglich, die in dieser Arbeit entwickelten Algorithmen sowohl im mesoskopischen als auch im mikroskopischen Bereich zu nutzen und in zukünftigen Studien die Datenanalyse zu erweitern.

Contents

1

A short Introduction to Brain Mapping

The study of the human brain promises unprecedented insights into the working mechanisms of neural networks and their information processing capabilities. Understanding how brain function emerges from the structural organization of its building blocks may eventually yield applications in several fields ranging from healthcare to novel computing and interfacing technologies [31, 66, 79]. The modeling of the principles of information processing in neural networks has already led to significant advances in the field of machine learning especially in the area of pattern recognition [66, 47]. Current research is dedicated to developing and advancing computing architectures (e.g. neuromorphic computing architectures) in order to better emulate biological neural networks [80, 33]. Furthermore, a detailed knowledge of the brain's anatomy and the function of specific brain regions is critical for understanding and eventually treating neuro-degenerative diseases such as Parkinson's or Alzheimer's disease [31]. With the recent launch of the Human Brain Project in Europe [2] and the Brain Initiative in the US [55] these research goals have been acknowledged by the scientific community for their importance for society.
The main challenges of studying the human brain are due to its complexity and multi-

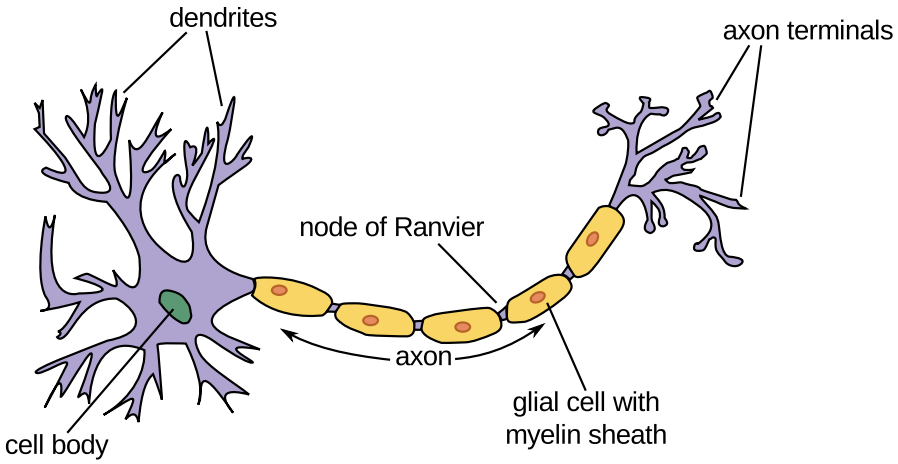

FIGURE 1.1: Sketch of a neuronal cell. The cell receives excitatory or inhibitory input at its dendrites. When a certain threshold is exceeded, it fires and an action potential propagates along the axon until it reaches the axon terminals, where the signal leads to the excitation or inhibition of other neurons. This figure was adapted from [1] and labeled according to [20].

scale organization. At the microscale, the brain is built-up of individual neurons, which are electrically excitable cells, each consisting of a cell body, dendrites and an axon (cf. Fig. 1.1). The primary function of the dendrites is to receive signals from other neurons whereas the axon allows the propagation of electro-chemical signals. Upon firing of a neuron, an electro-chemical pulse propagates along the axon by opening sodium ion channels in its membrane, which leads to a change in the membrane potential and opens further channels along the nerve fiber. On its own, the conduction velocity of this action potential is very slow. Thus, long ranged axons are typically insulated by glial cells, which allow Saltatory conduction [20]. These glial cells form a myelin sheath around the axon, which allows the action potential to occur only at the "nodes of Ranvier" between glial cells, where the signal is refreshed by opening new sodium ion channels. As the action potential propagates from node to node, the conduction velocity is increased by up to two orders of magnitude. When the action potential reaches the axon terminals, most synapses release neurotransmitters into the synaptic cleft, where they are detected by neuroreceptors at the dendrites of other neurons.
On a macroscopic level, the brain can be subdivided into the cerebral cortex (also called gray matter) and the subcortical white matter (which appears white in dissected brains due to its high myelin content). The cerebral cortex of the brain describes the outermost, $2\,\text{mm} - 4\,\text{mm}$ thick layer and consists mostly of cell bodies [20]. In the field of brain mapping, the brain's organization is typically described by a parcellation into distinct brain regions based on function and structure.
Brain function is typically studied by functional Magnetic Resonance Imaging (fMRI), which is based on the blood-oxygen-level-dependent (BOLD) response. When assigning specific tasks to a subject, the brain activity increases in brain regions that are relevant for the respective task, leading to an increased local energy consumption by brain cells which can be identified based on the BOLD contrast [51].
On a structural level, the cortex can be subdivided based on different features such as neuron density or the distribution of certain neuroreceptors [3, 81]. By cross referencing functional and structural mapping techniques, researchers aim to understand the link between the organization visible on a structural level and the respective function that is observed in vivo [21].
In general, even performing simple tasks requires the co-activation of multiple brain regions. Hence, it is critical not only to map brain regions but also to understand how they are connected to each other. Similar to the subdivision of the brain into different regions, *connectivity* can be studied on a functional and on a structural level. *Functional connectivity* is defined as the temporal co-activation of different brain regions and can be studied through fMRI.
The present study addresses an imaging modality for *structural connectivity*, i.e. the physical connection between different brain regions. These connections are analyzed to develop a comprehensive network model of the human brain called *connectome* [71], which includes connections ranging from large macroscopic fiber bundles down to single axon terminations in the cortex. Hence, studying structural connectivity of the (human) brain is a multiscale challenge, ranging across several orders of magnitude, from $10^2\,\text{mm}$ (approximate size of the human brain and long ranged interhemispheric connections) to $10^{-3}\,\text{mm}$ (the approximate diameter of an axon) or even $10^{-5}\,\text{mm}$ (the diameter of single neurofilaments within axons) [20]. A broad variety of imaging methods have been developed in order to investigate the fiber architecture of the brain at different scales.
So far, *diffusion weighted Magnetic Resonance Imaging (dMRI)* is the only means of imaging the course of fiber pathways in vivo. This technique is capable of measuring the orientation sensitive diffusion of water molecules. As the walls of nerve fibers impose

spatial restrictions on the diffusion, the orientation-dependent magnitude of diffusion makes it possible to infer orientations of fiber pathways. The highest spatial resolution achieved in dMRI measurements of complete human brains to date is 1.25 mm [75] in vivo, while for post mortem measurements even a sub-millimeter resolution has been achieved [52].

For any 3D imaging technique, the brain volume is virtually subdivided into volume elements called *voxels*. In *Diffusion Tensor Imaging (DTI)*, the connectome is represented by assigning a diffusion tensor to each of these voxels. These tensors are visualized by ellipsoids whose main axis indicate the predominant fiber orientation. Ellipsoids are well suited to visualize single fiber orientations (in cigar shaped ellipsoids) and to visualize the level of uncertainty the measurement is afflicted with (i.e. with increasing uncertainty the ellipsoids become more spherical).

It has been argued that the tensor is not sufficient to represent voxels that contain fibers oriented in two (or more) distinct orientations [73]. Due to the relatively coarse resolution of dMRI this issue is highly relevant, as in many voxels multiple fiber orientations are present. Hence, more complex measurement protocols such as *High-angular-resolution diffusion imaging (HARDI)* have been developed [73], representing the statistical distribution of fiber orientations by *orientation distribution functions (ODFs)* [74]. These ODFs make it possible to adequately quantify and visualize crossing fiber structures in every voxel.

For post mortem studies of the human connectome, several histological imaging methods have been developed. Myelin staining techniques such as the Luxol fast blue stain or the Heidenhain-Woelcke stain utilize the chemistry of the myelin sheath to bind dye particles and reveal the fiber architecture in histological sections [43, 78]. Histological sections with stained myelin are often used to validate other imaging techniques such as dMRI [48]. However, reconstructing a whole brain volume requires extensive image registration as shearing forces during the preparation procedure deform each brain section individually. Furthermore, myelin stains only offer the possibility to image the myelin density but not the actual orientation of nerve fibers. While it is possible to deduce the orientation of homogeneous fiber bundles based on the morphological features made visible in myelin stains, more complex structures cannot be thoroughly examined. For visualization purposes, structure tensor analysis can be applied to myelin stained sections in order to make the in-plane orientation more accessible [10].

Recently, Chung et al. have developed a protocol (called *CLARITY*) that makes it possible to transform opaque biological tissue into an optically transparent nanoporous hydrogel. By means of immunohistochemical labeling they were able to reveal detailed fiber connections in an unsectioned mouse brain [14]. In their study, the tissue sample was imaged by in-depth scanning the hydrogel hybridized and lipid free tissue with an optical microscope. To date, the maximal tissue thickness that can be analyzed with this approach is restricted to the $\approx 10\,\text{mm}$ regime due to the limited working distance of microscope objective lenses.

This study focuses on *3D Polarized Light Imaging (3D-PLI)*, a histological imaging technique that analyzes unstained brain sections and is capable of extracting 3D orientation vectors that model the brain's fiber architecture. 3D-PLI is primarily based on the birefringence of the myelin sheath, an optical effect that changes the polarization state of polarized light [67]. While the birefringence of nerve fibers has been known for almost a century, only the advances in digital image processing in recent years have made this method feasible for a comprehensive study of the connectome. Polarimetric measurements of unstained brain sections make it possible to deduce the three dimensional orientation of myelinated axons (a comprehensive introduction to the theory of polari-

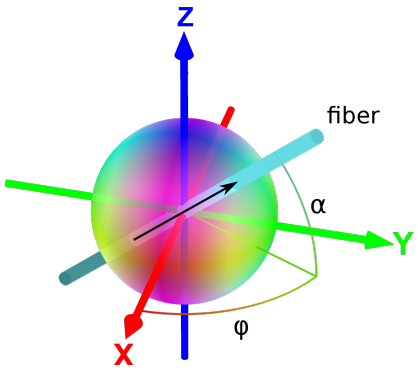

FIGURE 1.2: The 3D-PLI orientation vector for a nerve fiber can be represented in spherical coordinates by the inclination angle α and the direction angle φ. The color sphere shows how these orientations vectors can be visualized by color in order to make vector maps more accessible.

metric measurements and its application in 3D-PLI is given in Chap. 2). In 3D-PLI, these fiber orientations are represented by vectors, which are tangential to the course of the respective nerve fiber. As depicted in Fig. 1.2, such a vector can be parameterized in spherical coordinates by its inclination angle, which denominates the out of plane angle, and the direction angle, which describes the orientation within the section plane. As 3D-PLI is a histological imaging technique, image registration of the individual measured brain sections is required to reconstruct a complete brain volume. In this volume a vector is assigned to every voxel. Hence, the 3D-PLI connectome is given by a three dimensional vector field that provides the (tangential) orientation of nerve fibers in every point.

The resolution of 3D-PLI is primarily limited by the optical design of the respective imaging system. Therefore, 3D-PLI is highly scalable as it is capable of analyzing the structural connectivity in brain sections at a mesoscopic level (with a field of view corresponding to the size of the brain) and at a microscopic level (with resolution limited by the wavelength of the light at approximately 0.5 µm). While this multiscale approach requires multiple polarimetric imaging systems [5], the working principle is the same and recent efforts have ensured the comparability across different 3D-PLI platforms [64]. One important step in this process was an improvement in the calibration process that has been developed in the course of this study and which is presented in Chap. 3.

3D-PLI is currently being established as a bridging modality that makes it possible to compare and cross validate structural connectivity data between different imaging methods. By applying structure tensor analysis to histological myelin stains, it is possible to generate information comparable to the direction angle information in 3D-PLI. Furthermore, recent efforts by Axer et al. demonstrated that introducing so called *PLI Orientation Distribution Functions (pliODF)* makes it possible to connect 3D-PLI with dMRI measurements and facilitate cross-validation between these two modalities [6].

The theoretical model of the birefringence of nerve fibers which the data analytics of 3D-PLI are based on, makes it possible to directly measure the direction of fibers. The inclination, on the other hand, has to be inferred from the measurement of a physical quantity called retardation. Axer et al. have demonstrated that this relationship can be unraveled in white matter regions with a constant myelination and fiber density. However, they also noted that their method was flawed in the transition regions between white and gray matter and at the axon terminals in the gray matter [4].

In this study, new algorithms have been developed to address ambiguities in this rela-

tionship on the basis of measurements with a tiltable specimen stage. By tilting the brain section, small changes are applied to the orientation of nerve fibers, which increases the available information and allows a non-ambiguous signal interpretation. In Chap. 4 the mathematical foundation of two algorithms is derived and it is shown that both algorithms enhance the reconstruction of the fiber architecture. Both algorithms essentially reconstruct similar orientation vectors, but differ in terms of the trade-off between accuracy and required computing resources. The advantages and pitfalls of each algorithm are explored and use cases demonstrate how they can be applied to investigate the fiber architecture.
As previously argued, one of the main advantages of 3D-PLI over other modalities is its multiscale applicability. While this holds true for the imaging principle and most image processing steps, the tiltable specimen stage is only feasible in a system whose field of view matches the specimen dimensions. In a microscopic imaging system on the other hand, such a specimen stage is not feasible. In order to prevent the developed algorithms from inhibiting the scalability of 3D-PLI, Chap. 5 deals with extending the current hardware concept of 3D-PLI microscopy. An oblique illumination system is developed in order to provide data similar to that of a tiltable specimen stage. Proof of principle measurements with a prototype demonstrate the feasibility of the new concept.

2

Basics of Birefringence Polarimetry and Its Application in Neuroscience

In the course of this chapter a review of the basics of *3D Polarized Light Imaging* is presented. The first part deals with the physical principles of polarimetry and describes the mathematical calculus that is used throughout this study. In contrast to previous studies on 3D-PLI by Axer et al. [4, 5], which described the theoretical foundation of 3D-PLI using the Jones calculus, the mathematical framework here is based on the Mueller-Stokes calculus. This calculus enables the description of unpolarized and partially polarized light which is required for the polarimetric calibration methods developed in Chap. 3. The current model for the interaction of polarized light with brain tissue is explained in Sec. 2.2. It is demonstrated how this model is used to extract information about the nerve fiber architecture with state of the art imaging systems. Further sections deal with the preparation of brain tissue before it is measured, and with the post processing of data for interpretation and visualization purposes.

2.1 Polarized Light and its Mathematical Description in Experiments

In general, polarization is a property of a transversal wave and describes the orientation of the associated oscillation plane. Light as a transversal electro-magnetic wave obeys the Maxwell equations and can be described by an oscillating electric field vector $\mathbf{E}(z, \tilde{t})$. Presuming a wave propagating along the z-axis of the coordinate system a solution to the wave equation is given by

$$\mathbf{E}(z, \tilde{t}) = \mathbf{E}_0 e^{i(kz - \omega\tilde{t})}, \tag{2.1}$$

where $\mathbf{E}_0 \in \mathbb{C}^2$ is the polarization state of the wave, also known as the Jones vector [36]. The imaginary constant is represented by $i = \sqrt{-1}$, k denotes the wave number, ω the angular frequency of the wave and $\tilde{t}$ the time parameter.
The interaction between polarized light and polarization sensitive optical elements can be described by the Jones calculus, where elements in the optical pathway, which influence the polarization state, are represented by complex 2×2-matrices. Multiplying the Jones vector with such a Jones matrix describes the changes in polarization when passing the

Parts of this chapter have been adapted from Wiese et al. [76].

corresponding optical element. This Jones formalism is well suited to describe coherent and completely polarized light (e.g. in laser applications). Previous studies on 3D-PLI [46, 4, 5] have used the Jones formalism to describe the experimental setup and the effects of birefringent brain tissue on polarized light. However, in this study the Mueller-Stokes calculus is used for the description of polarized light, since it relates directly to the measurands in the experiment. The camera of a common imaging system only records scalar gray value intensities. In the Mueller-Stokes formalism the light intensity values for basic polarization states are directly calculated, while the Jones formalism focuses on the description of the electric field. Hence, the Mueller-Stokes calculus is more common in literature on polarization sensitive imaging techniques [13, p. 22.14].
In the Mueller-Stokes calculus the polarization state of a light beam is described by the real valued Stokes vector which relates to the Jones vector by

$$\mathbf{S} = \begin{pmatrix} S_0 \\ S_1 \\ S_2 \\ S_3 \end{pmatrix} = \begin{pmatrix} E_{0x}E_{0x}^* + E_{0y}E_{0y}^* \\ E_{0x}E_{0x}^* - E_{0y}E_{0y}^* \\ E_{0x}E_{0y}^* + E_{0y}E_{0x}^* \\ iE_{0x}E_{0y}^* - iE_{0y}E_{0x}^* \end{pmatrix}. \tag{2.2}$$

The first component S_0 of this vector denotes the total light intensity, while each of the parameters S_1, S_2 and S_3 describe the predominance of two orthogonal polarization states. The Stokes parameter S_1 denotes the prevalence of linear horizontally over linear vertically polarized light, while the parameter S_2 describes the same for linearly $\pm 45°$ polarized light and S_3 describes the predominance of right handed over left handed circularly polarized light [15, p. 13]. In this representation of a polarized light beam, measurands that can be observed in the experiment (e.g. the light intensity) are directly accessible (e.g. in S_0). When using the Jones formalism on the other hand, the measured light intensity $I \propto \mathbf{E}_0 \cdot \mathbf{E}_0^*$ has to be derived after calculating the Jones vector $\mathbf{E}_0$. It is often useful to normalize the Stokes vector by $\mathbf{S}/S_0$ so that the Stokes parameters assume values of $-1 \leq S_1, S_2, S_3 \leq 1$. In addition, it is important to note that the Stokes parameters also must obey

$$S_0^2 \leq S_1^2 + S_2^2 + S_3^2,$$

with $\leq$ turning into $=$ for completely polarized light. For partially polarized light it is useful to define the degree of polarization as

$$p = \frac{\sqrt{S_1^2 + S_2^2 + S_3^2}}{S_0}.$$

A change in the polarization state of a light beam is described by multiplying the Stokes vector with a real valued 4×4-Mueller matrix. Unpolarized light represented by $\mathbf{S} = I_0 \begin{pmatrix} 1 & 0 & 0 & 0 \end{pmatrix}^\dagger$ can be changed into any polarization state by using a combination of three basic components [15, pp. 17-23]:

1. The linear polarizer has a preferred transmission axis that allows transmission of the linear polarization components parallel to the axis whereas light polarized perpendicular to that axis is strongly absorbed. Such a linear polarizer can be described by the Mueller matrix

$$\mathbf{M}_{\text{pol}}(p_x, p_y) = \frac{1}{2} \begin{pmatrix} p_x^2 + p_y^2 & p_x^2 - p_y^2 & 0 & 0 \\ p_x^2 - p_y^2 & p_x^2 + p_y^2 & 0 & 0 \\ 0 & 0 & 2p_x p_y & 0 \\ 0 & 0 & 0 & 2p_x p_y \end{pmatrix}, \tag{2.3}$$

where p_x and p_y denote the percentage of transmitted light with polarization states in x and y direction. Hence, an ideal polarizer with its transmission axis in x-direction would be described by the Mueller matrix $\mathbf{M}_{\text{pol}}(1,0)$. In experiments, the polarization filters are always flawed to some extent, reducing their efficiency to polarize light to a percentage p. Such a more realistic partial polarizer can be modelled by the Mueller matrix $\mathbf{M}_{\text{pol}}\left(\sqrt{\frac{1+p}{2}}, \sqrt{\frac{1-p}{2}}\right)$.

2. The retarder (sometimes also called waveplate when referring to an optical filter) induces a polarization-dependent change in the phase of the electromagnetic wave (also called *retardance* and denoted by δ). Such a retarder consists of a birefringent medium that has a polarization dependent refractive index. Hence, it induces the polarization-dependent phase shift[1], that can be described by the Mueller matrix

$$\mathbf{M}_{\text{wp}}(\delta) = \begin{pmatrix} 1 & 0 & 0 & 0 \\ 0 & 1 & 0 & 0 \\ 0 & 0 & \cos(\delta) & -\sin(\delta) \\ 0 & 0 & \sin(\delta) & \cos(\delta) \end{pmatrix}. \tag{2.4}$$

In technical applications, the two most common waveplates are the quarter-wave plate and the half-wave plate. The quarter-wave plate ($\delta = \pi/2$) converts circularly polarized light into linear polarized light, and linear polarized light is converted into circularly polarized light if its polarization axis is at an angle of $\pm 45°$ relative to the main axis of the retarder. The half-wave plate ($\delta = \pi$) generally rotates a linear polarized beam by an angle defined through the polarization plane relative to the axis of the waveplate.

3. The rotator (sometimes also called circular retarder) rotates the direction of linear polarized light by an angle θ. Such a rotation occurs in optical active media, e.g. in solutions of chiral molecules. Its Mueller matrix is given by [15, p. 22]

$$\mathbf{M}_{\text{rot}}(\theta) = \begin{pmatrix} 1 & 0 & 0 & 0 \\ 0 & \cos(2\theta) & \sin(2\theta) & 0 \\ 0 & -\sin(2\theta) & \cos(2\theta) & 0 \\ 0 & 0 & 0 & 1 \end{pmatrix}. \tag{2.5}$$

Additionally, the rotation matrix $\mathbf{M}_{\text{rot}}(\theta)$ can be used to account for a rotation between the coordinate system of a polarizing element and the laboratory system. Given $\mathbf{M}$ as the matrix of an optical element, the transformation

$$\mathbf{M}(\theta) = \mathbf{M}_{\text{rot}}(-\theta)\ \mathbf{M}\ \mathbf{M}_{\text{rot}}(\theta), \tag{2.6}$$

yields the matrix $\mathbf{M}(\theta)$, which describes the polarization effects if the respective element is rotated by an angle θ.
For this study, the rotated matrix of the retarder and the linear polarizer are of particular interest. The Mueller matrix of a general retarder with retardance δ and fast axis orientation θ is

$$\mathbf{M}_{\text{wp}}(\delta,\theta) = \begin{pmatrix} 1 & 0 & 0 & 0 \\ 0 & \cos^2(2\theta) + \cos(\delta)\sin^2(2\theta) & (1-\cos(\delta))\sin(2\theta)\cos(2\theta) & \sin(\delta)\sin(2\theta) \\ 0 & (1-\cos(\delta))\sin(2\theta)\cos(2\theta) & \sin^2(2\theta) + \cos(\delta)\cos^2(2\theta) & -\sin(\delta)\cos(2\theta) \\ 0 & -\sin(\delta)\sin(2\theta) & \sin(\delta)\cos(2\theta) & \cos(\delta) \end{pmatrix}. \tag{2.7}$$

[1] Further details on birefringence are given in Sec. 2.2

The matrix of an ideal linear polarizer with $p_x = 1$ and $p_y = 0$ rotated at an angle θ is given by

$$\mathbf{M}_{\mathrm{pol},x}(\theta) = \frac{1}{2}\begin{pmatrix} 1 & \cos(2\theta) & \sin(2\theta) & 0 \\ \cos(2\theta) & \cos(2\theta)^2 & \sin(2\theta)\cos(2\theta) & 0 \\ \sin(2\theta) & \sin(2\theta)\cos(2\theta) & \sin(2\theta)^2 & 0 \\ 0 & 0 & 0 & 0 \end{pmatrix}. \tag{2.8}$$

Respectively, the matrix of a rotated partial polarizer, which generates linear polarized light to a degree of polarization p, is given by

$$\mathbf{M}_{\mathrm{pol},x}(p,\theta) = \tfrac{1}{2}\begin{pmatrix} 1 & p\cos(2\theta) & p\sin(2\theta) & 0 \\ p\cos(2\theta) & \cos(2\theta)^2 + 2\sin(2\theta)^2\sqrt{1-p^2} & \sin(2\theta)\cos(2\theta)(1-2\sqrt{1-p^2}) & 0 \\ p\sin(2\theta) & \sin(2\theta)\cos(2\theta)(1-2\sqrt{1-p^2}) & \sin(2\theta)^2 + 2\cos(2\theta)^2\sqrt{1-p^2} & 0 \\ 0 & 0 & 0 & 2\sqrt{1-p^2} \end{pmatrix}. \tag{2.9}$$

These Mueller matrices cover all polarization effects that are discussed in this study; however, they do not represent a complete list of all possible polarization effects. A more extensive review is given by Chipman et al. [13].
In experimental studies polarimeters are employed to determine the Stokes vector of a light beam (light-measuring polarimeters) or the Mueller matrix of a sample (sample-measuring polarimeters). The measurement principle of a sample-measuring polarimeter is explained in the following. The beam irradiated from an (unpolarized) light source is polarized by a filter (also called polarization state generator - *PSG*) into a well defined polarization state. After passing the sample the light is analyzed by a second polarization filter (called the polarization state analyzer - *PSA*) and the beam intensity is recorded with a suitable sensor [13, p. 22.17]. Given the Stokes vector of a light source $\mathbf{S}_{\mathrm{source}}$ (often $\mathbf{S}_{\mathrm{source}} = \begin{pmatrix} I_0 & 0 & 0 & 0 \end{pmatrix}^\dagger$ in case of initially unpolarized light) and the Mueller matrix M_{PSG} of the polarization state generator, the polarization state that illuminates the sample can be written as

$$\mathbf{S}_{\mathrm{PSG}} = \mathbf{M}_{\mathrm{PSG}}\ \mathbf{S}_{\mathrm{source}}. \tag{2.10}$$

Similarly, the transposed Stokes vector for the polarization state analyzer $\mathbf{S}^\dagger_{\mathrm{PSA}}$ can be determined by multiplying the matrix of the polarization state analyzer $\mathbf{M}_{\mathrm{PSA}}$ from the left with the Stokes vector of the sensor $\mathbf{S}^\dagger_{\mathrm{sensor}}$ (e.g. $\mathbf{S}^\dagger_{\mathrm{sensor}} = \begin{pmatrix} 1 & 0 & 0 & 0 \end{pmatrix}$ for an ideal detector):

$$\mathbf{S}^\dagger_{\mathrm{PSA}} = \mathbf{S}^\dagger_{\mathrm{sensor}}\ \mathbf{M}_{\mathrm{PSA}}. \tag{2.11}$$

By controlling the PSG and the PSA the measured intensity becomes a linear combination of the sixteen Mueller matrix elements. In order to disentangle these elements, multiple measurements with different states of the PSG and PSA are conducted, and the intensity of the k-th measurement can be denoted as

$$I_k = \mathbf{S}^\dagger_{\mathrm{PSA},k}\ \mathbf{M}_{\mathrm{sample}}\ \mathbf{S}_{\mathrm{PSG},k}. \tag{2.12}$$

Therefore, determining all elements of an entirely unknown Mueller matrix requires at least sixteen measurements that provide sixteen linearly independent equations, which need to be analyzed by a suitable algorithm to provide the (least square) solution. However, some Mueller matrices are already fully characterized by only a few parameters. Hence, if the structure of the Mueller matrix is already known[2], it is sufficient to determine a subset of the Mueller matrix elements and infer the remaining ones. In these

[2] e.g. the sample is a birefringent medium which is completely described by the Mueller matrix of a retarder with two independent parameters

cases the setup of the polarimeter can be simplified (which will then be called an *incomplete* sample-measuring polarimeter) [13, pp. 22.20-22.24].
Due to the regular occurrence of trigonometric functions in the Mueller-Stokes calculus the trigonometric identities

$$\begin{aligned}
\sin(x \pm y) &= \sin(x)\cos(y) \pm \cos(x)\sin(y),\\
\cos(x \pm y) &= \cos(x)\cos(y) \mp \sin(x)\sin(y),\\
\sin(x)^2 &= \frac{1}{2}\left(1 - \cos(2x)\right),\\
\cos(x)^2 &= \frac{1}{2}\left(1 + \cos(2x)\right),\\
\sin(2x) &= 2\sin(x)\cos(x),\\
\cos(2x) &= 1 - 2\sin(x)^2,
\end{aligned}$$

are used in several calculations throughout this study. The intensity in Eq. (2.12) is often measured under the rotation of polarization filters and can be described by superposition of sinusoidal signals

$$I_k = \sum_j \Big(a_j \cos(j\rho_k) + b_j \sin(j\rho_k)\Big).$$

Here ρ_k denotes the angle of rotation ranging from 0° to 360° in equidistant steps. For such a signal we can perform a discrete Fourier transformation yielding the Fourier coefficients [62]

$$\begin{aligned}
a_0 &= \frac{1}{N}\sum_{k=0}^{N} I_k,\\
a_j &= \frac{2}{N}\sum_{k=0}^{N} I_k \cos(j\rho_k),\\
b_j &= \frac{2}{N}\sum_{k=0}^{N} I_k \sin(j\rho_k).
\end{aligned}$$

In a second step, the desired information such as the Mueller matrix of a sample can be derived from these coefficients. This, however, depends on the actual application and the experimental setup.
After understanding the concepts of polarimetry, the next section deals with the polarimetric effects of brain tissue and how we can utilize them to determine the fiber architecture.

2.2 Birefringence of Nerve Fibers

3D-PLI is based on the optical birefringence of myelinated nerve fibers. In general, birefringence describes the dependency of the refractive index of a medium on the polarization state of the incident light and occurs in anisotropic media. This dependency can be described by a refractive index ellipsoid, which is depicted in Fig. 2.1. The principal axes of this ellipsoid indicate the refractive index of the medium for light that is polarized in the corresponding directions. Depending on the anisotropic structure, the index ellipsoid has a rotational symmetry with two identical axes $n_x = n_y \neq n_z$ (uniaxial

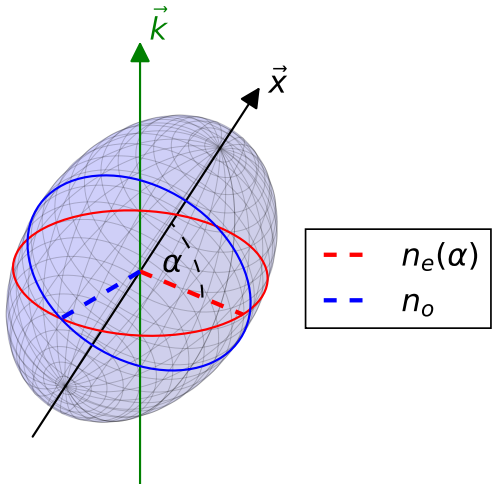

FIGURE 2.1: Uniaxial index ellipsoid for positive birefringence. Depending on the orientation of the main axis (**x**) relative to the direction of propagation (**k**) the refractive index for the extra ordinary ($n_e(\alpha)$) ray changes.

birefringence) or it has three different axes $n_x \neq n_y \neq n_z \neq n_x$ (biaxial birefringence)[3]. In the case of uniaxial birefringence the index ellipsoid is also called indicatrix [9, p. 799].

To illustrate how the macroscopically observable polarization effects arise from this model, we presume a polarized light ray propagating along the z-axis through a medium with uniaxial birefringence. The main axis (also called optic axis) of the indicatrix is oriented along the orientation vector **x**, as visualized in Fig. 2.1. The cross section of the indicatrix with the x-y-plane yields an ellipse whose main axes determine the refractive indices ($n_e(\alpha)$ and n_o) for the respective linear polarization states. The Jones[4] vector of the incident light $\mathbf{E_0}$ can be written as a superposition of two orthogonal linear polarization states, oriented along these two axes

$$\mathbf{E_0} = \mathbf{E_o} + \mathbf{E_e},$$

also called the *ordinary* ($\mathbf{E_o}$) and the *extraordinary* ($\mathbf{E_e}$) wave. Since the optical path length in a medium is proportional to the refractive index, each of these waves experiences an individual phase shift ($\delta_o = \frac{2\pi n_o t}{\lambda}$ and $\delta_e = \frac{2\pi n_e t}{\lambda}$) while passing through the birefringent medium, with λ as the wavelength of the incident light and t as the thickness of the medium. Hence, the electric field vector can be written as

$$\begin{aligned}\mathbf{E} &= \mathbf{E_o} e^{i\delta_o} + \mathbf{E_e} e^{i\delta_e} \\ &= \left(\mathbf{E_o} e^{i\frac{\delta_o-\delta_e}{2}} + \mathbf{E_e} e^{-i\frac{\delta_o-\delta_e}{2}}\right) e^{i\frac{\delta_o+\delta_e}{2}},\end{aligned}$$

where the first part yields the new Jones vector

$$\mathbf{E_0}' = \mathbf{E_o} e^{i\frac{\delta_o-\delta_e}{2}} + \mathbf{E_e} e^{-i\frac{\delta_o-\delta_e}{2}},$$

while the second part is the phase shift experienced by both waves, which is irrelevant in terms of polarization effects. The relative phase shift between the two waves

$$\delta = \delta_e - \delta_o = \frac{2\pi t(n_e - n_o)}{\lambda}, \tag{2.13}$$

[3]The biaxial model is not relevant in the context of this study due to the rotational symmetry of fibers and will therefore not be discussed any further.

[4]The polarized light is described by the Jones vector since birefringence results in a phase shift, which is not described by Stokes vector.

is called retardance, i.e. the ordinary wave is retarded by δ relative to the extraordinary wave. The refractive index for the extraordinary wave n_e depends on the orientation of the optic axis relative to the direction of light propagation indicated by the vector $\mathbf{k}$ (cf. Fig. 2.1). Therefore, the refractive index is a function of the angle α, which can be derived from the elliptic geometry of the indicatrix, yielding

$$n_e(\alpha) = \frac{1}{\sqrt{\frac{\sin(\alpha)^2}{n_o} + \frac{\cos(\alpha)^2}{n_E}}}, \tag{2.14}$$

where n_E and n_o denote the two axes of the indicatrix. For small differences of these two indices Eq. (2.13) can be approximated by[5]

$$\delta \approx \frac{2\pi t \Delta n}{\lambda} \cos(\alpha)^2, \tag{2.15}$$

where the quantity $\Delta n = n_E - n_o$ denotes the magnitude of the optical anisotropy and is called birefringence. Depending on the sign of Δn, it is often distinguished between positive and negative uniaxial birefringent materials. For a more concise mathematical treatment in the following calculations, the relative thickness $t_{\text{rel}} = 4t\Delta n/\lambda$ is introduced, yielding

$$\delta \approx \frac{\pi}{2} t_{\text{rel}} \cos(\alpha)^2. \tag{2.16}$$

This simplification was first introduced by Axer et al. [4]. It takes into account that only the combined effect of sample thickness t, birefringence Δn and wavelength λ is relevant for the signal interpretation but not the individual values.

The theoretical model behind the 3D-PLI image analysis presumes that the birefringence of a myelinated axon is described by a uniaxial indicatrix, whose principal axis is aligned along the fiber orientation [46]. This macroscopic optical property of myelinated axons originates from the microstructural organization of filaments within the axon as well as the ordered arrangement of lipids and proteins in the myelin sheath [28, 68]. The strongest contribution to the experimentally observable birefringence is caused by the sheath, which can be modelled by multiple radially oriented positive indicatrices. Studies by Bear et al. [8] and Menzel et al. [53] demonstrated that this microscopic anisotropy leads to a macroscopic negative birefringence of myelinated axons, which was observed experimentally in several studies [8, 12, 18].

Apart from the polarimetric effects, the myelin sheath of an axon also causes strong light scattering and absorption [72, 34]. The combined effect causes light attenuation during imaging which is described by the Lambert-Beer law

$$I = I_0 e^{-\mu t}. \tag{2.17}$$

The optical effect of brain tissue, including both negative uniaxial birefringence[6] and light attenuation, is represented by the Mueller matrix

$$\mathbf{M}_{fiber} = e^{-\mu t} \begin{pmatrix} 1 & 0 & 0 & 0 \\ 0 & \cos^2(2\varphi) + \cos(\delta)\sin^2(2\varphi) & (1-\cos(\delta))\sin(2\varphi)\cos(2\varphi) & -\sin(\delta)\sin(2\varphi) \\ 0 & (1-\cos(\delta))\sin(2\varphi)\cos(2\varphi) & \sin^2(2\varphi) + \cos(\delta)\cos^2(2\varphi) & \sin(\delta)\cos(2\varphi) \\ 0 & \sin(\delta)\sin(2\varphi) & -\sin(\delta)\cos(2\varphi) & \cos(\delta) \end{pmatrix}. \tag{2.18}$$

This matrix (which is similar to the matrix of a general retarder in Eq. (2.4)) is parameterized by the in plane orientation φ, the retardation $\sin(\delta)$ and absorption $e^{-\mu t}$ [7]. In

[5] This approximation has been used in several studies [46, 4, 5]. A more detailed derivation based on a Taylor expansion is presented in Appx. A.1.

[6] Here, δ is defined positive and the signs in the matrix are changed.

[7] It is important to note that δ is defined as a positive quantity, while the signs of the respective matrix elements reflect the negative sign of the birefringence.

order to derive the course of nerve fibers within histological sections of the brain, a suitable polarimetric setup is needed to determine these quantities, which will be discussed in the following section.

2.3 Established Experimental Methods in 3D-PLI

For this study two polarimetric systems were employed - a large area polarimeter *(LAP)* capable of capturing whole human brain sections in a single shot at a pixel size of 64 µm × 64 µm, and a polarizing microscope *(PM)* with a pixel size of 1.33 µm × 1.33 µm. This section covers the experimental setup of these two systems and shows the established approach to interpret the recorded data.
In a standard 3D-PLI measurement with the LAP (shown in Fig. 2.2), an unstained histological brain section is illuminated with circularly polarized light. The brain tissue changes the polarization state which is examined with a linear analyzer. The circularly polarized light is created by a linear polarizer and a quarter-wave retarder whose fast axis is rotated by $\pi/4$ with respect to the polarizer. In principle, this system allows all three filters to be rotated independently of each other. For a standard 3D-PLI measurement as described by Axer et al. [4] all three filters are rotated simultaneously by an angle of ρ_k. Hence, the polarization state generator is described by

$$\mathbf{S}_{\mathrm{PSG_{LAP}}} = \mathbf{M}_{\mathrm{rot}}(-\rho_k)\ \mathbf{M}_{\mathrm{wp}}\left(\frac{\pi}{2}, \frac{\pi}{4}\right)\ \mathbf{M}_{\mathrm{pol}}(1,0)\ \mathbf{M}_{\mathrm{rot}}(\rho_k)\ \begin{pmatrix} I_0 \\ 0 \\ 0 \\ 0 \end{pmatrix} = \frac{I_0}{2}\begin{pmatrix} 1 \\ 0 \\ 0 \\ -1 \end{pmatrix}, \quad (2.19)$$

and the polarization state analyzer by

$$\begin{aligned} \mathbf{S}^{\dagger}_{\mathrm{PSA_{LAP}}} &= \begin{pmatrix} 1 & 0 & 0 & 0 \end{pmatrix}\ \mathbf{M}_{\mathrm{rot}}(-2\rho_k)\mathbf{M}_{\mathrm{pol}}(0,1)\ \mathbf{M}_{\mathrm{rot}}(2\rho_k) \\ &= \frac{1}{2}\begin{pmatrix} 1 & -\cos(2\rho_k) & -\sin(2\rho_k) & 0 \end{pmatrix}. \end{aligned} \quad (2.20)$$

The setup of the PM is similar to that of the LAP but differs in two aspects regarding its polarimetry. First, the polarization generator and analyzer are switched, meaning that the brain tissue is illuminated with linearly polarized light and the resulting polarization state is analyzed with a circular analyzer. Second, only the polarizer is rotated while the circular analyzer remains in the same position. Hence, the input polarization state at a rotation angle ρ_k of the polarizer is given by

$$\mathbf{S}_{\mathrm{PSG_{PM}}} = \mathbf{M}_{\mathrm{rot}}(-\rho_k)\ \mathbf{M}_{\mathrm{pol}}(1,0)\ \mathbf{M}_{\mathrm{rot}}(\rho_k)\ \begin{pmatrix} I_0 \\ 0 \\ 0 \\ 0 \end{pmatrix} = \frac{I_0}{2}\begin{pmatrix} 1 \\ \cos(2\rho_k) \\ \sin(2\rho_k) \\ 0 \end{pmatrix}, \quad (2.21)$$

and the polarization state analyzer is given by

$$\mathbf{S}^{\dagger}_{\mathrm{PSA_{PM}}} = \begin{pmatrix} 1 & 0 & 0 & 0 \end{pmatrix}\ \mathbf{M}_{\mathrm{pol}}(0,1)\ \mathbf{M}_{\mathrm{wp}}\left(\frac{\pi}{2}, \frac{\pi}{4}\right) = \frac{I_0}{2}\begin{pmatrix} 1 & 0 & 0 & -1 \end{pmatrix}. \quad (2.22)$$

The polarimetric imaging systems used in this study were custom made. In the in-house developed LAP, the illumination is realized by a LED panel (NSPG 510S manufactured by *Nichia corporation*) consisting of an array of 36 × 36 single LEDs. This LED array

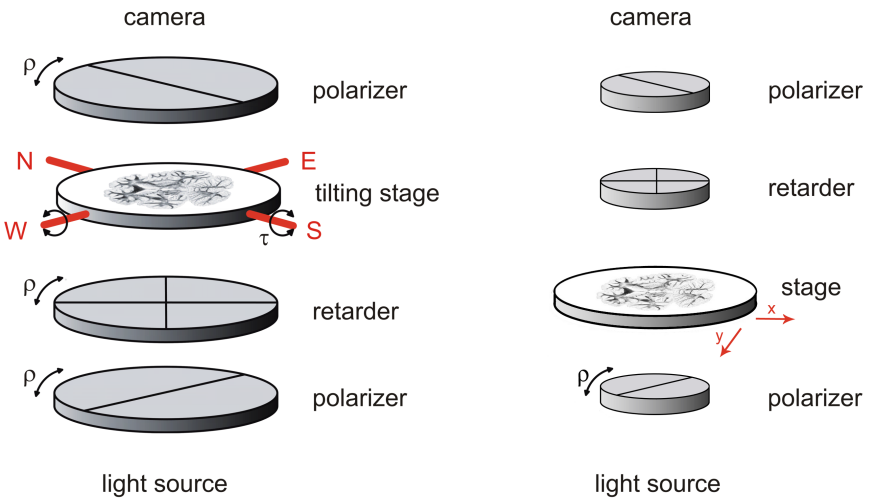

(a) LAP (b) PM

FIGURE 2.2: Sketch of the LAP (a) and PM (b) setup. In both systems, light is polarized into a well defined state and analyzed after it has passed the specimen. The LAP is equipped with a tiltable specimen stage, while the microscope employs an x-y-stage in order to scan the sample tile-wise.

illuminates an area of 300 mm × 300 mm at a central wavelength of $\lambda = 529$ nm. To ensure a constant brightness, the LED array is powered by a constant current source, while a water cooling system stabilizes the operating temperature. The illumination field is homogenized by diffuser plates made out of acrylic glass which are placed above the LED panel. The employed polarization filters manufactured by *Jos. Schneider Optische Werke GmbH* are made out of polymer foils and have a diameter of 240 mm. Each filter can be individually rotated or even removed from the system, so that also nonstandard measurements can be conducted. Due to the lack of commercially available filters with such a diameter, the retarder is not an exact match for the illumination wavelength and is specified for a wavelength of $\lambda = 568$ nm. This discrepancy in the wavelength of illumination and retarder introduces a bias in the quantitative image analysis and creates the need for a suitable calibration, which is discussed in Chap. 3. The brain section is mounted on a two-axes tiltable specimen stage that allows to tilt the brain section up to 8° around each axis. This feature is unique to the LAP and is not present in the PM. The PM, constructed by *Taorad GmbH*, has a reversed setup compared to the LAP. The light source consists of a single white light emitting LED (*IntraLED 2020+* operated at 24 W) filtered by a band-pass optic with a central peak wavelength of $\lambda = 550\,\text{nm} \pm 5\,\text{nm}$ to match the specified wavelength of the employed quarter-wave retarder. The employed polarization filters are standard filters for polarization microscopy with a diameter of approximately 25.4 mm. To ensure a uniform illumination of the sample, a Koehler illumination system was employed[8]. The PM has a field of view of approximately 2.7 mm × 2.7 mm. Hence, a histological brain slice is scanned tile-wise by employing an x-y-table as a specimen stage. The individual images are stitched together by an in-house developed software tool. Thereby, 3D-PLI is capable of generating a high resolution image of the whole brain slice without loss in the field of view.
For each system, the resulting light intensity signal I_k under the rotation of the filters

[8]Further details on the working principles of a Koehler illumination can be found in Chap. 5.

is calculated by the Mueller-Stokes calculus

$$I_k = \mathbf{S}^{\dagger}_{\mathrm{PSA},k}\ \mathbf{M}_{fiber}\ \mathbf{S}_{\mathrm{PSG},k}. \tag{2.23}$$

This leads to the same formula for both systems, which has been described by Axer et al. [4]

$$I_k = \frac{I_0 e^{-\mu t}}{4} + \frac{I_0 e^{-\mu t}}{4}\sin(\delta)\cos(2\varphi)\sin(2\rho_k) - \frac{I_0 e^{-\mu t}}{4}\sin(\delta)\sin(2\varphi)\cos(2\rho_k)\ . \tag{2.24}$$

Performing a Fourier analysis on this recorded intensity signal leads to the Fourier coefficients[9]

$$\begin{aligned}
a_0 &= \frac{1}{N}\sum_{k=0}^{N-1} I_k &&= \frac{I_0 e^{-\mu t}}{4},\\
a_1 &= \frac{2}{N}\sum_{k=0}^{N-1} I_k\cos(2\rho_k) &&= -\frac{I_0 e^{-\mu t}}{4}\sin(\delta)\sin(2\varphi),\\
b_1 &= \frac{2}{N}\sum_{k=0}^{N-1} I_k\sin(2\rho_k) &&= \frac{I_0 e^{-\mu t}}{4}\sin(\delta)\cos(2\varphi).
\end{aligned}$$

From these Fourier coefficients the so called *transmittance, retardation* and *direction* (or direction angle) are generated by a transformation of the parameter space. The transmittance is calculated by

$$I_T = \frac{I_0 e^{-\mu t}}{2} = 2a_0, \tag{2.25}$$

displaying the attenuation coefficient of the tissue. This parameter map resembles the image obtained by standard transmission imaging techniques. The definition of I_T is chosen in order to comply with the one introduced by Axer et al. [4]. The retardation

$$\sin(\delta) = \frac{\sqrt{a_1^2 + b_1^2}}{a_0}, \tag{2.26}$$

is the relative amplitude of the intensity profile I_k and is related to the fiber inclination and the relative thickness. The phase of the intensity profile given by

$$\varphi = \frac{1}{2}\arctan 2\,(a_1, -b_1) + \frac{\pi}{2}, \tag{2.27}$$

is equal to the in-plane direction angle of the nerve fibers. Each of these calculations is carried out for every image pixel, providing the respective parameter maps depicted in Fig. 2.3.

As the main goal of 3D-PLI is to determine the fiber orientation vector, the next step of the data analysis is to derive the fiber inclination angle from the measured retardation. This is significantly more challenging since the inclination is always conjointly measured with the relative thickness. Hence, a method for isolating these two entangled variables is required. For addressing this issue Axer et al. first verified that the condition

$$t_{\mathrm{rel}} \leq 1, \tag{2.28}$$

[9] Here I deviate from the notation of the Fourier coefficients introduced by Axer et al. to comply with the more common notation of Fourier coefficients. Hence, the meaning of a_1 and b_1 is switched compared to published 3D-PLI literature [4, 5].

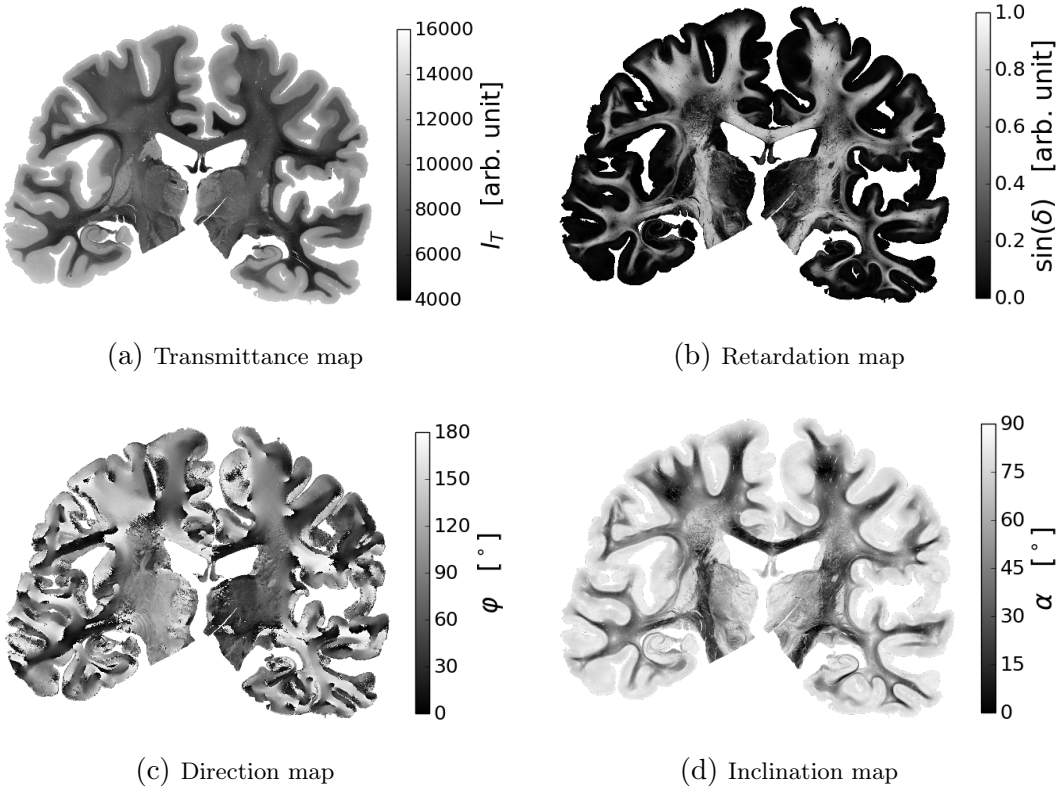

(a) Transmittance map

(b) Retardation map

(c) Direction map

(d) Inclination map

FIGURE 2.3: The different modalities obtained by the standard 3D-PLI analysis.

applies for the imaged histological slides. This condition is important, to obtain unambiguously the phase retardance $\delta = \frac{\pi}{2} t_{\text{rel}} \cos(\alpha)^2$ from a measured retardation value $\sin(\delta)$ by simply applying the arcsin-function. Presuming a constant relative thickness across a whole brain section, Axer et al. determined the parameter t_{rel} by a statistical analysis [4]. They argued that the highest values $\sin(\delta)_{max}$ in a retardation map are assumed for fibers with an inclination of $\alpha = 0$. Hence, the relative thickness is calculated by

$$t_{\text{rel}} = \frac{2}{\pi} \arcsin\left(\sin(\delta)_{max}\right), \tag{2.29}$$

and for every image pixel the respective inclination can be calculated by inverting Eq. (2.16), yielding

$$|\alpha| = \arccos\left(\sqrt{\frac{2}{\pi}\frac{1}{t_{\text{rel}}}\arcsin\left(\sin(\delta)\right)}\right). \tag{2.30}$$

In order to avoid the influence of outliers, the value $\sin(\delta)_{max}$ was determined by fitting a sigmoid-function to the tail of the frequency distribution [4]. While the presumption of a constant t_{rel} is reasonable for deep white matter regions, it will also lead to misinterpretation of the fiber inclination in cortical regions and in the transition domains between white and grey matter. In these regions, variations in myelination and fiber density occur [46] resulting in a change of t_{rel}. This issue is observable in the inclination map in Fig. 2.3d, where the whole cortex appears to contain only fibers oriented along the z-axis.

The second issue of determining the inclination arises from an inherent sign ambiguity due to the relationship $\delta \propto \cos(\alpha)^2$ even if the value of t_{rel} is known. Solving this sign ambiguity was addressed by Kleiner et al. who employed a tiltable specimen stage in the

LAP in order to apply small rotations to the fiber orientation vector [42]. By examining the changes in the respective retardation values, Kleiner et al. were able to infer the sign of the inclination.
In Chap. 4 new ways of a more accurate inclination reconstruction are explored, by using the additional data obtained with the tiltable specimen stage. It is demonstrated that this data holds information about the sign of the inclination as well as the local fiber density. Chap. 5 deals with implementing the necessary hardware to perform such an analysis not only on a mesoscopic but also on a microscopic resolution scale.

2.4 3D-PLI Data Visualization

Once a brain section is measured and the obtained data is processed, the information of the fiber orientation needs to be visualized. Since the fiber pathways are represented by a vector field in three dimensional space, one well suited possibility of data visualization is to encode the orientation in an RGB color map, also known as Fiber Orientation Map (FOM). By converting the determined spherical coordinates α and φ into Cartesian coordinates, the colors of the FOM are calculated by

$$\begin{aligned} \text{Red} &= 255\,|\cos(\alpha)\cos(\varphi)|\,, \\ \text{Green} &= 255\,|\cos(\alpha)\sin(\varphi)|\,, \\ \text{Blue} &= 255\,|\sin(\alpha)|\,. \end{aligned}$$

Fig. 2.4a shows a typical FOM generated by the 3D-PLI procedure. Red colored pixels indicate that fibers are oriented along the horizontal axis of the image, while green colored ones indicate a vertical fiber orientation. Fibers oriented out of the section plane are encoded by a blue coloring. Since only the absolute value of the Cartesian coordinates is visualized, there is an inherent ambiguity in this type of color-coding. However, this coloring is well known from the visualization of DTI Tensor Fields.
Interpreting FOMs by contrast can already provide significant information to neuroscientists about the course of fiber pathways, especially at a microscopic resolution. For lower resolved images provided by the LAP, small fiber pathways are often below the resolution limit. In these cases, the fiber orientation is solely indicated by the coloring and is not always easily accessible to the observer.
When a more accurate visual interpretation of the orientations is necessary, the depiction can be enhanced by plotting the actual vector field as shown in Fig. 2.4b. While the color-coding remains the same, additionally the orientation of the nerve fibers can now be directly assessed. In this two dimensional representation of the vector field, the length of the line encodes the vector component perpendicular to the image plane (i.e. the shorter the line the steeper is the course of the respective fiber). Depending on the level of detail needed in an analysis it is sometimes helpful to display only every n-th pixel as a vector to generate a more concise overview. This data reduction is especially useful in relatively homogeneous areas with only slowly changing fiber orientations. The interpretation of very heterogeneous tissue is likely to suffer since important data might be neglected in this visualization.

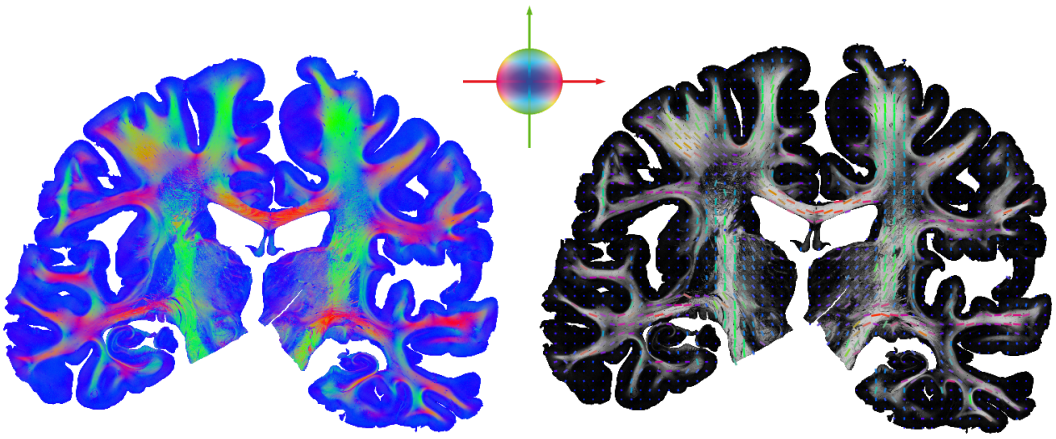

(a) Fiber Orientation Map (FOM) colors encode the 3D orientation.

(b) Retardation map overlayed with a visualization of the vector field. Only every 40th Vector was mapped

FIGURE 2.4: Visualization of the PLI vector field. In both figures, the color-coding represents the different orientations of the vectors according to the color sphere. While the RGB coloring (a) provides more details, in the vector representation (b) the in plane orientation can be assessed more accurately.

2.5 Preparation of Histological Brain Slides and Volumetric Reconstruction

In this study, datasets from two different human brains were analyzed. Both brains were obtained through donor programs in accordance with the local legal requirements. The brains were removed within 24 hours after the patients' death and fixed with 4% solution of buffered formaldehyde to avoid tissue degeneration. Before freezing the brain, it was immersed in a 20% solution of glycerin with Dimethyl sulfoxide (DMSO) for cryoprotection. The brains were frozen and sectioned coronally into slices with a thickness of 70 µm by a cryostat microtome (*Polycut CM 3500, Leica, Germany*). For each brain slice a so-called *block-face image* of the cutting surface was captured in order to create a reference for the volumetric reconstruction. The slices were then mounted on glass slides, immersed in a 20% solution of glycerin to avoid dehydration and protected from exposure by a coverslip.
The dataset from the first brain features a whole human brain section, which is used for the evaluation of fibers oriented parallel to the section plane. The section investigated in this study covers the mid-brain abreast of the Thalamus. The second dataset consists of approximately 220 consecutive slides from the right hemisphere of a second brain. This dataset is used to examine the fiber pathways oriented along the cutting direction (i.e. the z-axis). In order to follow the pathways, the 3D-Volume of these slices needs to be reconstructed. The position of this reconstructed volume within the hemisphere is shown in Fig. 2.5.
During the cutting process the brain slices are deformed and do not match the original structure. Hence, a multi-step image registration procedure is used to computationally reverse these deformations [59]. For this process, first the block-face images are stacked in order to create a reference volume [69]. Then, an affine image transformation (i.e. a global transformation that includes translation, rotation, reflection and shearing) morphs the image of each slide onto its corresponding block-face image. When applying

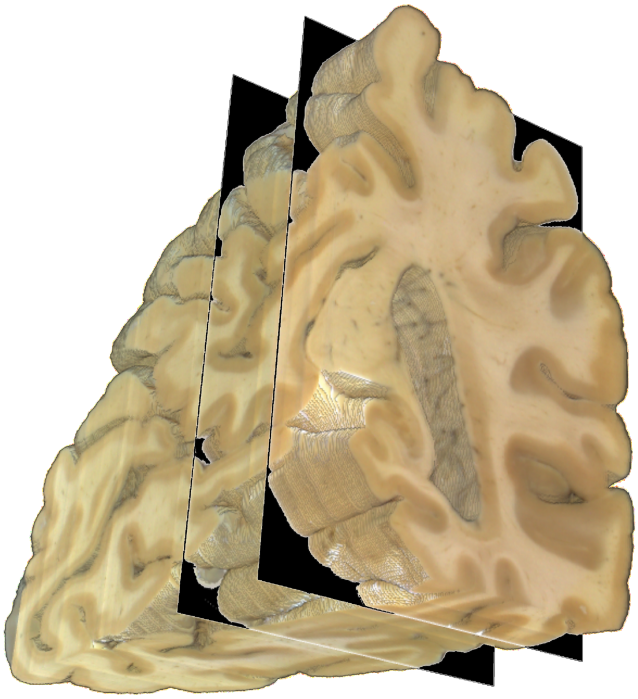

FIGURE 2.5: Reconstructed block-face volume of the examined brain hemisphere. The planes represent the boundaries of the dataset that was used to validate the algorithms in Chap. 4.

the transformation it is necessary to also reorientate the calculated vectors accordingly (cf. [59] for further details). However, this preprocessing only transforms the image as a whole, while deformations in the tissue are often localized to certain regions. Thus, in a second step a more sophisticated b-spline registration is applied, which is capable of applying local deformations. The best volume reconstruction to date is achieved by a third processing step which uses a *simultaneous* b-spline transformation. This method accounts not only for information in the image plane, but also along the z-axis [22, 27] and is thereby capable of ensuring smoother transitions along the z-axis.

3

Polarimetric Calibration of the LAP

This chapter deals with the calibration of recorded 3D-PLI measurement data. The calibration is especially relevant for the analysis presented in Chap. 4, which is based on small changes of the measured intensity profile when tilting the sample. Hence, a directive needs to be developed to ensure the accurate polarimetric measurement of the histological brain sections.
The approach presented here is based on a description of the polarization filters, which considers an inhomogeneous absorption and non ideal polarization properties. The current calibration method that is used for all 3D-PLI imaging systems is presented in Sec. 3.1. It is well suited to compensate for inhomogeneous absorption, but not for the actual polarization properties. Hence, in Sec. 3.2 a new polarimetric calibration is developed, which accounts for the systematic errors introduced by real polarization filters. In Sec. 3.3 it is described how the filter properties of the LAP can be determined in order to apply the calibration procedure to the measured data, and Sec. 3.4 provides a short discussion on the influence of the polarimetric calibration.

3.1 The Standard Intensity Based Calibration in 3D-PLI

The currently used image calibration for the 3D-PLI imaging systems developed by Dammers et al. [16] compensates for the accumulated effect of several error sources. While the LED-Array is homogenized by diffuser plates the illumination does not display a constant intensity level across the whole image. Additionally, the polarization filters display inhomogeneities in the level of absorption, which are rotated with the filters. When recording the images, each pixel within the CCD array of the camera displays a unique light sensitivity characteristic and is also distorted by read out noise.
To account for these effects Dammers et al. proposed to determine *gain factor frames* ($g(x, y, \rho_k)$) for each of the 18 rotation angles of the polarization filters which account for the accumulated effects [16]. Multiplication of these gain factors with the measured intensity $I'(x, y, \rho_k)$ at location x, y and angle ρ_k yields the calibrated intensity profile

$$I(x, y, \rho_k) = g(x, y, \rho_k) I'(x, y, \rho_k). \tag{3.1}$$

Parts of this chapter have been published [64], however, the analysis has been recalculated using Mueller-Stokes and extended to account for partial polarization.

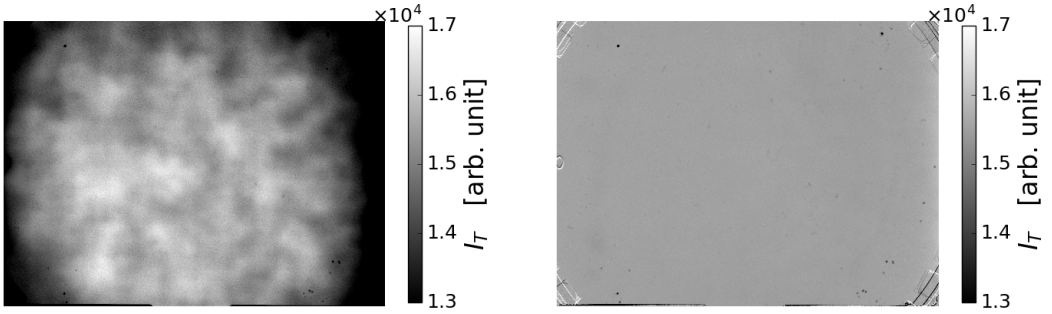

(a) Transmittance before calibration. (b) Transmittance after calibration.

FIGURE 3.1: Shown are transmittance images with an empty specimen stage before and after the calibration. It is clearly visible that the illumination field is homogenized by the calibration and the only remaining artifacts are cause by dust particles on the filters.

In order to generate the gain factors a set of 100 calibration images (so called flat fields) for each of the 18 rotation angles of the polarization filters is recorded under experimental conditions. From these sets the average calibration image $\bar{I}_{\text{flat}}(x, y, \rho_k)$ is calculated for each angle, to minimize the influence of noise. A single reference value I_{ref} for the intensity is defined as the mode (most common value) across the joint distribution of all 1800 recorded flat fields. The gain factors were then constructed by

$$g(x, y, \rho) = I_{\text{ref}}/\bar{I}_{\text{flat}}(x, y, \rho). \tag{3.2}$$

This intensity based calibration creates a uniform background as shown in Fig. 3.1. However, this method only corrects errors that contribute in a multiplicative manner to the measured intensity (i.e. absorption, detection sensitivity etc.). Changes in intensity that are caused by polarimetric errors, depend not only on the system but also on the sample that is being measured. These errors occur when there is a systematic difference between the presumed and actual polarization states that are generated and analyzed by the imaging system. Hence, it is necessary to complement the intensity based calibration by a polarimetric calibration, which is presented in the next section.

3.2 Accounting for Non-Ideal Polarization Filters

In general there are numerous effects that cause polarization filters to behave in a non-ideal manner. For example the polarization properties of a filter depend on the operating temperature, the incident angle of the light relative to the filter or simply the variations caused by limitations of the fabrication process [29, pp. 503-528]. Modern manufacturing technologies allow a reliable production of polarization elements with high quality. However, since laser applications pose the driving market for polarization elements these quality standards are only feasible for small diameter filters. Commercially available large diameter filters (such as the ones used in the LAP) on the other hand, lack both quality and variety.
The two predominant effects of non ideal filters that influence the measurements of the LAP are the degree of polarization p achieved by the linear polarizers and the actual retardance γ of the waveplate. The limited degree of polarization is virtually present in

all linear polarizers and particularly relevant for the large diameter filters utilized in the LAP. The quarter-wave retarder is specified for a wavelength of $\lambda_{\text{ret}} = 568\,\text{nm}$ of the incident light while the employed light source emits at a wavelength of $\lambda_{\text{source}} = 529\,\text{nm}$. This discrepancy causes a deviation of the retardance induced by the waveplate so that it is not exactly a quarter of the wavelength. Hence, the PSG and PSA are not exactly as described in Sec. 2.3, making a more accurate description necessary.
To account for similar effects, Chipman et al. [13] have described in their study a way to determine Mueller matrix elements from a data reduction algorithm, which is capable of accounting for arbitrary but well-known polarization generator ($\mathbf{S}_{PSG}$) and analyzer ($\mathbf{S}_{PSA}$) states. However, this procedure requires that the polarization states generate a sufficient set of linearly independent equations which is not the case for the present measurement protocol. Establishing a new measurement protocol would cause conflicts with the standardized 3D-PLI workflow and lead to the obstruction of other studies. While such a change might be feasible in the long run, for the purpose of this study it is more desirable to adapt the current analysis with respect to the non-ideal filter properties.
In order to understand the effects of the real polarization filters on the measurement, the intensity profile in Sec. 2.3 is recalculated with the ideal linear polarizer matrices in Eq. (2.20) and Eq. (2.21) being replaced by the matrices of partial polarizers (see Eq. (2.9)). Since the two polarizers are structurally identical, both filters display the same degree of polarization p. Additionally, the matrix of an ideal quarter wave retarder in Eq. (2.21) is replaced with that of a retarder with arbitrary retardance γ. This results in the generated polarization states

$$\begin{aligned}\tilde{\mathbf{S}}_{PSG_{LAP}}(\rho_k) &= \mathbf{M}_{\text{rot}}(-\rho_k)\ \mathbf{M}_{\text{wp}}(\gamma)\ \mathbf{M}_{\text{pol}}\left(\sqrt{\frac{1+p}{2}}, \sqrt{\frac{1-p}{2}}\right)\ \mathbf{M}_{\text{rot}}(\rho_k)\ \begin{pmatrix} I_0 \\ 0 \\ 0 \\ 0 \end{pmatrix} \\ &= \frac{I_0}{2}\begin{pmatrix} 1 \\ p\cos(\gamma)\cos(2\rho_k) \\ p\cos(\gamma)\sin(2\rho_k) \\ -p\sin(\gamma) \end{pmatrix}, \end{aligned} \tag{3.3}$$

while the analyzer state is correctly described by

$$\begin{aligned}\tilde{\mathbf{S}}^{\dagger}_{PSA_{LAP}}(\rho_k) &= \begin{pmatrix} 1 & 0 & 0 & 0 \end{pmatrix}\ \mathbf{M}_{\text{rot}}(-\rho_k)\ \mathbf{M}_{\text{pol}}\left(\sqrt{\frac{1-p}{2}}, \sqrt{\frac{1+p}{2}}\right)\ \mathbf{M}_{\text{rot}}(\rho_k) \\ &= \frac{1}{2}\begin{pmatrix} 1 & -p\cos(2\rho_k) & -p\sin(2\rho_k) & 0 \end{pmatrix}. \end{aligned} \tag{3.4}$$

The measurement of nerve fiber tissue with the polarization states results in a new formula for the intensity profile measured in each pixel. Under the rotation of the filters

by an angle ρ_k this profile is now given by[1]

$$\begin{aligned}
\tilde{I}(\rho_k) =& \tilde{\mathbf{S}}_{PSA_{LAP}}(\rho_k)\mathbf{M}_{fiber}\tilde{\mathbf{S}}_{PSG_{LAP}}(\rho_k) && (3.5)\\
=& \frac{I_0 e^{-\mu t}}{4}\Big[1 - p^2\cos(\gamma)\frac{1}{2}\left(1+\cos(\delta)\right) && (3.6)\\
& - p^2\cos(\gamma)\frac{1}{2}\left(\cos(4\rho_k)\right)\left(1-\cos(\delta)\right)\cos(4\varphi) && (3.7)\\
& - p^2\cos(\gamma)\frac{1}{2}\sin(4\rho_k)\left(1-\cos(\delta)\right)\sin(4\varphi) && (3.8)\\
& - p^2\sin(\gamma)\cos(2\rho_k)\sin(\delta)\sin(2\varphi) && (3.9)\\
& + p^2\sin(\gamma)\sin(2\rho_k)\sin(\delta)\cos(2\varphi)\Big]. && (3.10)
\end{aligned}$$

A Fourier analysis of this profile yields the coefficients

$$\begin{aligned}
\tilde{a}_0 =& \quad \frac{I_0 e^{-\mu t}}{4}\left(1 - \frac{p^2\cos(\gamma)}{2}\left(1+\cos(\delta)\right)\right),\\
\tilde{a}_1 =& -\frac{I_0 e^{-\mu t}}{4}p^2\sin(\gamma)\sin(\delta)\sin(2\varphi),\\
\tilde{b}_1 =& \quad \frac{I_0 e^{-\mu t}}{4}p^2\sin(\gamma)\sin(\delta)\cos(2\varphi),\\
\tilde{a}_2 =& -\frac{I_0 e^{-\mu t}}{8}p^2\cos(\gamma)(1-\cos(\delta))\sin(4\varphi),\\
\tilde{b}_2 =& -\frac{I_0 e^{-\mu t}}{8}p^2\cos(\gamma)(1-\cos(\delta))\cos(4\varphi).
\end{aligned} \qquad (3.11)$$

Note that for $\gamma = \pi/2$ and $p = 1$ these coefficients are identical to those calculated for the ideal case as one would expect. From these coefficients the transmittance and retardation maps can be calculated by

$$I_T = 2\frac{\tilde{a}_0 - \mathrm{sign}(\cos(\gamma))\sqrt{\tilde{a}_2^2 + \tilde{b}_2^2}}{1 - p^2\cos(\gamma)}, \qquad (3.12)$$

and

$$\sin(\delta) = \frac{\sqrt{\tilde{a}_1^2 + \tilde{b}_1^2}}{\frac{I_0 e^{-\mu t}}{4}\left|\sin(\gamma)\right| p^2}. \qquad (3.13)$$

In contrast, the formula for the direction angle

$$\varphi = \frac{1}{2}\arctan 2(a_1, -b_1) + \frac{\pi}{2},$$

remains the same as the filter deviations do not affect the phase of the intensity profile. This new directive for determining the corrected retardation and transmittance makes it possible to account for systematic errors induced by non-ideal polarization filters. In order to apply these equations in the 3D-PLI data analysis, first the filter properties p and γ need to be determined.

[1] A detailed derivation of the following calculations is presented in Appx. A.2.

3.3 Determination of the Filter Properties

In a first step we aim to determine the degree of polarization which is achieved by the two linear polarizers. For this experiment only the two crossed polarizers are inserted in the LAP and the waveplate is removed. By rotating the analyzer, while the polarizer remains in the default position, the degree of polarization p can be determined. According to the Mueller-Stokes calculus (as described in Sec. 2.1) the resulting intensity profile is described by

$$\begin{aligned} I^p(\rho_k) &= \begin{pmatrix} 1 & 0 & 0 & 0 \end{pmatrix} \mathbf{M}_{\mathrm{pol},x}\left(p, \rho_k + \frac{\pi}{2}\right) \mathbf{M}_{\mathrm{pol},x}(p,0) \begin{pmatrix} I_0 \\ 0 \\ 0 \\ 0 \end{pmatrix} \\ &= I_0/4\left(1 - p^2\cos(2\rho_k)\right). \end{aligned} \tag{3.14}$$

From a measurement of this profile the degree of polarization p can be calculated from the ratio between amplitude a_1^p and average intensity a_0^p by

$$p = \sqrt{\frac{|a_1^p|}{a_0^p}}. \tag{3.15}$$

This measurement was performed with the rotation angle of the analyzer varying from 0° to 178° with a sampling step size of 2°. A *region of interest* (ROI) of approximately 5.5×10^5 pixels in the center of the field of view was evaluated in order to avoid fringe effects from absorbing elements that are visible at the borders of the image (cf. Fig. 3.1b). The average degree of polarization across this region of interest was $p = 0.9832$ with a standard deviation of $\sigma_p = 0.0018$.
Next, the retardance γ of the waveplate needs to be determined, since its behavior for the wavelength of the LED array is not specified. For this purpose, a second quarterwave retarder is used as a sample in a standard measurement. This sample retarder (whose specifications are given in Tab. 3.1) is much more homogeneous compared to the one employed in the LAP and its operating wavelength (532 nm) is almost an exact match to the wavelength of the LED array (529 nm). Hence, when measuring this sample, a retardation value of $\sin(\delta) = 1$ is expected and any deviations from this value are attributed to the incorrect description of retarder properties of the LAP.
In order to determine the retardance of the LAP waveplate, the sample was measured with the standard measurement protocol. For the acquired dataset a least square fit was used to determine a value for γ such that calculating the retardation values of the sample according to Eq. (3.13) resulted in an average of $\sin(\delta) = 1$. Thereby, it was possible to determine the actual retardance of the LAP waveplate to be $\gamma = 0.5061\pi$, which deviates from an ideal quarter waveplate ($\gamma = 0.5\pi$) by 1.2 %.

Operating Wavelength (λ_{ret})	532 nm
Retardation	$\lambda/4$
Retardation Accuracy	$\pm\lambda/300$
Diameter	25.4 mm

Table 3.1: Specifications of the sample retarder (Newport 10RP04-16)

3.4 Discussion of the Polarimetric Calibration

In this chapter, a polarimetric calibration method was developed, which makes it possible to exclude systematic errors in a 3D-PLI measurement with the LAP. These errors are induced by the limited degree of polarization achieved by the employed linear polarizers and the wavelength discrepancy between waveplate and light source. While the pixelwise intensity calibration in Sec. 3.1 makes it possible to correct an inhomogeneous absorption, the polarimetric calibration in Sec. 3.2 assumes a non ideal polarization property which is constant across the whole filter. If the retardation is calculated without the polarimetric calibriation, i.e.

$$\sin(\delta) = \frac{\sqrt{\tilde{a}_1^2 + \tilde{b}_1^2}}{\tilde{a}_0},$$

the retardation measurement in the LAP (assuming $\gamma = 0.5061\pi$ and $p = 0.9832$ as the filter properties) is afflicted with a systematic error ranging between 4.3 % and 5.2 % (cf. Fig. 3.2). This error is corrected by using Eq. (3.13) to determine the retardation value. However, the developed model for the polarization filters does not describe all possible polarimetric effects that can occur in real filters and in the future a more sophisticated calibration might be necessary. A more advanced method could describe the correct Stokes vectors of the PSG and the PSA in every image pixel and for every filter position. This would require a change in the general approach of the 3D-PLI image acquisition and analysis, e.g. towards the data reduction algorithms proposed by Chipan et al. [13, pp. 22.17-22.19].
The developed polarimetric calibration is complementary to the established intensity based calibration and fits well into the current 3D-PLI image processing pipeline. With this method, it is now possible to compensate for the predominant sources of error and to calculate the corrected retardation by Eq. (3.13). Both, the developed polarimetric calibration and the intensity based calibration were applied to all experimental data presented in Chap. 4.

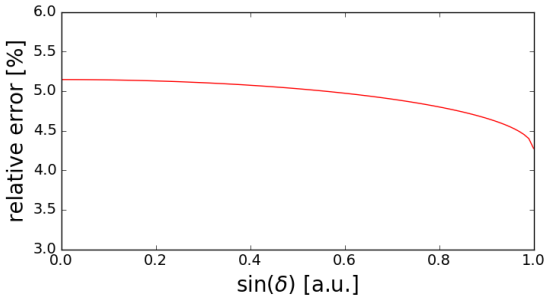

FIGURE 3.2: The relative error that is caused by the imperfect quarter-wave plate depending on the actual retardation of the respective sample. The error that ranges between 4.3 % and 5.2 % can be corrected by employing the polarimetric calibration presented in this chapter.

4

Deriving Fiber Orientations from Tiltable Specimen Stage Experiments

It was discussed in Sec. 2.3 that inferring the inclination of a fiber from the measured data poses a challenging problem in 3D-PLI due to an ambiguity in the theoretical model. Hence, reconstructed orientations in FOMs make it possible to distinguish different fiber pathways visually, whereas the orientation vectors themselves are only reliable in deep white matter regions. In this chapter new approaches are explored to derive the fiber inclination from additional measurements conducted at different positions of a tiltable specimen stage; thereby aiming to facilitate the determination of reliable orientation vectors in transition regions between gray and white matter and in the termination fields.
For the interpretation of the measured data two new algorithms are developed. The first algorithm is well-suited for high throughput applications, as it enables fast computation, but it is also sensitive to noise. The second algorithm employs a maximum likelihood method and is based on a statistical model of the data acquisition process. Thereby, the noise stability is enhanced at the cost of computing time.
Both derived algorithms are verified by simulated datasets in order to compare the results to well-known reference values. After testing the algorithms in this controlled environment, their performance for experimental data is evaluated. Due to the lack of a suitable phantom (an object with a known and well-defined structure that produces the same physical effects in the imaging process as the biological tissue), the extracted orientations are compared with the conjectural course of anatomically visible structures.

4.1 A Review on Ambiguities in 3D-PLI

Determining the inclination of a uniaxial indicatrix from polarization measurements of a birefringent medium (e.g. nerve fiber tissue) is challenging due to mathematical ambiguities which inhibit the direct calculation from measured data. As discussed in Sec. 2.3, these ambiguities are caused by the relation between the measured retardation and the fiber inclination (see Eq. (2.15))

$$\sin(\delta) = \sin\left(\frac{\pi}{2} t_{\mathrm{rel}} \cos(\alpha)^2\right),$$

Parts of this chapter have been adapted from Wiese et al. [76].

which is not bijective in general. The ambiguities of this relation are threefold:

- Since two parameters (t_{rel} and α) are mapped onto only one measurement value, the function cannot be inverted from only one measurement.
- The symmetry of the cos-function conceals the sign of the inclination which is defined on $\alpha \in [-\pi/2, \pi/2]$.
- For $t_{\text{rel}} > 1$ the periodicity of the outer sin-function introduces an additional ambiguity.

These ambiguities are well-known in crystallography applications, where the determination of the indicatrix of a crystal yields information about its structural symmetry. The basic physics of this problem is the same as in 3D-PLI, whereas the concrete imaging concept differs. In the following, developed concepts in crystallography are analyzed for their applicability to 3D-PLI.
Geday et al. [23] have developed a multi-wavelength approach to derive the actual optical retardance δ from the measured retardation $\sin(\delta)$ for samples with $t_{\text{rel}} > 1$. They have demonstrated that by varying the wavenumber $k = \frac{2\pi}{\lambda}$ of the incident light, the induced change in the retardance

$$\frac{\partial \delta}{\partial k} = t\,\Delta n + \frac{tk\partial\,\Delta n}{\partial k}, \tag{4.1}$$

can be utilized to unfold the periodicity of the sine. As shown by Axer et al. [4], the current 3D-PLI preparation of histological sections only leads to values for the relative thickness of $t_{\text{rel}} \leq 1$. Hence, the phase retardance δ can be extracted for 3D-PLI measurements by simply applying the arcsin-function.
Approaches to gain sufficient information to derive the orientation of the optic axis consider additional measurements obtained by either tilting the sample [42, 58] or by means of light-field imaging [56]. Pajdzik et al. have demonstrated in a proof-of-concept experiment that by employing a tiltable specimen stage the inclination of quartz crystals can be determined [58]. In their study, a non-linear model for the change in retardation has been developed based on a geometrical description of the tilting process. The model was fitted to the retardation data acquired for several different positions of the tiltable specimen stage revealing the inclination of the analyzed crystal. Their approach was designed for the analysis of single crystals and is not feasible for a high throughput application in image processing, where such an analysis would need to be conducted in every pixel.
Following a different concept, Oldenbourg et al. [56] have developed a polarized light-field microscope[1], which is capable of capturing the birefringence information of the sample from different perspectives in a single shot. However, their analysis of the light field data followed a manual evaluation of the conoscopic view. It was argued that in order to analyze complete images comprising typically 120×120 microlenses, fast and robust processing algorithms still need to be developed [56].
For the investigation of nerve fiber architecture, previous studies by Axer et al. [4] utilized a statistical approach to determine t_{rel} from the distribution of retardation values over a whole brain section (described in Sec. 2.3). This approach presumes a uniform relative thickness across the whole section and does not take local variations in myelin density into account. Hence, their method allows the correct determination of orientations in deep white matter regions where little change in the relative thickness occurs.

[1] Further details on polarization sensitive light-field imaging can be found in Sec. 5.1.

Transitions at the white matter / gray matter border and gray matter regions on the other hand cannot be interpreted correctly with this approach.
Kleiner et al. [42] addressed the challenge of solving the sign ambiguity of the inclination in 3D-PLI. By mounting histological brain sections onto a tiltable specimen stage and analyzing the obtained retardation data (which included a Markov Random Field approach to correct for statistical outliers), the sign has been successfully determined. However, the study did not investigate how this approach can be utilized to account for variations in t_{rel} in order to improve the inclination reconstruction.

4.2 Basic Theory of the Tiltable Specimen Stage Data Acquisition

The general concept of complementing the *planar* (i.e. the not tilted) measurement with data acquired from a tilted specimen stage can be illustrated by considering the functional relationship $\alpha, t_{\text{rel}} \rightarrow \sin(\delta)$, as depicted in Fig. 4.1. It is shown that for the measurement of a certain retardation value, the corresponding inclination is ambiguous in terms of the sign and the relative thickness t_{rel}. By tilting the sample (i.e. the unknown inclination α is varied by a well-defined amount) additional information about the local gradient $\frac{\partial \sin(\delta)}{\partial \alpha}$ is obtained. Collecting this information yields for $\alpha \in (-\pi/2, \pi/2)$ and $t_{\text{rel}} \in (0, 1]$ the bijective transformation

$$\alpha, t_{\text{rel}} \rightarrow \sin(\delta), \frac{\partial \sin(\delta)}{\partial \alpha},$$

which needs to be inverted in order to get the desired information[2].
In order to turn this approach into a viable image analysis, it is necessary to apply well-defined changes to the inclination and to develop a directive on how to analyze the

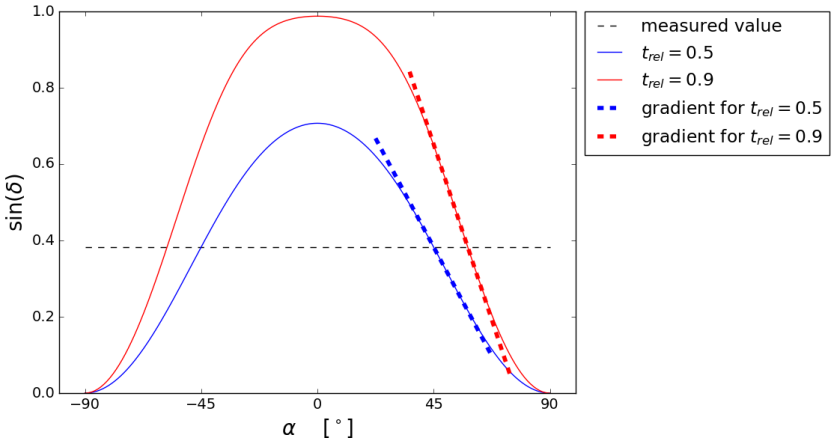

FIGURE 4.1: Displayed is the dependency of the retardation $\sin(\delta)$ on the inclination value α. For a retardation value in the planar measurement (e.g. $\sin(\delta) \approx 0.4$), the inclination that is reconstructed depends on the relative thickness t_{rel}. It is only by measuring the local gradient that it is possible to distinguish between the different cases.

[2]The proof for bijectivity is presented in Appx. A.3.

resulting datasets. A tiltable specimen stage is capable of applying a rotation to a fiber orientation vector $\mathbf{x}$ that can be expressed by a 3×3 rotation matrix $\mathbf{R}$ resulting in a tilted orientation vector

$$\mathbf{x}' = \mathbf{R}\ \mathbf{x}. \tag{4.2}$$

The exact composition of the rotation matrix depends on the employed tilting system. In our case the tiltable specimen stage of the LAP is realized by a nested two-axis system that can be rotated around the y-axis by an angle of $-8° \leq \tau_y \leq 8°$ and then around the x-axis by an angle of $-8° \leq \tau_x \leq 8°$. Hence, the matrix can be described by

$$\mathbf{R}(\tau_x, \tau_y) = \begin{pmatrix} 1 & 0 & 0 \\ 0 & \cos(\tau_x) & -\sin(\tau_x) \\ 0 & \sin(\tau_x) & \cos(\tau_x) \end{pmatrix} \cdot \begin{pmatrix} \cos(\tau_y) & 0 & \sin(\tau_y) \\ 0 & 1 & 0 \\ -\sin(\tau_y) & 0 & \cos(\tau_y) \end{pmatrix}. \tag{4.3}$$

For the approaches presented in Sec. 4.3 and Sec. 4.4, the planar measurement is generally supplemented by N_t measurements, each with a different tilted position of the specimen stage. In the following, quantities for the planar measurement are indicated by an index 0 to distinguish them from the tilted measurements. The latter are indexed with i, whereas $i \in [1, 2, \ldots, N_t]$ refers to the variable for the respective position of the tiltable specimen stage defined by a rotation matrix $\mathbf{R}_i$.
Applying a rotation to the orientation vector $\mathbf{x}_0$ written in spherical coordinates leads to the tilted orientation vector

$$\mathbf{x}_i = \begin{pmatrix} \cos(\alpha_i)\cos(\varphi_i) \\ \cos(\alpha_i)\sin(\varphi_i) \\ \sin(\alpha_i) \end{pmatrix} = \mathbf{R}_i \begin{pmatrix} \cos(\alpha_0)\cos(\varphi_0) \\ \cos(\alpha_0)\sin(\varphi_0) \\ \sin(\alpha_0) \end{pmatrix}. \tag{4.4}$$

This new orientation vector represents the spatial orientation of the indicatrix relative to the imaging system. Hence, the measured retardation and direction values change respectively, yielding a set of measured direction angles φ_i and retardations $\sin(\delta_i)$ for every image pixel. Deriving the inclination from this data requires a suitable algorithm. In Sec. 4.3 and Sec. 4.4 two different algorithms are presented that are capable of determining the parameters of the fiber model (α, φ, t_{rel}) from the additional data.
For a practical application of the described theory, experimental effects must also be considered. It has been discussed by Pajdzik et al. [58] that due to refraction at the sample surface, the external rotation applied by the tiltable specimen stage is not equal to the actual rotation of the sample relative to the path of light. When considering a sample tilted by an angle τ_{ext}, this refraction causes the light to enter the sample at a different angle, which can be calculated according to Snell's law[3]

$$\frac{\sin(\tau_{int})}{\sin(\tau_{ext})} = n_{sample}. \tag{4.5}$$

Here, n_{brain} denotes the refractive index of the brain tissue and τ_{int} is the internal tilting angle which is relevant to the interpretation of birefringence information (i.e., which needs to be used for τ in the analysis in Sec. 4.3). For the average refractive index a value of $n_{sample} \approx 1.45$ is presumed, based on optical studies of brain tissue by Vidal et al. [17]. Considering the maximal tilting angle $\tau_{ext} = 8°$ of the employed specimen stage leads to a reduced internal angle of $\tau_{int} \approx 5.5°$.
Due to tilting, it also needs to be considered that the path length through the tissue is

[3] Birefringence effects that could cause a different refraction for the ordinary and extraordinary ray are negligible here due to the low birefringence of $\Delta n \approx 10^{-2}$.

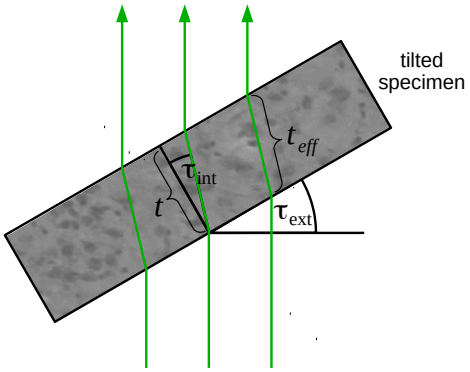

FIGURE 4.2: When applying an outer rotation specified by the angle τ_{ext} to the specimen, refraction at the specimen surface reduces this angle to the internally observable τ_{int}. Furthermore, the length of the light path through the specimen is increased from t to $t/\cos(\tau_{int})$

slightly elongated [58]. In Fig. 4.2, the distance of the lower and upper surface of the tilted sample is set apart by a distance t. As the sample is tilted, the path of light is changed resulting in a longer distance $t/\cos(\tau_{int})$. Since the retardance is proportional to the optical path length, this effect can be reversed by rescaling the measured retardance according to $\delta_i \cos(\tau_{int})$ for all tilted measurements (i.e. $i \neq 0$).
To improve the readability of following formulas, these experimental adjustments are implicitly used; the tilting angle τ refers to the internal tilting angle $\tau = \tau_{int}$ and the phase retardance δ_i will be considered as already corrected, i.e. multiplied by the factor $\cos(\tau_{int})$ in a preprocessing step.
Imaging a tilted sample leads to parallax effects, which have been co-registered for all experimental data in this study. Co-registration was achieved by a projective transformation, which was generated from matching scale-invariant features (cf. [7]) between the tilted and planar images.

4.3 An Analytical Solution to Calculate the Inclination of a Uniaxial Indicatrix

Previous work by Pajdzik et al. on deriving the inclination of a birefringent medium from tilting measurements have focused on nonlinear regression to evaluate the measured retardations [58]. In this section, it is demonstrated that given a suitable coordinate system it is possible to find an analytical solution to the problem. This approach complies with the demands of high throughput image processing in 3D-PLI.

4.3.1 Deriving the Inclination from Measurement Data

The Tilting Coordinate System

For the purpose of the mathematical analysis, first a suitable definition of the rotation is needed, which describes the tilting process. Kleiner et al. [42] introduced a coordinate system where the angle ψ defines the direction in which the sample is tilted, while the angle τ defines the actual tilt of the specimen stage. This rotation is described by the

tilting matrix

$$\mathbf{R}_i = \mathbf{R}^z(\psi_i)\mathbf{R}^y(\tau)\mathbf{R}^z(-\psi_i),$$

where the tilting direction is defined in equidistant steps as

$$\psi_i = 2\pi\frac{i-1}{N_t} \qquad \text{with } i \in [1, 2, \ldots, N_t]. \tag{4.6}$$

This definition is necessary for the analysis developed in the next section, yet the specimen stage in the experiment can only be tilted around the x- and y-axis by an angle of $\pm 8°$, which is described by a tilting matrix

$$\mathbf{R} = \mathbf{R}^x(\tau_x)\mathbf{R}^y(\tau_y). \tag{4.7}$$

Here, τ_x denotes the rotation around the x-axis and τ_y the rotation around the y-axis, respectively. It can be shown that these two transformations cannot be converted into each other, i.e. for an arbitrary tilting (ψ, τ) it is not possible to find a (τ_x, τ_y), so that

$$\mathbf{R}^z(\psi_i)\mathbf{R}^y(\tau)\mathbf{R}^z(-\psi_i) = \mathbf{R}^x(\tau_x)\mathbf{R}^y(\tau_y). \tag{4.8}$$

In the experiment, there are, however, two approaches to work around this issue. While a general solution to Eq. (4.8) does not exist, it is possible to find one for the special case $N_t = 4$ (as the specimen stage is only rotated around one of the two axes). A second approach considers that the analysis presented here is purely based on the retardation values, meaning only the z-component of the orientation vector is relevant. Hence, it is sufficient to ensure that the third row of the matrices in Eq. (4.8) is identical, which is achieved by choosing[4]

$$\begin{aligned}\tau_x &= -\arcsin(\sin(\tau)\sin(\psi)),\\ \tau_y &= \arctan(\tan(\tau)\cos(\psi)).\end{aligned}$$

Retrieving the Inclination from Retardation Measurements

For the derivation of the inclination angle from the acquired retardation dataset, first it is derived how the tilting influences the measured retardation and then it is demonstrated how this enables the reconstruction of the inclination.
Tilting the sample by an angle τ in the tilting direction ψ_i results in a three-dimensional rotation of the fiber orientation vector described by

$$\mathbf{x}_i = \mathbf{R}^z(\psi_i)\mathbf{R}^y(\tau)\mathbf{R}^z(-\psi_i)\mathbf{x}_0. \tag{4.9}$$

Considering the vector $\mathbf{x}_0$ in spherical coordinates, the z-component of the rotated vector $\mathbf{x}_i$ is given by

$$\sin(\alpha_i) = \sin(\tau)\cos(\alpha_0)\cos(\psi_i - \varphi_0) + \cos(\tau)\sin(\alpha_0), \tag{4.10}$$

where α_i denotes the inclination of a fiber of the i-th tilting measurement. Using the identity $\cos(\alpha_i)^2 = 1 - \sin(\alpha_i)^2$, this result can be inserted into the relation of the phase retardance Eq. (2.15) yielding

$$\delta_i = \frac{\pi}{2}t_{\text{rel}}\left[1 - (\sin(\tau)\cos(\alpha_0)\cos(\psi_i - \varphi_0) + \cos(\tau)\sin(\alpha_0))^2\right]. \tag{4.11}$$

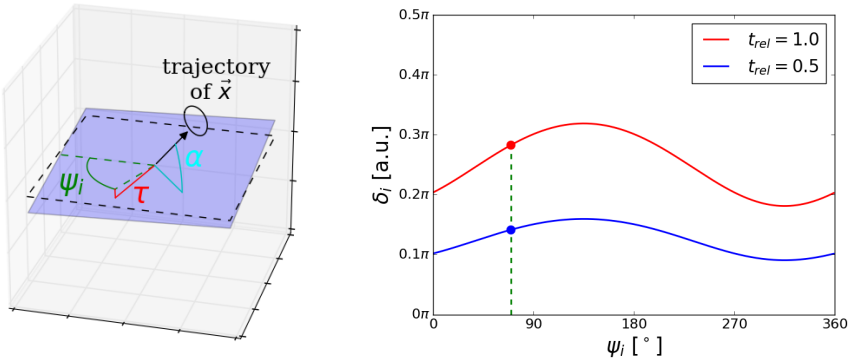

(a) (b)

FIGURE 4.3: When tilting the specimen in different directions ψ, the orientation vector $\mathbf{x}$ precesses on a trajectory depicted in (a). As this changes the inclination angle of the vector relative to the optic axis, the measured phase retardance δ oscillates as shown in (b).

This equation means that tilting the specimen stage in different directions specified by the angles ψ_i results in a sinusoidal oscillation of the phase retardance obtained from the 3D-PLI measurement, as depicted in Fig. 4.3. While the offset of this oscillation relates to the retardance of a planar measurement, the amplitude of this dataset carries complementary information which is similar to the gradient discussed in Sec. 4.2. In order to extract the inclination, a Fourier analysis is performed across δ_i yielding the coefficients[5]

$$a_{\delta,1} = \frac{2}{N}\sum_{i=1}^{N_t} \delta_i \cos(\psi_i) = \pi t_{\text{rel}} \sin(\tau)\cos(\tau)\sin(\alpha_0)\cos(\alpha_0)\cos(\varphi_0), \tag{4.12}$$

$$b_{\delta,1} = \frac{2}{N}\sum_{i=1}^{N_t} \delta_i \sin(\psi_i) = \pi t_{\text{rel}} \sin(\tau)\cos(\tau)\sin(\alpha_0)\cos(\alpha_0)\sin(\varphi_0). \tag{4.13}$$

This information gained from the tilting measurements can now be combined with the information from the planar measurement from Eq. (2.16)

$$\delta_0 = \frac{\pi}{2} t_{\text{rel}} \cos^2(\alpha_0).$$

Thereby it is possible to calculate the inclination angle α_0 from the information obtained by the planar measurement (δ_0), information obtained by the tilted measurement ($a_{\delta,1}, b_{\delta,1}$) and the knowledge about the applied tilting (τ):

$$|\alpha_0| = \arctan\left(\frac{\sqrt{{a_{\delta,1}}^2 + {b_{\delta,1}}^2}}{2\delta_0 |\sin(\tau)\cos(\tau)|}\right). \tag{4.14}$$

This formula represents a method for the analytical determination of the inclination regardless of the parameter t_{rel}. Hence, the reconstruction is no longer biased by variations in myelination of fibers or the local fiber density in the tissue.

[4]For the detailed derivation refer to Appx. A.4.

[5]The retardance signal δ_i also yields second order Fourier coefficients $a_{\delta,2}, b_{\delta,2}$ which, however, are not needed in the following context. A comprehensive derivation can be found in Appx. A.5

Finally, to obtain the correct fiber orientation, it is necessary to determine the sign of the inclination. The sign can be calculated by

$$\text{sign}(\alpha_0) = \text{sign}(a_{\delta,1}\cos(\varphi_0) + b_{\delta,1}\sin(\varphi_0)) \cdot \text{sign}(\tau), \tag{4.15}$$

using the fiber direction angle from the planar measurement φ_0 and the information provided by the tilted measurements in $a_{\delta,1}$ and $b_{\delta,1}$.
In addition to the fiber orientation, it is also interesting to calculate the relative thickness t_{rel}. This scalar contains structural information about the tissue and is related to the degree of myelination and the fiber density in the analyzed pixel. Once the inclination has been determined, this structure parameter can be computed according to

$$t_{\text{rel}} = \frac{2\delta_0}{\pi\cos(\alpha_0)^2}. \tag{4.16}$$

These theoretical findings provide a directive to determine the exact and unambiguous inclination angle. Since the Fourier analysis is a linear combination of the tilted retardation maps, the inclination can be calculated without the need for iterative and computationally time consuming model fitting. However, it is important to note that while the analytic solution to this problem is straightforward for ideal signals, it is necessary to determine its numerical stability when dealing with small signals affected by noise, as present in gray matter brain regions. The influence of noise is examined in the next section on the basis of simulated datasets, while Sec. 4.3.3 deals with the validation for experimental datasets.

4.3.2 Validation for Simulated Datasets

In this section the numerical stability of the proposed analytical solution is examined. More precisely, recorded images and the corresponding retardation signals are affected by noise, which can cause deviations between the underlying ground truth and the solution found by Eq. (4.14). In biological samples the underlying ground truth is generally unknown and can at best be estimated from indicators such as the macroscopically visible structure or other imaging techniques. To date, artificial phantoms that could be used to validate the 3D-PLI measurement principle and data analysis do not exist. Therefore, a simulation approach based on the current theory of 3D-PLI (see Sec. 2.3) was chosen for which a ground truth can be arbitrarily defined.

Methods

For the simulation an initial orientation vector $\mathbf{x}_{\text{sim},0}$ was specified which is defined by an inclination $\alpha_{\text{sim},0}$ and a direction angle $\varphi_{\text{sim},0}$. For this vector the simulated intensity profile of the planar measurement was calculated according to Eq. (2.24):

$$I_k = \frac{I_0 e^{-\mu t}}{4}\left(1 + \sin\left(\frac{\pi}{2}t_{\text{rel}}\cos\left(\alpha_{\text{sim},0}\right)^2\right)\sin\left(2\rho_k - 2\varphi_{\text{sim},0}\right)\right).$$

For the relative thickness of the simulated sample, values of $t_{\text{rel}} = 0.5$ and $t_{\text{rel}} = 0.1$ were chosen to represent tissue samples within the white matter and the gray matter, respectively. The average intensity was chosen to be $\frac{I_0 e^{-\mu t}}{2} = 5000$, which corresponds approximately with the measured transmittance of white matter tissue. Noise was added to each of the 18 values of the intensity profile according to the Poisson distribution with

an expectation value equal to the respective intensity value of the simulated profile. The Poisson distribution was chosen as it is the best model for the noise caused by the randomized detection of photons in a camera sensor [77]. The original vector was then rotated by four tilting matrices, so that a set of tilted vectors $\mathbf{x}_{\mathrm{sim},i}$ was obtained according to Eq. (4.9). Each of these four vectors simulates the orientation for a different position of the tiltable specimen stage. For every simulated position of the tiltable specimen stage a corresponding intensity profile was calculated as it had been for the planar position. For these noisy signals the transmittance, retardation and direction values were calculated and according to the developed analysis the inclination was computed. From the developed analysis a calculated orientation vector $\mathbf{x}_{calc}$ was obtained. This vector differed from the original vector due to the influence of noise during image acquisition. For the comparison to the *"ground truth"*, a suitable measure is given by the acute angle β between these two vectors $\mathbf{x}_{sim}$ and $\mathbf{x}_{calc}$. It can be calculated by

$$\beta = \arccos\left(\frac{|\mathbf{x}_{sim} \cdot \mathbf{x}_{calc}|}{|\mathbf{x}_{sim}|\,|\mathbf{x}_{calc}|}\right). \tag{4.17}$$

This measure is well-suited for the comparison between ground truth and result because it respects the symmetry of the problem, i.e. two vectors oriented antiparallel to each other describe the same course of a nerve fiber. In this example, the angle between the two antiparallel vectors would be 180°, while the acute angle is $\beta = 0°$. In order to evaluate the average effect of noise rather than statistical outliers, the simulation was repeated 100 times for every initial vector and the average acute angle $\bar{\beta}$ was calculated.

Results

Fig. 4.4 shows the average angular deviation for different initial conditions. The coordinates on the sphere represent the different initial orientations of the vector $\mathbf{x}_{sim}$, while the coloring visualizes the respective average angular deviation $\bar{\beta}$ for this vector. Each sphere was simulated for a different relative thickness. Fig. 4.4a shows the resulting deviation for white matter regions with a relative thickness of $t_{\mathrm{rel}} = 0.5$. In Fig. 4.4b the deviations from the initial vector are depicted for a relative thickness of $t_{\mathrm{rel}} = 0.1$ representing gray matter regions.
In Fig. 4.4a it can be seen that most fiber orientations of the simulated white matter tissue could be reconstructed with an error of up to $\bar{\beta} \approx 1.5°$. The direction angle of the initial fiber orientation had no relevant effect on the accuracy. Fibers with an initial inclination of $\alpha_{\mathrm{sim}} \approx 0°$ could only be reconstructed with a slightly lower accuracy of $\bar{\beta} \approx 3°$. For an initial fiber inclination of $\alpha_{\mathrm{sim}} \geq 85°$, the accuracy dramatically decreased and at an initial inclination angle of exactly $\alpha_{\mathrm{sim}} = 90°$ the error reached a value of $\bar{\beta} \geq 30°$. This large statistical error means that the reconstructed fiber orientation was almost entirely random, making it impossible to draw any conclusions about the initial fiber orientation.
In the case of the second scenario, which simulated a region where fibers transition into the gray matter, overall the accuracy of the reconstruction was decreased compared to the first scenario, while it behaved in a similar fashion. The reconstruction for most initial vectors was afflicted with a statistical error of $\bar{\beta} \approx 8°$. For an initial inclination angle of $\alpha_{\mathrm{sim}} \approx 0°$ this error increased up to $\bar{\beta} \approx 11°$. For steep fibers with an inclination of $\alpha_{\mathrm{sim}} \geq 80°$ it was impossible to reconstruct their orientation by the developed algorithm with a reasonable accuracy.

Discussion

The simulation showed that in general the algorithm is capable of recovering the parameters of the original fiber structure, with very high (in white matter regions) to reasonable accuracy (in gray matter regions). The algorithm makes it possible unravel the co-jointly measured inclination of the fiber structure and relative thickness of the tissue, without making any additional presumptions such as a constant parameter t_{rel}. However, the simulated datasets also revealed that fibers oriented almost perpendicularly to the image plane cannot be reconstructed. This limitation originates from the retardation characteristic depicted in Fig. 4.1. As was pointed out in Sec. 4.2, the relationship

$$\alpha, t_{\text{rel}} \rightarrow \sin(\delta), \frac{\partial \sin(\delta)}{\partial \alpha},$$

is bijective on the intervals $\alpha \in (-\pi/2, \pi/2)$ and $t_{\text{rel}} \in (0, 1]$. For exactly $|\alpha| = 90°$ it is not bijective since we obtain $\delta = 0$ and $\frac{\partial \sin(\delta)}{\partial \alpha} = 0$ for all possible values of t_{rel}. While this issue is theoretically only relevant for exactly one orientation vector, in practice, the presence of noise also leads to a poor reconstruction for all adjacent vectors. In Fig. 4.4, it can be seen that a lower relative thickness (and thus a lower signal-to-noise ratio of the recorded data) leads to more orientation vectors being affected. The loss in accuracy that was observed for an original fiber inclination of $\alpha = 0°$, can also be explained with the retardation characteristic. For this particular fiber inclination, neighboring inclinations only exhibit small changes in the gradient and the retardation value. Due to noise these small differences are more difficult to distinguish than for other fiber inclinations (e.g. $\alpha = 45°$).
The presented approach to reconstruct the fiber orientations is solely based on the model for the measured retardation value. However, changes in fiber direction angle φ when tilting the sample, also contain information on the fiber inclination. This additional information is not exploited yet. Hence, to overcome the limitations of the algorithm particularly for steep fibers, in Sec. 4.4 a second approach is presented to analyze the dataset of tilted measurements, including available information in the measured direction angles.

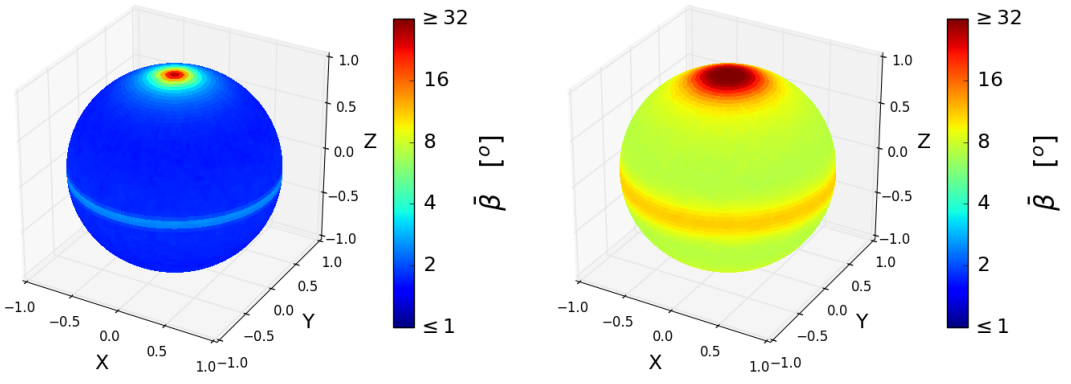

(a) $t_{\text{rel}} = 0.5$ (b) $t_{\text{rel}} = 0.1$

FIGURE 4.4: The spheres visualize how well any given orientation vector can be reconstructed by the algorithm, for two different values of t_{rel}. Every point on the sphere encodes the accuracy $\tilde{\beta}$ for the respective orientation vector.

4.3.3 Validation for Experimental Datasets

After analyzing the performance of the algorithm with simulated datasets, this section is dedicated to providing the proof of principle on experimental datasets. As already discussed, a phantom for 3D-PLI does not exist; however, by validating the computed vectors with different indicators of the fiber orientation, it is possible to substantiate the working principle of the algorithm.

Methods

In a first experiment, the acquired data of a single brain section is processed in order to demonstrate the working principle of the algorithm. Since it is of particular interest whether fiber orientations in the transition regions to the cortex can be reconstructed, the results were complemented by a close-up recorded with the polarizing microscope. This microscopic image adds valuable information since the fiber architecture in the transition regions is clearly visible in the retardation map, independently of orientations calculated by an algorithm.
To verify if the retardation values change when tilting the sample according to the described theory, the standard recording procedure was varied. Instead of conducting a standard LAP measurement with $N_t = 4$ different positions of the tiltable specimen stage, the sampling rate was increased to $N_t = 72$ different positions of the tiltable specimen stage. Hence, ψ_i is varied by a step size of 5°, resulting in a fine sampling of the retardation values. By determining the inclination and relative thickness in a single pixel and then computing the expected changes in the retardation value, it is possible to compare theory and experiment.
In order to evaluate the reconstructed z-components of the orientation vectors in the white matter, they were compared to the anatomical visible course of the sagittal stratum. For this purpose, a set of 220 consecutive sections from the right hemisphere of a human brain was analyzed. The brain sections were measured according to the standard 3D-PLI measurement protocol (i.e. every section is measured in the default position and $N_t = 4$ tilted positions of the specimen stage) and co-registered as described in Sec. 2.5. To extract the anatomical structure, the retardation maps of the sections were stacked and virtually resliced along the z-axis at two positions, depicted in Fig. 4.8a. Based on the retardation value, the vector field was masked along the visible outlines of the sagittal stratum.

Results

The FOM generated by the developed tilting analysis displays consistent fiber orientation for the transition from white to gray brain matter and within the gray matter. In contrast to the FOMs created by the standard 3D-PLI analysis (cf. Sec. 2.3), it can be seen in Fig. 4.5a that fiber orientations in the cortex are no longer biased towards the z-axis. It is evident that the reconstructed orientations in the gray matter are as diverse as in the white matter. In addition to the FOM, the developed analysis provides a t_{rel}-map depicted in Fig. 4.5b. This new modality contains complementary information about the fiber architecture, e.g. the distinction between white and gray brain matter. For visualization purposes this new parameter map can be combined with the FOM through multiplication. Such a weighted FOM encodes the orientation by color as before, while the structure parameter t_{rel} is encoded in the brightness (cf. Fig. 4.5c).

For this particular brain section only few structures seem to be orientated out of the imaging plane, expressed by the overall lack of blue coloring. It can be seen that blue coloring in some cases coincides with a very high value in t_{rel}. Such regions can often be found at the intersection of two fiber bundles (cf. arrows in Fig. 4.5a and Fig. 4.5b). The reconstruction of fiber orientations for a transition region between gray and white matter is shown in Fig. 4.6. In the microscopic retardation map Fig. 4.6a the fibers in the gyrus are bundled in the lower right corner and then fan out into the cortex. In the lower resolved retardation map, generated by the LAP (Fig. 4.6b background), this is only visible as a decrease of the overall retardation. The fiber orientations derived by the new algorithm match well with the microscopic structures. Though individual fibers cannot be observed at the LAP resolution, the general fiber architecture can still be recovered for the transition regions between white and gray matter and for the termination fields in the gray matter.

To evaluate how well the experimental data fits the theoretical model, retardation values were measured for $N_t = 72$ different positions of the tiltable specimen stage. Fig. 4.7 shows the changes in retardation when tilting the sample for two exemplary pixels (cf. red dots in Fig. 4.5b). The recovered parameters from this data were $\alpha = -52.3°$ and $t_{\text{rel}} = 0.74$ for the first pixel (red line) and $\alpha = 17.7°$ and $t_{\text{rel}} = 0.26$ for the second pixel (blue line). Given these parameters the lines show the respective theoretical models describing the expected retardation values for the different positions of the tiltable specimen stage. The match between theoretical model and measured data points was measured by the square root of the mean square error, with $\Delta \sin(\delta) = 0.012$ for the first and $\Delta \sin(\delta) = 0.008$ for the second pixel. Apart from statistically distributed errors, there was also a distinct phase offset between theoretical curve and experimental data in the first pixel (red curve) and an offset in the retardation value for the second pixel (blue curve).

For the evaluation of the z-component of fiber orientation vectors the orientations were compared to the anatomical course of the sagittal stratum that is visible in retardation maps. Fig. 4.8 shows the retardation dataset of 220 consecutive brain sections of the right hemisphere. Fig. 4.8a gives an overview of the hemisphere. The colored lines indicate where the dataset was virtually resliced along the z-axis to analyze the z-component of the orientation vectors.

The resliced retardation map in Fig. 4.8d shows a part of the sagittal stratum that has an inclination angle of approximately $\alpha = 60°$ with respect to the sectioning plane. The lower retardation values compared to the surrounding fiber bundles are due to inclined fibers. Most of the reconstructed vectors in Fig. 4.8d are well aligned with the outer boundaries of the fiber bundle that are made visible by the retardation map.

The resliced retardation map in Fig. 4.8c features the sagittal stratum at a different position. The boundaries of this part of the sagital stratum, which are visible in the retardation map, suggest that the fiber tract is now aligned almost perpendicularly to the imaging plane. The majority of the extracted fiber orientations in the upper part match reasonably well with this predicted orientation. In the lower part, however, the orientation vectors are dispersedly oriented and do not follow any path. When zooming in on the upper part of the tract, it also becomes visible that two distinct fiber orientations are present (cf. Fig. 4.8b). The left-hand side features vectors oriented along the z-axis, as expected, while the vectors on the right-hand side also display a component oriented along the y-axis[6]. Additionally, in each resliced view registration artifact are visible, which do not affect the analysis as every calculation is performed pixelwise and is not dependent on the alignment of the sections.

[6]For these resliced views the y-axis corresponds to the axis perpendicular to the image plane.

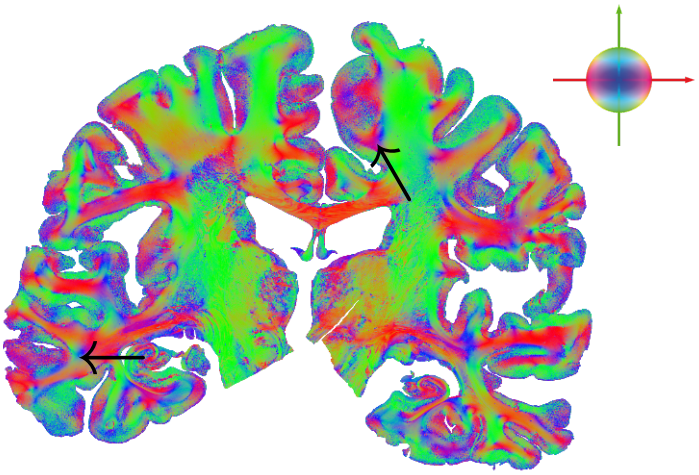

(a) Fiber orientation map generated with the results of the new algorithm. It can be seen that the orientations are continuous from white to gray matter

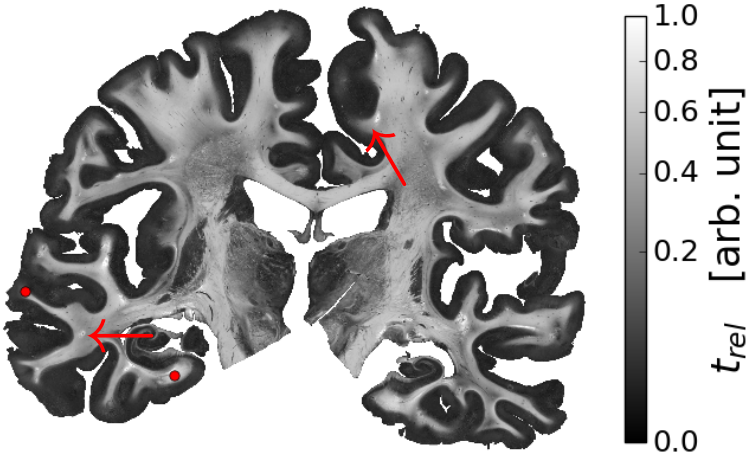

(b) Visualization of the parameter t_{rel}. This modality makes it possible to distinguish between white and gray matter.

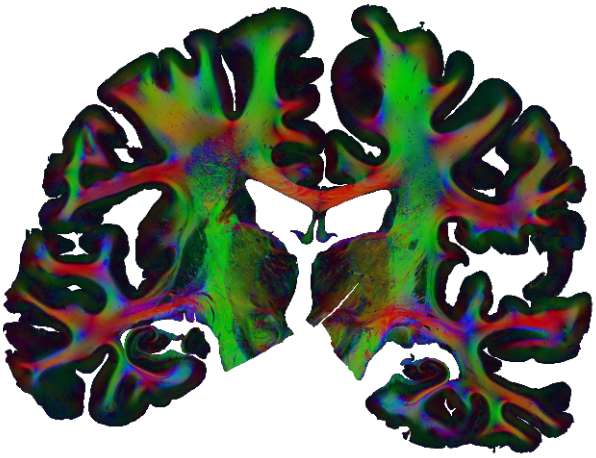

(c) Enhanced fiber orientation map that encodes orientations by color and t_{rel} by brightness. This visualization combines both sets of information in a single map.

FIGURE 4.5: The different modalities that can be generated from the new algorithm. It is possible to separate the inclination and relative thickness and even display both sets of information in one map, while still being able to distinguish them.

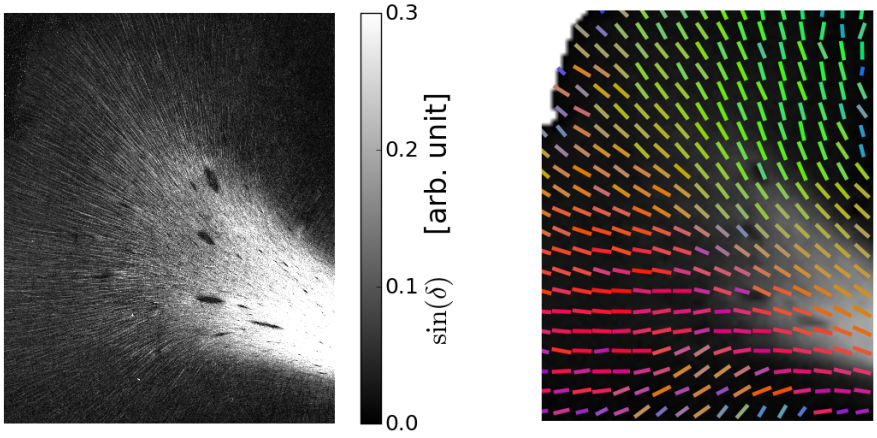

(a) Microscopic retardation map of the ROI. Individual fibers within the plane are visible.

(b) Vector field generated by the algorithm. Only the orientation of every 4th pixel is depicted.

FIGURE 4.6: Comparison of the fiber structure that is visible in a retardation map generated with the PM (a) and the recovered fiber orientations with the LAP (b). Visualized is a ROI featuring a single gyrus with a thick fiber bundle that fans out and terminates in the cortex.

Discussion

So far, tracing fibers from white brain matter into the regions of their termination fields in the cortex has been reserved to microscopic studies. While in microscopic datasets individual fibers are visible in the gray matter, in LAP datasets these fibers could previously not be traced reliably. For the first time, it is now possible to resolve the ambiguous interpretation of retardation maps by collecting additional data from measurements with a tilted sample. Though individual fibers cannot be observed in the lower resolved LAP images, the inferred orientation vector field is in agreement with the microscopically observed architecture (cf. Fig. 4.6).
It has been demonstrated that the developed algorithm is capable of separating the structure parameter t_{rel} and the fiber inclination angle α. Thereby, two complementary maps were generated. The created FOM is not afflicted with a bias anymore, which had been caused by presuming a constant t_{rel} across the whole brain section in previous studies (cf. [4, 46]). Discontinuities in the fiber orientations at the border between white and gray matter are no longer present; instead it is now possible to trace fibers from the white matter fiber bundles to the termination fields in the cortex. The generated t_{rel}-map is a measure for the birefringence of the examined material. It is related secondarily to other quantities such as fiber density[7]. This dependency could provide a valuable tool for a statistical description of the terminations of myelinated fibers in the cortex. However, further research will be necessary to precisely understand the link between these quantities and avoid misinterpretation.
The brain section in Fig. 4.5 displays small regions which are afflicted with interpretation artifacts. These regions were found at the intersection of two different in-plane fiber bundles. At such an intersection, the signals of the differently oriented fibers are superimposed and thereby cancel each other out. In the fiber orientation map such

[7]The basic reasoning behind this relation is that the more fibers are present, the more birefringent material is in the optical path, which adds up to the total effect that is being observed.

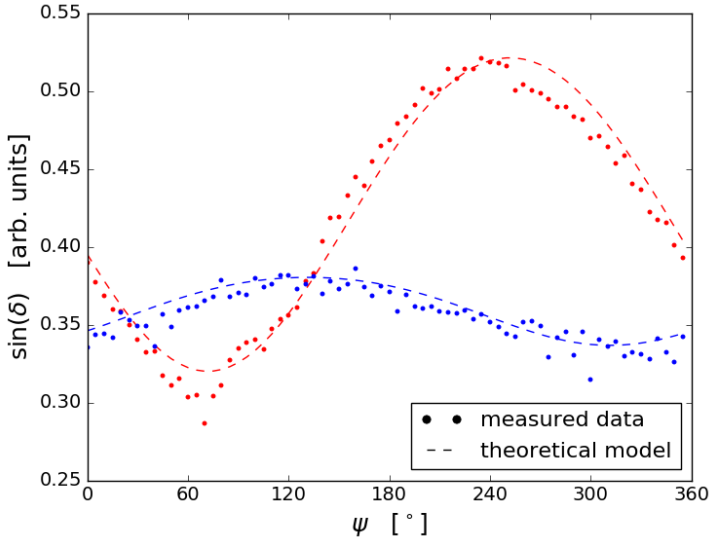

FIGURE 4.7: Retardation values in two independent pixels (which are highlighted in Fig. 4.5b) for $N_t = 72$ different positions of the tiltable specimen stage. Apart from small distortions, the experimental data oscillates as predicted by the theoretical model.

regions were represented by unusually high t_{rel}-values and an orientation perpendicular to the image plane. This type of artifact cannot be avoided since a fiber crossing cannot be represented by a vector field model that only allows one vector for each pixel. Such a crossing scenario is represented by a low retardation value which resembles the signal for a perpendicularly oriented fiber. In order to resolve this issue, a new fiber model will be needed to represent a multi directional fiber architecture within a single pixel. Similar representations are known from HARDI measurements in dMRI (however, at a much lower scale) and the recently introduced pliODF, for which the fiber structure in a voxel is represented by orientation distribution functions. These functions are statistical representations of the underlying fiber orientations that give information about the percentage of fibers oriented into any possible direction [6]. The more difficult challenge, however, will be how to relate the parameters of such a model to the actual measurement data.

The experimentally observed retardation values were assessed in individual pixels and conformed with the theoretically predicted oscillation (cf. Eq. (4.11)) of the retardation signal within a reasonable margin of error (cf. Fig. 4.7). This result confirms the premise of the approach quantitatively, thereby providing further evidence for the employed model. Though the retardation values behave as predicted when the sample is tilted, this verifies the self-consistency of the retardation model, while the direct validity of the derived fiber orientations has yet to be proven.

Achieving a direct validation of calculated orientation vectors is impeded by lack of information about the actual fiber orientations in the examined brain tissue. Since phantoms for 3D-PLI have not been developed yet, in this study a reconstructed brain volume was used, consisting of 220 consecutive sections. In this brain volume, the overall course of the sagittal stratum was estimated by assessing the retardation contrast. This approach has several pitfalls. For a heterogeneous structure, the overall orientation of the bundle might not be equivalent to the orientations in every single point (e.g. imagine a rope like structure where the individual yarns are twisted and their tangential orientations differ from the primary course of the rope). Another issue is that the cross sections

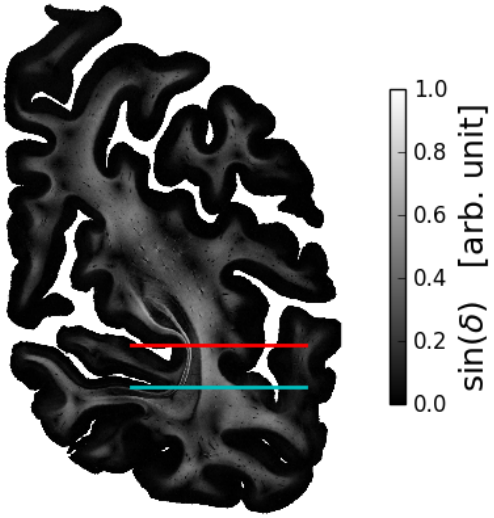

(a) Overview of the analyzed hemisphere. The colored lines indicate the position of the resliced views in (c) and (d).

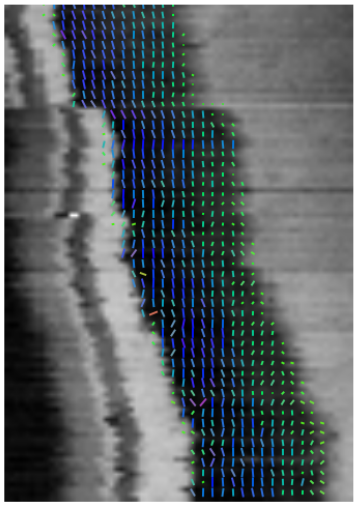

(b) Zoom of the vector field in (c). Every 2nd vector is depicted. 2 distinct structures are visible, one oriented along the z-axis the other along the y-axis.

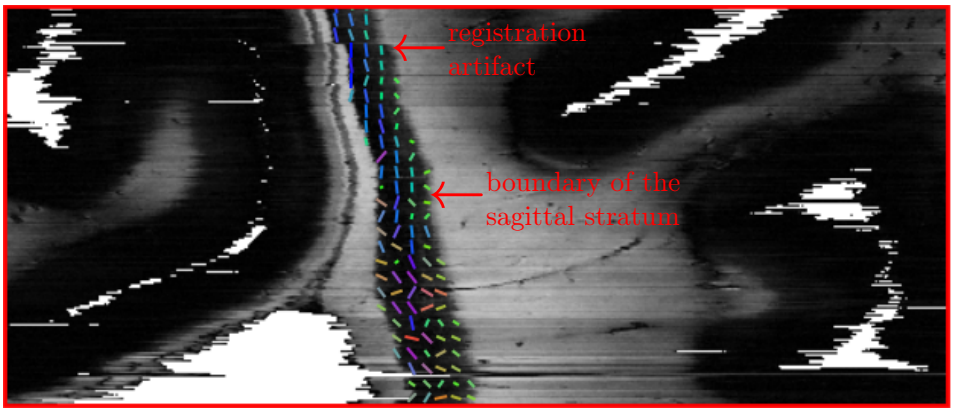

(c) Resliced view of (a) (red line) featuring the vector field of a fiber bundle inclined by approximately 90° (every 8th vector is plotted). The vectors in the upper part of the bundle fit to the outer boundaries, while vectors in the lower part seem randomly distributed.

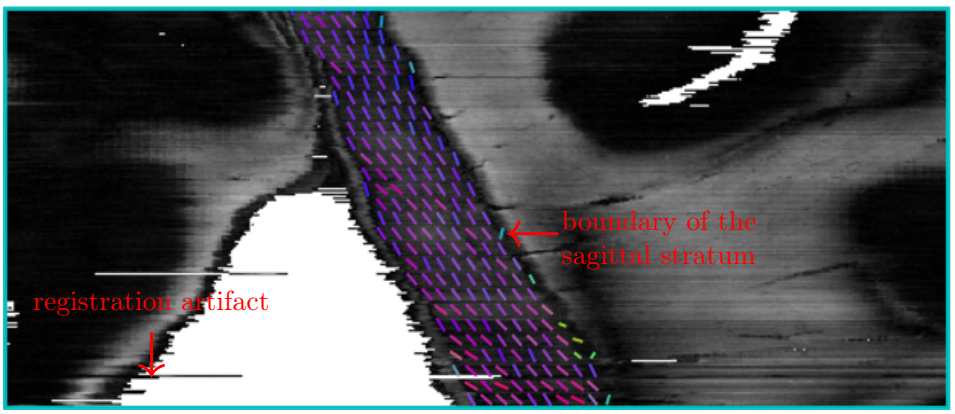

(d) Resliced view of (a) (cyan line) featuring the vector field of a fiber bundle inclined by approximately 60° (every 8th vector is plotted). The orientations fit very well with the outer boundaries.

FIGURE 4.8: Virtually resliced views of a stack of 220 consecutive sections to compare the reconstructed vectors with the anatomically visible course. The vector field has been masked manually based on the retardation values.

shown in Fig. 4.8d and Fig. 4.8c reduce a three-dimensional structure to two dimensions. Finally, this evaluation is only qualitative in its nature and does not provide a quantitative measure. Yet, it is currently the best way to validate the calculated vectors and with these limitations in mind, the presented data provides evidence that the fiber orientations indeed can be calculated from the measurements of a tilted sample.
The orientation of part of the sagittal stratum depicted in Fig. 4.8d was reconstructed very well and the vectors follow the structure which is inclined by approximately 60° with respect to the image plane. For the part of the sagittal stratum that is inclined by approximately 90° (cf. Fig. 4.8c), the calculated orientations are more diverse. Given the limitations of this analysis, it is possible that there are actually two different fiber constellations in the upper part of the sagittal stratum. It is also possible that the observed vectors are caused by a small systematic error, which leads to a significant misinterpretation. For simulated datasets, it was shown that the reconstruction of fibers with an inclination of $\alpha = 90°$ is particularly afflicted with random noise. Hence, the algorithm is also susceptible to minor systematic errors in the calculation, which would lead to a larger error in the derived orientation. The almost random orientations observed in the lower part of the sagittal stratum could be evidence for the random orientations that were predicted in the simulation for fibers inclined by $\alpha = 90°$.
To either confirm or deny any of these possibilities, the algorithm needs to be improved so that the instability at $\alpha = 90°$ is eliminated. This can only be achieved by using information that is not already included in the measured retardation values. So far, the measured direction angles of tilting measurements were neglected. In Sec. 4.4, a more advanced approach is developed, which takes both the amplitude and phase of the intensity signal for every position of the specimen stage into account. This new problem cannot be solved analytically any more and instead a maximum likelihood approach is employed. In order to differentiate the developed algorithm from the following approach, it is also referred to as the "DFT-based algorithm" as it calculates the inclination from a discrete Fourier transform of the retardance data.

4.4 Maximum Likelihood Estimation of the Birefringence Parameters from a Noise Model of the Data Acquisition Process

In the previous section, it has been shown that an analytical solution can be found for retrieving the inclination from a set of retardation data acquired at different positions of the tiltable specimen stage. In most cases, this approach yields deeper insights into the fiber architecture of the human brain and represents a significant improvement to the standard 3D-PLI analysis described in Sec. 2.3. An analysis of the noise stability in Sec. 4.3.2 revealed, however, that especially fibers with an inclination of $\alpha \approx \pi/2$ are prone to be afflicted with noise. Hence, an algorithm for the 3D-PLI analysis is needed, which takes all available data into account and also respects the noise sensitivity of individual data points.
The data is analyzed using the maximum likelihood method, which aims to determine the most probable parameters of a model given an observed dataset that is afflicted by measurement errors (i.e. noise). To this end, it is necessary to understand the influence of model parameters on the probability distribution of the measurands. Hence, in Sec. 4.4.1, the noise of the imaging system is examined and based on these observations, Sec. 4.4.2 gives a derivation of the statistical model of the data acquisition process. Once the probability of a certain observation for a given parameter can be described, an algorithm (cf. Sec. 4.4.3) is needed to find the maximal plausible parameter. For validation of the developed algorithm, the same datasets as in Sec. 4.3 are examined and the reconstruction of the underlying fiber architecture is compared to the previous results. Additionally, crossing fiber structures are analyzed, to gain a better understanding of how they influence the signal interpretation.

4.4.1 Noise Sensitivity of the LAP Imaging System

For the development of a likelihood based algorithm, a correct description of noise occurring in the imaging system is key. Hence, in this section, an examination of the detection noise is presented.

Methods

In order to analyze the noise level during image acquisition, a tissue sample was inserted into the LAP imaging system in order to create a broad variety of different intensity values. To generate a statistical database, $n = 100$ images of the same brain section were taken. This dataset was analyzed pixelwise for its sample mean

$$\bar{I} = \sum_{j=1}^{n} \frac{1}{n} I_j, \tag{4.18}$$

which estimates the expectation value $\mathrm{E}[I_j]$ and its sample variance

$$S^2 = \sum_{j=1}^{n} \frac{1}{n-1} (I_j - \bar{I})^2, \tag{4.19}$$

which estimates the variance $\mathrm{Var}[I_j]$ across the 100 images. The value I_j denotes the observed intensity value in each pixel and the index j specifies the jth-measurement.
Shot noise, which is typically the predominant source of noise in bright field imaging, is expected to follow a Poisson distribution driven by the statistics of photon detection [77]. For such a Poisson distribution, the standard deviation depends on the expectation value by $\sigma = \sqrt{\mathrm{E}[I_j]}$. To verify that the camera noise is indeed described by these statistics, the expectation value and variance were compared to those observed in the dataset. It can be shown that the expectation value of the variance estimator S^2 is given by

$$\mathrm{E}[S^2] = \mathrm{Var}[I_j] = \sigma^2, \tag{4.20}$$

and the variance of the sample variance can be calculated according to[8]

$$\mathrm{Var}(S^2) = \frac{2\sigma^4}{n-1}. \tag{4.21}$$

Results and Discussion

In the 2D-histogram in Fig. 4.9, the measured sample variances are plotted against the measured sample means. It can be seen that instead of the expected behavior of $\sigma = \sqrt{\mathrm{E}[I_i]}$ the noise actually follows a distribution whose standard deviation is given by $\sigma = \sqrt{3\mathrm{E}[I_i]}$. However, accepting the factor of three between the expected and observed results, the distribution follows the predicted behavior (this behavior being characterized by the linear increase and the respective variance bounds). Hence, in the following derivations the noise is described by the Poisson model but a gain factor of $g = 3$ needs to be taken into account. This gain factor is due to the internal signal processing steps in the camera. It most likely originates from the conversion of the electronic signal recorded by the camera chip into an RGB-image. RGB information is recorded by applying color filters on individual pixels on the camera chip in the so called *Bayern*-pattern. With this technique each camera pixel is only sensitive to one color. To generate the RGB information within an image pixel, demosaicing algorithms can by used to interpolate the missing color information [41]. These algorithms are designed by the manufacturer and not accessible to the public. Due to the factor of 3, which is equal to the number of color channels, it is possible that the gain factor originates from the processing steps of such an algorithm. Another possible reason might be a simple signal amplification in the camera electronics.
Now that the behavior of the camera noise is known, it can be utilized to describe the data acquisition in a probabilistic model.

4.4.2 Theoretical Model of the 3D-PLI Data Acquisition Process

As discussed in Sec. 4.2, tilting the sample corresponds to a rotation of the orientation vector $\mathbf{x}$, which is defined by an inclination α and a direction angle φ. The tilting can be expressed by a rotation according to

$$\mathbf{x}_i = \mathbf{R}_i \, \mathbf{x} \; . \tag{4.22}$$

After tilting the sample, we obtain a tilted vector $\mathbf{x}_i$ with an inclination α_i and a direction angle φ_i. In this calculus, the planar measurement is treated as any tilting

[8] Further details on the respective derivations can be found in [11, p. 331].

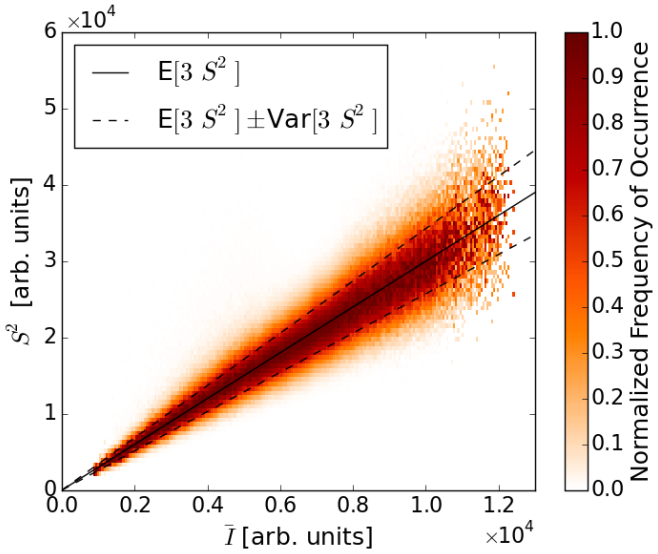

FIGURE 4.9: Normalized 2D-histogram of the camera detection statistics. The sample variance increases proportionally to the sample mean. Except for the factor of 3, the average increase as well as the distribution of the observed sample variance match with the theory.

measurement with a rotation matrix $\mathbf{R}_0 = I_{3\times3}$. For the following calculations, ideal polarization filters in the imaging system are presumed[9]. Hence, a 3D-PLI measurement of the tilted sample yields the intensity profile

$$I_{k,i} = \frac{I_0 e^{-\mu t}}{4}\left(1 + \sin\left(\frac{\pi}{2} t_{\text{rel}} \cos(\alpha_i)^2\right) \sin(2\rho_k - 2\varphi_i)\right),$$

as derived in Sec. 2.3. For this measurement the two normalized Fourier coefficients are defined

$$A_i = \frac{a_{1,i}}{a_{0,i}} = \frac{2}{N} \frac{1}{\frac{1}{N}\sum_k I_{k,i}} \sum_k I_{k,i} \cos(2\rho_k), \tag{4.23}$$

$$B_i = \frac{b_{1,i}}{a_{0,i}} = \frac{2}{N} \frac{1}{\frac{1}{N}\sum_k I_{k,i}} \sum_k I_{k,i} \sin(2\rho_k). \tag{4.24}$$

These measurands carry the relative amplitude (i.e. retardation) and phase (i.e. direction angle) information of the sinusoidal intensity profile. The normalization by $\frac{1}{N}\sum_k I_{k,i}$ ensures a value range of $A_i, B_i \in [-1, 1]$, thereby removing any influence of the transmittance on the measurands. The expectation values $\langle A_i \rangle$ and $\langle B_i \rangle$ of these measurands are then given by

$$\langle A_i \rangle = -\sin\left(\frac{\pi}{2} t_{\text{rel}} \cos(\alpha_i)^2\right) \sin(2\varphi_i), \tag{4.25}$$

$$\langle B_i \rangle = \quad \sin\left(\frac{\pi}{2} t_{\text{rel}} \cos(\alpha_i)^2\right) \cos(2\varphi_i). \tag{4.26}$$

For a given measurement, the measurands A_i and B_i are statistically distributed around their expectation values due to detection noise during image acquisition. Given a tilting

[9] In Sec. 4.4.7 the influence of non ideal polarization filters is discussed

position of the specimen stage defined by the rotation matrix $\mathbf{R}_i$ the likelihood to observe A_i and B_i can be defined as

$$P\left(A_i, B_i \,|\, t_{\mathrm{rel}}, \alpha, \varphi, \mathbf{R}_i\right) = P\left(A_i \,|\, t_{\mathrm{rel}}, \alpha, \varphi, \mathbf{R}_i\right) P\left(B_i \,|\, t_{\mathrm{rel}}, \alpha, \varphi, \mathbf{R}_i\right) \,, \tag{4.27}$$

for any parameter set $(t_{\mathrm{rel}}, \alpha, \varphi)$ that describes the fiber architecture of the brain tissue. According to Bayes' theorem[10], the probability to measure the acquired data for all different positions of the tiltable specimen stage can be defined by the cumulative density function

$$P\left(t_{\mathrm{rel}}, \alpha, \varphi \,|\mathrm{Measurements}\right) = \prod_{i=0}^{N_t} P\left(A_i \,|\, t_{\mathrm{rel}}, \alpha, \varphi, \mathbf{R}_i\right) P\left(B_i \,|\, t_{\mathrm{rel}}, \alpha, \varphi, \mathbf{R}_i\right) \,. \tag{4.28}$$

For the next step, a concrete expression for this probability needs to be derived, so that the most probable parameter set $(t_{\mathrm{rel}}, \alpha, \varphi)$ can be determined from the available measurement data.
When measuring an arbitrary intensity the observed value will be statistically distributed around $I_{k,i}$ due to shot noise. As investigated in Sec. 4.4.1 the shot noise is modelled by a Poisson distribution. Since the intensity values are large (i.e. $I_{k,i} \gg 10$), the photon detection can be modelled by a Gaussian distribution with mean $I_{k,i}$ and variance $\sigma_{I_{k,i}} = \sqrt{g I_{k,i}}$. Here, the gain factor g accounts for the conversion between the actual photon count of the camera and the gray value displayed in an image, which was observed in Sec. 4.4.1.
For any tilting measurement the measurand A_i is calculated from the intensities of the acquired images by Eq. (4.23). Using Gaussian error propagation, the standard deviation of A_i can be determined. With the partial derivative

$$\partial_{I_{k,i}} A_i \;=\; \frac{2}{N} \frac{\cos(2\rho_k) \frac{1}{N} \sum\limits_k I_{k,i} - \frac{1}{N} \sum\limits_k I_{k,i} \cos(2\rho_k)}{\left(\frac{1}{N} \sum\limits_k I_{k,i}\right)^2} = \frac{4}{N} \frac{\cos(2\rho_k) - \frac{1}{2} A_i}{I_{T,i}} \,, \tag{4.29}$$

the standard deviation of the measurand is given by[11]

$$\sigma_{A_i} \;=\; \sqrt{\sum_k \left(\partial_{I_{k,i}} A_i \; \sigma_{I_{k,i}}\right)^2} \;=\; \sqrt{\frac{4\,g}{N\,I_{T,i}} \left(1 - \frac{1}{2} A_i^2\right)}. \tag{4.30}$$

Similarly, the standard deviation of the second measurand can be calculated by

$$\sigma_{B_i} \;=\; \sqrt{\sum_k \left(\partial_{I_{k,i}} B_i \; \sigma_{I_{k,i}}\right)^2} \;=\; \sqrt{\frac{4\,g}{N\,I_{T,i}} \left(1 - \frac{1}{2} B_i^2\right)}. \tag{4.31}$$

[10] Bayes' theorem states that the probability P of an event X given a condition Y can be written as $P(X|Y) = P(X)P(Y|X)/P(Y)$. In our case this means that the probability that the brain tissue is correctly characterized by a parameter set $(t_{\mathrm{rel}}, \alpha, \varphi)$ for the given information acquired in the 3D-PLI measurement can be written as

$$P\left(t_{\mathrm{rel}}, \alpha, \varphi \,|\mathrm{Measurements}\right) = \frac{P(t_{\mathrm{rel}}, \alpha, \varphi) P(\mathrm{Measurements}|t_{\mathrm{rel}}, \alpha, \varphi)}{P(\mathrm{Measurements})}.$$

However, there is no inherent reason for any measurement or any parameter set to be more or less likely than any other. Hence, the prior as well as the normalization factor assume a uniform distribution and the equation can be simplified to

$$P\left(t_{\mathrm{rel}}, \alpha, \varphi \,|\mathrm{Measurements}\right) = P(\mathrm{Measurements}|t_{\mathrm{rel}}, \alpha, \varphi).$$

[11] A more detailed derivation is given in Appx. A.6

The theoretical transmittance for each tilting measurement $I_{0,i}$ in both equations is unknown. Thus, the measured transmittance is used as an estimator of this value. With the calculated expectation value $\langle A_i \rangle$ and the standard deviation σ_{A_i}, the Gaussian probability density function can be written as

$$P\left(A_i \,|\, t_{\mathrm{rel}}, \alpha, \varphi, \mathbf{R}_i\right) = \frac{1}{\sqrt{2\pi}\sigma_{A_i}} \exp\left(-\frac{\left(A_i - \langle A_i \rangle\right)^2}{2\sigma_{A_i}^2}\right), \tag{4.32}$$

Respectively we obtain the probability density function for the second measurand

$$P\left(B_i \,|\, t_{\mathrm{rel}}, \alpha, \varphi, \mathbf{R}_i\right) = \frac{1}{\sqrt{2\pi}\sigma_{B_i}} \exp\left(-\frac{\left(B_i - \langle B_i \rangle\right)^2}{2\sigma_{B_i}^2}\right). \tag{4.33}$$

The probability to obtain all of the measured data (i.e. the set of all A_i and B_i) is given by the product of these Gaussian density functions as described by Eq. (4.28). For optimization purposes it is common to calculate the logarithmic likelihood function, which is not as strongly peaked as the original likelihood function, so that the maximum can be found more easily. Additionally, most optimization algorithms are designed to find the minimum of a function rather than the maximum. Hence, a negative sign is added and the function that needs to be minimized is given by

$$\begin{aligned} -\log(P(t_{\mathrm{rel}}, \alpha, \varphi|\mathrm{Measurements})) = &\sum_{i=0}^{N_t} \log(\sigma_{A_i}) + \log(\sigma_{B_i}) + 2\sum_{i=0}^{N_t} \log(\sqrt{2\pi}) \\ &+ 0.5 \sum_{i=0}^{N_t} \left(\frac{\left(A_i - \langle A_i \rangle\right)}{\sigma_{A_i}}\right)^2 + \left(\frac{\left(B_i - \langle B_i \rangle\right)}{\sigma_{B_i}}\right)^2 . \end{aligned} \tag{4.34}$$

The term $2\sum_{i=0}^{N_t} \log(\sqrt{2\pi})$ of this equation can be neglected for the optimization process, since it represents a constant offset. In Fig. 4.10 this probability function is depicted for three different simulated measurements, each being parameterized by a set $(t_{\mathrm{rel}}, \alpha, \varphi)$. It can be seen that the function is not necessarily convex (thereby disabling convex optimization methods) and assumes very different shapes. Hence, a certain flexibility is required of the optimization algorithm which is supposed to find the minimum. In the next section, an optimization algorithm is discussed that is capable to minimize the function for all possible cases.

4.4.3 The Likelihood Orientation Estimation Algorithm

In order to create an algorithm that is capable of finding the maximum of the likelihood function (i.e. the minimum of Eq. (4.34) due to the negative sign), first the optimization problem is characterized. In Fig. 4.10 it can be seen that in general the likelihood function is not convex, thereby eliminating all algorithms which require a convex function. An analytical solution of the problem is not possible, since it would require calculating the gradient of Eq. (4.34) and determining its root analytically, but the trigonometric dependence of $\langle A_i \rangle$ and $\langle B_i \rangle$ on the parameters prevents such an approach.
The second important feature of the probability fields is the often long stretched iso-surfaces around the minimum (cf. Fig. 4.10a, Fig. 4.10c). Of particular interest is the field in Fig. 4.10a, whose contours resemble the Rosenbrock function. This function is known to be troublesome for gradient descent methods. Due to the shape of the long

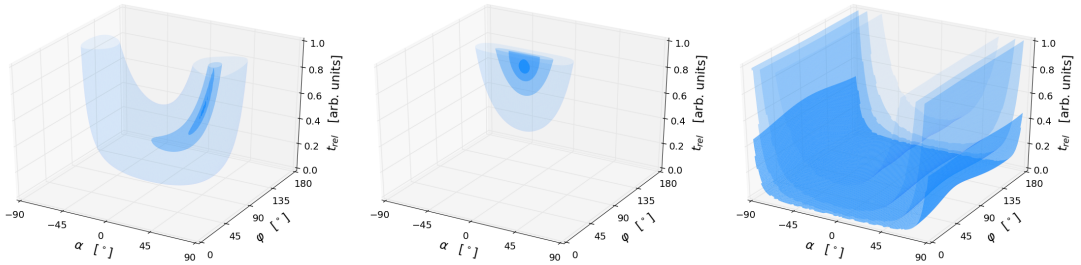

(a) $-\log(P)$ for $t_{\mathrm{rel}} = 0.65$, $\alpha = 45°$, $\varphi = 90°$

(b) $-\log(P)$ for $t_{\mathrm{rel}} = 0.9$, $\alpha = 0°$, $\varphi = 90°$

(c) $-\log(P)$ for $t_{\mathrm{rel}} = 0.01$, $\alpha = 0°$, $\varphi = 90°$

iso-surface values: -30 | 10^2 | 10^3 | 10^4

FIGURE 4.10: Iso-surfaces of the function $-\log(P(t_{\mathrm{rel}}, \alpha, \varphi|\text{Measurements}))$ for different simulated fiber structures.

stretched valley, the descent is often directed almost perpendicularly to the direction of the minimum. This results in a strongly oscillating pathway, while the algorithm searches for the minimum of the valley. Such a path can cause a high number of necessary iterations and sometimes even premature termination of the algorithm [65]. Hence, for the optimization problem posed here, the Nelder Mead simplex algorithm is chosen, which has been proven to be robust when tested with the Rosenbrock function [54]. This algorithm spans a simplex with four edges (given the three-dimensional parameter space). By iteratively comparing and moving these points through the parameter space, the simplex converges to the minimum of the sampled function.
In order to utilize the Nelder Mead simplex algorithm, two issues need to be solved. First of all, a suitable starting point needs to be determined. The planar measurement of the sample already provides a good estimate of the fiber direction angle φ_0, since it can be directly measured. For the initial values of t_{rel} and α an evenly spaced grid of 6×6 points is used to determine the best starting point using brute force minimization. From this starting point, the Nelder Mead simplex algorithm is used, which converges to the true minimum as depicted in Fig. 4.11.The second issue that needs to be overcome is the bounded parameter space (i.e. $-90° \leq \alpha \leq 90°$, $0° \leq \varphi \leq 180°$ and $t_{\mathrm{rel}} \geq 0$). The simplex algorithm has no inherent rules to deal with hard boundaries. A common way to deal with bounded optimization problems is accepting parameter values outside the boundaries but introducing a penalty term that forces the algorithm back into the original parameter space [45]. Such a method, however, requires multiple iterations (meaning a higher demand on computational resources) and can still lead to the algorithm getting stuck at the boundary. For the problem at hand, a more preferable way to deal with the boundaries is to symmetrize the parameter space. Considering a vector in spherical coordinates, this is achieved by allowing all values for the polar and azimuthal angles and then calculating the respective angles that describe the same orientation vector but are within the parameter space. Given the unbounded parameters $\tilde{\alpha}$ and $\tilde{\varphi}$, the symmetry is therefore described by

$$\alpha = \left[\tilde{\alpha} - \left\lfloor \left(\tilde{\alpha} + \frac{\pi}{2}\right)/\pi \right\rfloor \cdot \pi\right] \cdot \operatorname{sign}\left(-\lfloor \tilde{\varphi}/\pi \rfloor \mod 2 + \frac{1}{2}\right), \tag{4.35}$$

$$\varphi = \tilde{\varphi} - \lfloor \tilde{\varphi}/\pi \rfloor \cdot \pi. \tag{4.36}$$

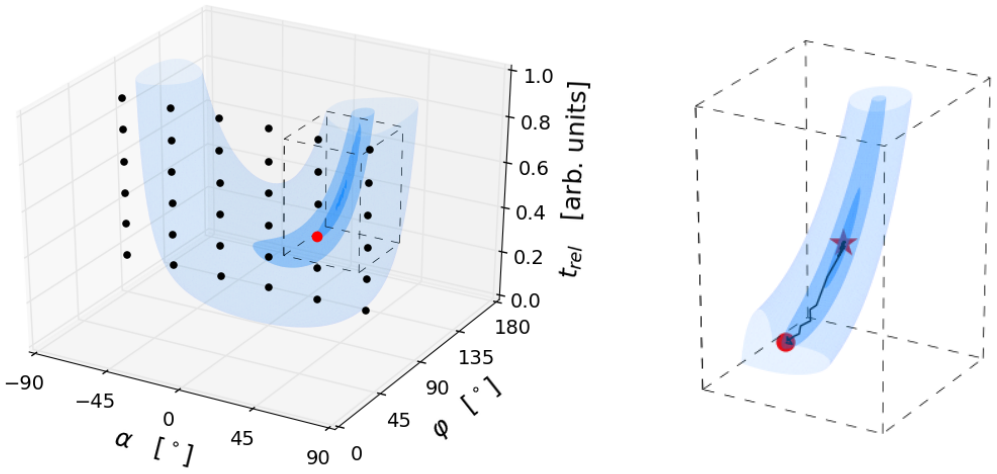

FIGURE 4.11: Visualization of the optimization algorithm. First a suitable starting point (indicated by the red dot) is chosen from a brute force grid (black dots). In a second step the Nelder Mead simplex converges to the minimum (indicated by the red star). The black line in the right figure shows the path the algorithm takes through the parameter space.

The subtraction (or addition) of multiples of π calculates the spherical coordinates of the vector within the desired parameter range. In Eq. (4.35) the sign of the inclination is changed if an uneven multiple of π is subtracted from the unbounded direction angle $\tilde{\varphi}$. This change of sign is necessary so that vectors that are antiparallel to vectors within the parameter boundaries are correctly represented by their counterparts.
For the relative thickness, it is sufficient to consider the absolute value of the unbounded parameter $\tilde{t}_{\mathrm{rel}}$ in calculations

$$t_{\mathrm{rel}} = \left|\tilde{t}_{\mathrm{rel}}\right| . \tag{4.37}$$

The described symmetry of the probability field is depicted in Fig. 4.12. The coloring of the α/φ-plane indicates which parameter values represent the same fiber orientation, while the gray plane indicates the symmetry of the parameter t_{rel} which leads to a mirroring of the probability field. Although there are multiple minima in the unbounded parameter space, each of them represents the same fiber model. Hence, for the optimization algorithm it is sufficient to converge to any of these minima. To summarize, the probability of a certain measurement to occur for any given parameter set is calculated by the function:

Function $-\log P\ (\tilde{\alpha}, \tilde{\varphi}, \tilde{t}_{\mathrm{rel}}, (A_0, B_0), \ldots, (A_{N_t}, B_{N_t}))$:
  symmetrize $\tilde{\alpha}$, $\tilde{\varphi}$ and $\tilde{t}_{\mathrm{rel}}$;
  determine α_i and φ_i $\forall i \in \{0, \ldots, N_t\}$;
  calculate $\langle A_i \rangle, \langle B_i \rangle$ $\forall i \in \{0, \ldots, N_t\}$;
  calculate $\sigma_{A_i}, \sigma_{B_i}$ $\forall i \in \{0, \ldots, N_t\}$;
return $-\sum_{i=0}^{N_t} \log(\sigma_{A_i}) + \log(\sigma_{B_i}) - 2\sum_{i=0}^{N_t} \log(\sqrt{2\pi}) - 0.5 \sum_{i=0}^{N_t} \left(\frac{(A_i - \langle A_i \rangle)}{\sigma_{A_i}}\right)^2 + \left(\frac{(B_i - \langle B_i \rangle)}{\sigma_{B_i}}\right)^2$

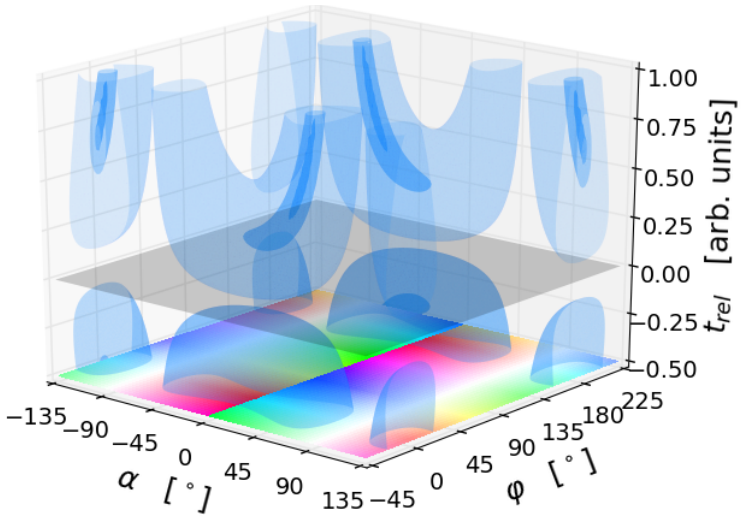

FIGURE 4.12: The symmetry of the probability field for values outside the defined parameter range. The coloring indicates orientation parameters that represent identical orientation vectors due to the periodicity of the spherical coordinates. For negative values of t_{rel} the value of the probability function is mirrored at $t_{\mathrm{rel}} = 0$ as indicated by the grey plane.

The optimization is then performed by:

Data: Maps of $\sin(\delta_i)$, φ_i, $I_{T,i}$ $\forall i \in \{0, 1, \ldots, N_t\}$
Result: Maps of α_0, ϕ_0, $t_{\mathrm{rel}0}$, $-logP_0$
initialization;
for *every image pixel* **do**
  $A_i = \sin(\delta_i)\cos(\varphi_i)$;
  $B_i = \sin(\delta_i)\sin(\varphi_i)$;
  for $\alpha^j, {t_{rel}}^j \in$ *Bruteforce-Grid* **do**
    $P^j = -\log P\ (\alpha^j, \varphi_0, {t_{\mathrm{rel}}}^j, (A_0, B_0, I_{T,0}), \ldots, (A_{N_t}, B_{N_t}, I_{T,N_t}))$;
  end
  determine initial α_m, $t_{\mathrm{rel}m}$ from the minimum of $\min(P^j)$;
  Nealder Mead simplex optimization of $-\log P$ with initial point ${\alpha^m}$, φ_0, ${t_{\mathrm{rel}}}^m$;
end

This algorithm will be referred to in the following as the *Likelihood Orientation Estimation* (*LOriE*) algorithm.
In this study, the LOriE algorithm was implemented prototypically, using the programming language *python*. For the numerical calculation the package *NumPy* and the implementation of the Nelder Mead simplex algorithm from the *SciPy* package were used [35]. Since the optimization needs to be carried out in every pixel of the image data, the necessary computation time was extensive. Together with two colleagues (Tim Huetz and Stefan Koehnen) a second piece of software was developed based on the prototypical software to parallelize the algorithm pixel wise and thereby enable the employment of high performance computing resources. In the current implementation between 60 and 90 core hours were needed to process a single brain section.

4.4.4 Simulative Examination of the Noise Stability

Methods

The LOriE algorithm is evaluated based on the same datasets as the DFT-based algorithm. Simulated datasets were created and analyzed as described previously in Sec. 4.3.2. That is, for a known fiber orientation vector the expected intensity profiles were created (one for each position of the tiltable specimen stage) and shot noise was added. After reconstructing the fiber orientation with the LOriE algorithm, the average angular deviation $\bar{\beta}$ between the original and reconstructed orientation was calculated.

Results

The average angular deviation for different initial fiber orientation vectors is depicted in Fig. 4.13. As before, each point on the sphere represents the corresponding initial fiber orientation vector and the coloring of the sphere visualizes the deviation $\bar{\beta}$.
The reconstruction of fiber orientations with the LOriE algorithm achieved a very high precision for the simulated white matter dataset (cf. Fig. 4.13a). For this scenario, most fiber orientations were reconstructed with an accuracy of $\bar{\beta} \approx 1.5°$. As in Sec. 4.3.2, a loss in accuracy for fibers with an inclination $\alpha = 0°$ or $|\alpha| = 90°$ was observed. In contrast to the reconstruction achieved with the DFT-based algorithm, the angular deviation accomplished by the LOriE algorithm did not exceed a value of $\bar{\beta} \approx 3°$.
For the scenario of a gray matter region (with $t_{\text{rel}} = 0.1$) the resulting accuracy of the LOriE algorithm is depicted in Fig. 4.13b. The angular deviation for most initial orientation vectors was around $\bar{\beta} \approx 5°$. Only for fiber inclinations of $|\alpha| = 80°$ to $|\alpha| = 90°$, the angular deviation increased to a value of $\bar{\beta} = 18°$. In this scenario, no significant loss in the reconstruction accuracy was observable for fibers with an inclination of $\alpha = 0°$.

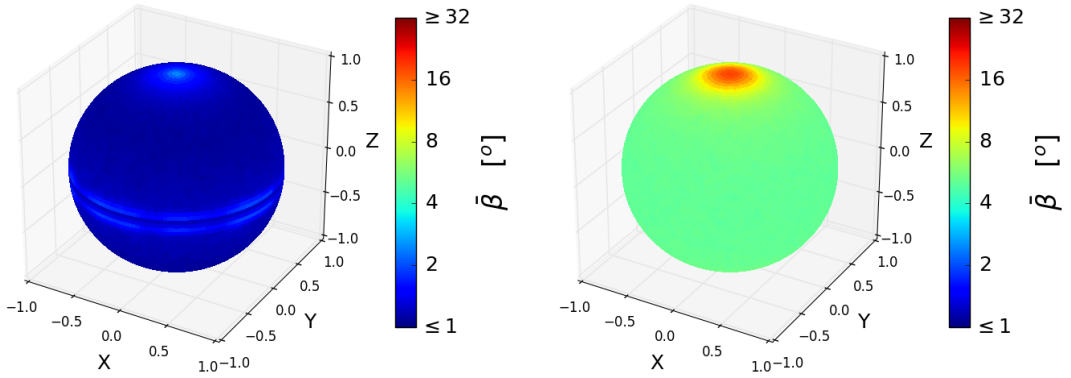

(a) $t_{\text{rel}} = 0.5$ (b) $t_{\text{rel}} = 0.1$

FIGURE 4.13: The spheres visualize how accurate any given orientation vector can be reconstructed by the LOriE algorithm for two different values of t_{rel}. Every point on the sphere encodes the accuracy $\bar{\beta}$ for the respective orientation vector.

Discussion

In both cases (i.e. the simulated white matter and the simulated gray matter region), the developed LOriE algorithm provided the same or better reconstruction accuracy as the first developed algorithm. In comparison with the previous results in Sec. 4.3.2, the error for the reconstruction of vectors with an initial inclination of $|\alpha| \in [10°, 80°]$ remained the same or slightly decreased (by not more than 2°). The true advantage of the LOriE algorithm is clearly visible for the reconstruction of white matter fiber bundles oriented out of the imaging plane. While the DFT-based approach in Sec. 4.3 is not capable of reconstructing these fiber orientations with any certainty, the LOriE based approach achieves a reconstruction accuracy of $\bar{\beta} \approx 3°$. Hence, for the LOriE algorithm, reconstruction of the fiber architecture in white brain matter is not significantly impeded by detection noise.
For the scenario of a gray matter region, the LOriE algorithm is capable of reconstructing the original orientation vector with good accuracy. For the reconstruction of steep fibers, shot noise is still an issue, though the effect is less pronounced than before. The recorded data does not provide enough information to distinguish between the different orientations in this scenario. Solving this issue would, therefore, require additional information from a different, unexploited modality.
Overall, the LOriE algorithm achieves an even better reconstruction of the fiber architecture by taking more information into account (i.e. not only the changes of the retardation value but also the change of the fiber direction is analyzed by the algorithm). This improvement comes at the cost of a strong increase in the required computational resources (the required time increases by a factor of $\approx 10^5$). Hence, researchers employing these techniques will have to evaluate whether the results justify the necessary effort on a case by case basis. This decision can only be based on evaluating experimental data and will depend on the structure that is examined.

4.4.5 Simulation of Crossing Fibers

In the previous section it was examined how accurate a fiber bundle with a single orientation is reconstructed. In biological tissue, however, fibers are often oriented more heterogeneously. Thus, it is of particular importance for the analysis of experimental datasets, how crossing fibers within a single volume element are interpreted by the algorithm. Such structures cannot be represented by a single vector and it is important to know how they manifest in measured datasets to avoid a misleading interpretation.

Methods

In order to obtain a basic understanding of how crossing fibers affect the results of the LOriE algorithm, two principle scenarios are analyzed. The first scenario consists of two fiber bundles oriented perpendicularly to each other with both bundles running within the image plane (cf. Fig. 4.14a). In the second scenario, one bundle still resides within the image plane, while the other bundle is oriented perpendicularly to the section (cf. Fig. 4.14b).
To simulate the first scenario (with both fiber bundles oriented in the section plane), the collective optical properties of the fibers within the considered volume element were represented by two Mueller matrices, one for each fiber orientation. The combined

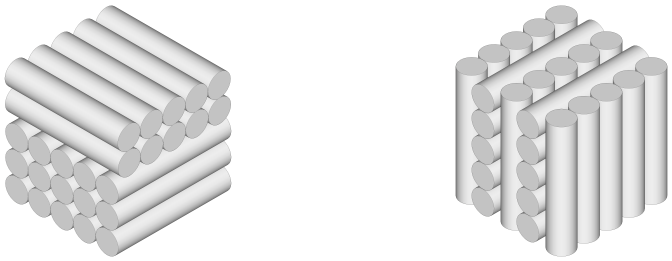

(a) Scenario of two crossed fiber bundles oriented parallel to the image plane.

(b) Scenario of fibers perpendicular to the image plane crossing in-plane fibers.

FIGURE 4.14: Visualization of crossing fiber scenarios. The signal is a mixture of all fibers within each cube.

thickness of the two bundles must be equal to the total sample thickness. Hence, a mixture parameter $q \in [0, 1]$ is introduced that describes the predominance of one fiber orientation over the other. Given the relative thickness $t_{\text{rel}} = 0.5$ for a sample that consists of a homogeneous fiber constellation, the relative thickness of each fiber bundle is then given by qt_{rel} and $(1 - q)t_{\text{rel}}$, respectively. With this information the Mueller matrix for each bundle was computed according to Eq. (2.18). Since transmitted light has to pass both bundles, the overall effect was obtained by multiplying the two matrices and considering the resulting matrix as the sample in the polarimeter[12]

$$\mathbf{M}_{tot} = \mathbf{M}_{fiber}\left(\mathbf{x}_1, qt_{\text{rel}}\right) \cdot \mathbf{M}_{fiber}\left(\mathbf{x}_2, (1-q)t_{\text{rel}}\right). \tag{4.38}$$

From this combined Mueller matrix the simulated signal was generated by Eq. (2.23)

$$I_k = \mathbf{S}^t_{\text{PSA},k}\ \mathbf{M}_{tot}\ \mathbf{S}_{\text{PSG},k}.$$

To simulate the tilting measurements, the two orientation vectors of the respective fiber bundles were rotated accordingly (cf. Sec. 4.3.2) and the steps of computing the Mueller matrices were repeated. The simulated signals were analyzed with the LOriE algorithm for different values of the mixture parameter q. The resulting orientation vector was compared to the two original orientations, by assessing the angular differences β_1 and β_2 (cf. Eq. (4.17)), which were computed according to Eq. (4.17).
Simulating the second fiber scenario (consisting of one fiber bundle within and one perpendicular to the section plane) requires a slightly different simulative approach. Light that is transmitted through the sample only passes one fiber bundle represented by the respective Mueller matrix. Hence, the intensity profile can be calculated as for a single fiber bundle. However, all light that passes the assessed voxel is measured within a single camera pixel and it is impossible to distinguish whether it passed fibers perpendicular to the image plane or fibers within the plane. Therefore, the overall intensity profile is given by simple signal averaging. Given $I_{k,\parallel}$ as the intensity profile for fibers oriented parallel to the image plane and $I_{k,\perp}$ as the intensity profile for fibers oriented perpendicularly to the image plane, the overall intensity was computed by

$$I_{tot} = qI_{k,\parallel} + (1-q)I_{k,\perp}. \tag{4.39}$$

The tilted measurements were simulated respectively. For the evaluation of this scenario, the angular differences $\beta_\parallel$ and $\beta_\perp$ were computed according to Eq. (4.17).

[12] Computing an overall matrix from a set of matrices, each representing a small part of the tissue is a common approach in simulative studies on 3D-PLI [19, 53].

Results

For two simulated fiber bundles running within the section plane and oriented perpendicularly to each other, the LOriE algorithm extracted the predominant fiber orientation and neglected the orientation of the other fiber bundle. This is visible in Fig. 4.15a where β_1 and β_2 are plotted depending on the mixture parameter. The plot shows that β_1 flips from 0° to 90° when the orientation $\mathbf{x}_2$ becomes predominant over $\mathbf{x}_1$ at $q = 0.5$; whereas β_2 behaves vice versa. Instead of significantly influencing the reconstruction of the orientation, the crossing fibers lead to a reduced signal strength. The relative thickness reconstructed by the algorithm decreases linearly from $t_{\text{rel}} = 0.5$ with an increasing amount of crossing fibers. For an even fiber mixture ($q = 0.5$), the relative thickness drops to $t_{\text{rel}} = 0$ and then rises back to its starting value with an increasing predominance of the second orientation.
The respective results for the scenario of a fiber bundle oriented parallel to the section plane crossing a bundle out of the section plane are shown in Fig. 4.15b. In this scenario, the orientation derived by the LOriE algorithm does not correspond to the orientation of the prevalent fiber bundle but almost always to the orientation of the bundle oriented parallel to the section. Only if the perpendicularly oriented fiber bundle makes up more than 97% of the tissue within the considered volume element, is its orientation recognized. The relative thickness decreases linearly with the mixture parameter q until it reaches a value of $t_{\text{rel}} \approx 0$ at $q \approx 0.97$. For fiber constellations with $q \geq 0.97$, it almost instantly returns to its original value of $t_{\text{rel}} = 0.5$.

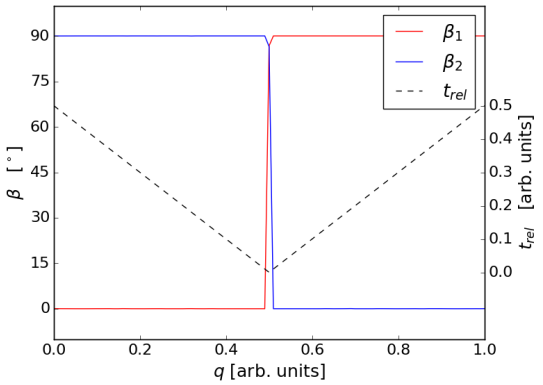

(a) In this scenario, the LOriE algorithm reconstructs the predominant orientation, while the value of t_{rel} decreases with increased mixing of the two orientations.

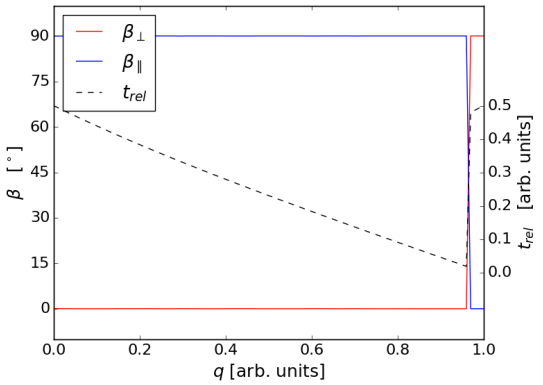

(b) In this scenario, the LOriE algorithm reconstructs the orientation parallel to the image plane preferentially. Only if the fiber bundle is almost free of differently oriented fibers, will the orientation perpendicular to the image plane be reconstructed.

FIGURE 4.15: Results of the simulation of crossing fiber structures. The plots depict the deviations of the computed orientation vector from the two original orientation vectors that describe the crossing structure (red and blue line) depending on the mixture percentage q of the two simulated fiber bundles. The computed structural parameter t_{rel} is also shown (dashed line). (a) features the results for the crossing scenario with both fiber bundles oriented parallel to the image plane, while in (b) the results for the scenario with one bundle perpendicular and one bundle parallel to the image plane are presented.

Discussion

For crossing fibers within the sectioning plane, the observed reconstruction is in agreement with theoretical predictions. The birefringence effect of the first fiber structure is opposed to that of the second one. Hence, the overall observed retardance is essentially the difference between the two individual values and the optical effect of the prevalent fiber orientation is observed. In this scenario, the derived relative thickness is reduced due to the opposing birefringence effects that cancel each other out. This behavior is useful when it comes to interpreting crossing fibers in experimental datasets. Since it is not possible to recover the structure of a heterogeneous fiber architecture within a single voxel using the current 3D-PLI model, recovering the predominant orientation is the next best alternative. For experimental datasets, the drop in the t_{rel}-parameter is helpful to identify crossed fiber bundles in deep white matter regions. Due to the linear dependence between the mixture q and the relative thickness t_{rel} it might even be possible to deduce the actual mixture within the pixel (e.g. as a 50%-50% or a 30%-70%). For a crossing structure with an even mixture of 50%-50% for each orientation, the algorithm will not be able to reconstruct a reliable orientation of any of the two fiber structures, since the birefringence of both bundles cancel each other out ($t_{\text{rel}} = 0$) and there is no signal left to interpret.
For most cases of crossed fiber structures with one bundle oriented within the plane and one perpendicular to the imaging plane, the LOriE algorithm reconstructs the orientation parallel to the section. This can be theoretically understood by remembering that fibers with an inclination of $|\alpha| = 90°$ display no retardation signal and only by tilting the sample and also considering the direction angle values in the LOriE algorithm can the original orientation be reconstructed. Thus, if there is even a small secondary signal introduced by a few fibers oriented parallel to the section, this signal will dominate the small signal of perpendicular fibers. It is only for structures which consist by more than 97% of fibers oriented perpendicularly to the brain section that this predominant fiber orientation is reconstructed. This knowledge about how crossing fiber structures are reconstructed is important for the interpretation of the results, since biological tissue almost always displays some level of heterogeneity.
In general we can conclude that a heterogeneous fiber architecture can impede the reconstruction of fiber pathways in a vector field based model. It was observed that even small "parasitic" fibers (i.e. fibers whose orientation deviates distinctly from that of the surrounding ones) can significantly influence the outcome of the LOriE algorithm. However, it was also shown that there are crossing structures for which the algorithm can be considered as stable, meaning that the prevalent orientation is reconstructed. For the two analyzed scenarios the resulting orientation vector always corresponds to one of the two intermingled orientations. This is a huge advantage compared to the common 3D-PLI reconstruction. For that reconstruction method, Dohmen et al. investigated simulated crossing fiber scenarios and found that the reconstructed orientation is almost always misinterpreted [19]. To understand every possible signal composition in the experiment, a more detailed survey of crossing fiber structures would be necessary. For now, the two analyzed compositions are sufficient to interpret the experimental results presented in the following section.

4.4.6 Validation of the LOriE Algorithm for Experimental Datasets

In Sec. 4.3.3, it has been observed that in an exemplary experimental dataset a fiber bundle oriented perpendicularly to the image plane was only partially reconstructed. Since the simulative analysis of the two developed algorithms revealed a distinct advantage of the LOriE algorithm for exactly this scenario, the reasons for the previously observed issues are investigated in this section. Additionally, the simulative study in Sec. 4.4.5 predicted the behavior of the LOriE algorithm for crossing fiber constellations, which is now investigated experimentally.

Methods

The LOriE algorithm was used to re-examine the dataset of 220 consecutive brain sections that was already presented in Sec. 4.3.3. For the interpretation of the resulting vector field, the parameter maps of the relative thickness and the transmittance were consulted.
To investigate crossing fibers, the optic chiasm of a hooded seal (Cystophora cristata) was chosen as an experimental model. In the optic chiasm, the optic tracts of the right and left hemisphere intersect each other and transition into the optic nerve. It is assumed that most of the fibers decussate from the one optic nerve to the contralateral optic tract. However, the percentage is highly dependant on the respective species [19]. The chiasm was cut in such a way that both optic tracts and optic nerves are oriented parallel to the section plane.

Results

First, the derived vector field of the virtually resliced stack of 220 sections of the right hemisphere is re-examined. The resulting vector fields of the LOriE algorithm are shown in Appx. B.1 in direct comparison with the results of the DFT-based algorithm introduced previously. In the direct comparison, small improvements are observable and the vectors extracted by the LOriE algorithm seem to fit even better with the course of the sagittal stratum that is visible in the retardation maps. This observation might, however, be subjective and is not quantifiable due to the qualitative nature of this comparison and the lack of a known ground truth. More importantly the reconstruction of the supposed perpendicular fiber bundle does not show major improvements. While parts of the bundle are reconstructed with an inclination of almost $\alpha = 90°$ to the right of these orientations there is still a region with fibers oriented in the y-direction.
In Fig. 4.16 the derived relative thickness and the measured transmittance are shown in a region of interest. It can be seen that the transmittance in Fig. 4.16a was constant across the whole bundle, while the relative thickness displayed two distinct levels. One of these levels coincided with the fibers oriented out of the section plane at $t_{\mathrm{rel}} \approx 0.35$ and the second level, which coincided with the fibers oriented along the y-axis, has a value of $t_{\mathrm{rel}} \approx 0.17$.
The optic chiasm of a hooded seal as a model for crossing fibers is shown in Fig. 4.17. The FOM in Fig. 4.17b displays the optic tracts and optic nerves with the crossing region in the center. It can be seen that the orientations in the crossing region consisted mostly of the two main orientations of the primary fiber tracts. Additionally, in a few pixels orientation vectors out of the section plane were reconstructed. The t_{rel}-map in

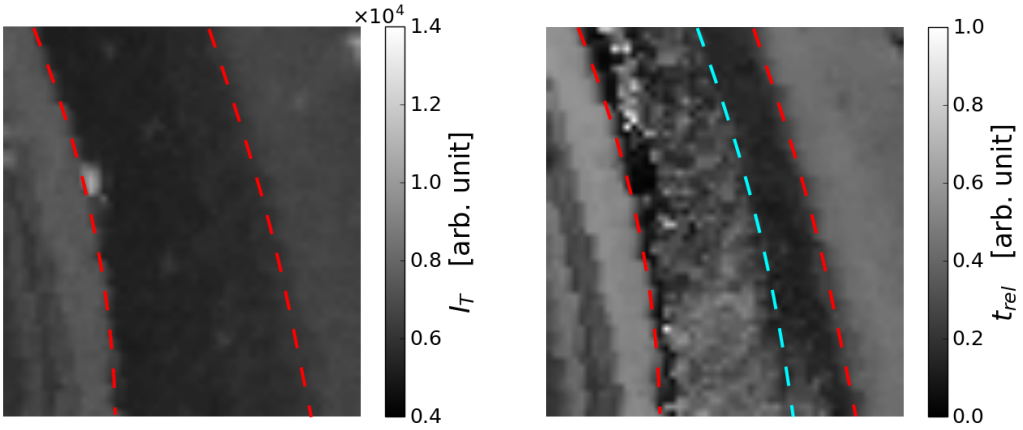

(a) The sagittal stratum is visible in the transmittance map. The red lines indicate the borders based on the measured values.

(b) In the t_{rel}-map a sub-division of the structure is visible (blue line). The left part has a high t_{rel} value, while the right part appears to have a significantly lower t_{rel} value.

FIGURE 4.16: Region of interest of the considered fiber bundle. While the light absorption caused by the myelin content is constant across the sagittal stratum (cf. (a)), the t_{rel}-map (cf. (b)) implies that the myelin density across the sagittal stratum is subdivided into two distinct regions. The discrepancy between the two maps indicates that a minority of crossing fibers is present.

Fig. 4.17c displays a constant value of $t_{\text{rel}} \approx 0.45$ for the individual fiber bundles which decreased down to $t_{\text{rel}} \approx 0$ in the crossing region. The probability map in Fig. 4.17d features the negative logarithmic probability that the LOriE algorithm achieved when it was finished with optimization. While this value was approximately $-\log(P) \approx -40$ for the homogeneous tracts, it increased up to $-\log(P) \approx 80$ in the crossing region.

4.4.7 Discussion

Reconstructing the vector field of the resliced stack with the LOriE algorithm provided results which are in agreement with the anticipated orientation indicated by the retardation maps. The vectors were reconstructed with the same or even slightly improved quality as for the first developed algorithm, thereby validating the working principle of the LOriE algorithm.
For the $\alpha = 90°$ scenario no major changes were observed in the reconstruction (cf. Appx. B.1). This result excludes the possibility that the orientations are afflicted with the known noise instability of the DFT-based algorithm, since simulative studies demonstrated that the LOriE algorithm would not be affected by this issue in deep white matter regions. The constant transmittance value across the fiber bundle indicates that there are no major changes in fiber density. A study by Reckfort et al. has shown that the attenuation of the transmittance is linked to the density of myelinated fibers in brain matter [63]. However, the t_{rel}-map generated by the LOriE algorithm, which is also indicative for fiber density, shows two distinct values for the two differently reconstructed orientations. It is known from the simulative investigation of crossing fibers in Sec. 4.4.5 that a minor in-plane fiber population dominates the signal over a major fiber population oriented out of the image plane. Hence, it is now evident that some fibers from the neighboring structure, which is also oriented along the y-axis, are interlaced with

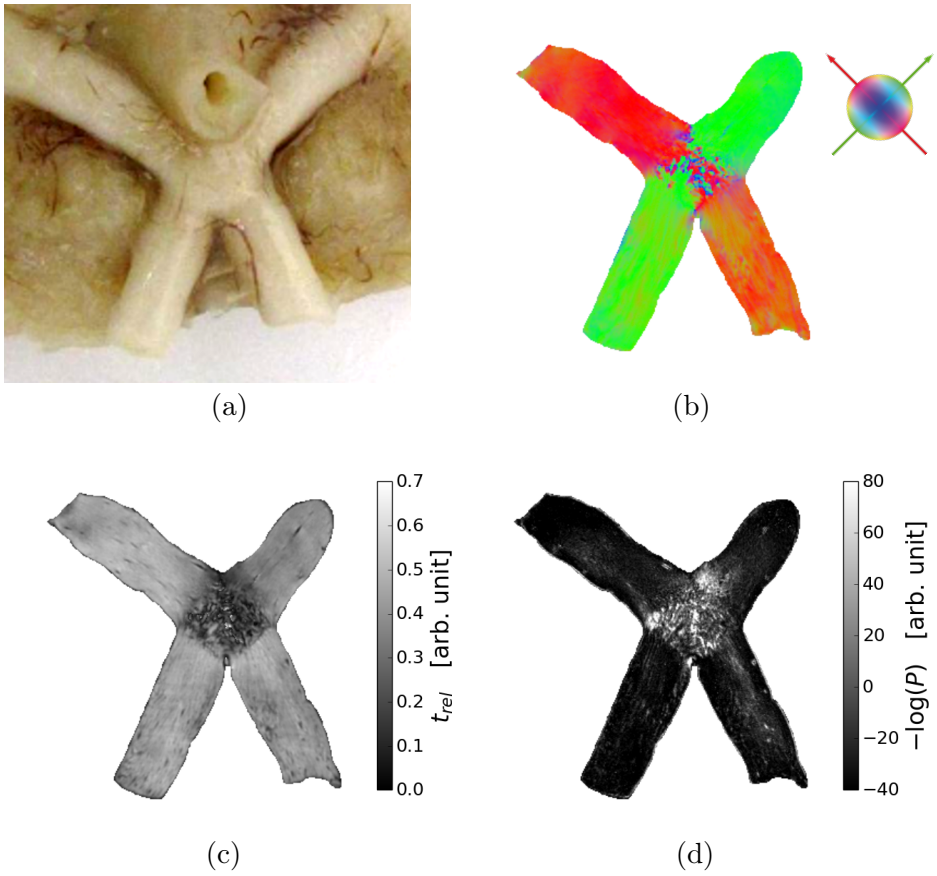

FIGURE 4.17: Shown are the different modalities generated by the LOriE algorithm for the optic chiasm of a hooded seal (displayed in (a) before sectioning). In the FOM (b) the extracted orientation in the crossing region is equal to one of the two primary orientations. In the t_{rel}-map (c) it can be seen that the value drops in the crossing region as expected. The optimized likelihood (d) highlights the crossing region due to bad agreement between the model and the experimentally observed data.

the examined bundle. As it was shown in simulations, these fibers dominated the signal causing the algorithm to reconstruct their orientation instead of the prevalent orientation along the z-axis.
To assess the results for in-plane crossing fibers, the optic chiasm of a hooded seal was analyzed as an experimental model. The results match with predictions of the simulative study, i.e. for most pixels either of the two main orientations was reconstructed and the relative thickness declines with an increasing fiber mixture. Additionally, it was observed that the probability of the deduced tissue parameters determined by the LOriE algorithm is lower in the crossing region. Generally, one would expect that this probability measure is poor whenever the measured data cannot be described well by the model. This can be due to a broad range of different reasons, such as outliers caused by dust particles. However, the changes in the signal when tilting a crossing fiber structure are not well defined by the employed model. Therefore, the algorithm cannot always fit the data to the model. In conclusion, this means that the LOriE algorithm provides another modality (i.e. the value $-\log(P)$ after optimization) that not exclusively but indicatively highlights regions of crossing fibers running within the section plane.
In a recent study, Reckfort et al. [63] were able to demonstrate a link between the transmittance and the parameter t_{rel}, thereby providing a different way to entangle inclination and relative thickness from a retardation measurement. The transmittance map of a brain section is dependent on brain preparation and changes of the transmittance over time have been observed in in-house studies. This method was applied with reasonable success to microscopic datasets, but it turned out to be less reliable for LAP datasets. While the exact quantitative relation between the observed transmittance and the relative thickness is not always evident, the transmittance can serve at least as an indicator. Here, this indicator was used as supplementary information for the interpretation of the fiber architecture in a region with crossing fibers. Due to the likelihood based estimation, this indicator could be used as a Bayesian prior to enhance the automatic analysis in the future. Such an approach would make it necessary to determine a probability distribution which specifies how likely it is to obtain a certain t_{rel}-value, given an observed value for the transmittance.
The developed LOriE algorithm is based on the description of the signal that presumes an ideal sample measuring polarimeter. However, in Chap. 3 it has been shown that non-ideal polarization filters lead to a more complex signal. Here, this was accounted for by deriving the retardation and transmittance values according to Eq. (3.13) and Eq. (3.12). This calibration leads to retardance values that fit to the developed theory, yet any effects on the standard deviation are not factored in. Since the expectation values comply with the theoretical model, the optimization will still find the correct minimum. However, by more carefully using all information of the experimental signal (i.e. it was shown that also 2nd order Fourier coefficients are to be expected, cf. Sec. 3.2) it might be possible to improve the analysis even further. Here, merely a proof of principle for the maximum likelihood estimation is presented, which has resulted in the elimination of the noise instability in the DFT-based algorithm. The LOriE algorithm has the major advantage that the likelihood based approach can be extended and adjusted by a suitable prior, thereby including additional information.

4.5 Conclusion

For the signal interpretation of 3D-PLI data, it is known that measured retardation values depend on the fiber inclination and the relative thickness of the birefringent tissue. This ambiguity has been a major challenge for the interpretation of 3D-PLI data. In this chapter, it was demonstrated how complementing the measured data with measurements of the tilted sample makes it possible to unravel this ambiguity. An algorithm was derived that is capable of analytically deriving the fiber inclination directly from the measured data. Both simulative and experimental evidence were presented to provide the proof of concept for the developed algorithm.
For fibers inclined by $\alpha = 90°$, a noise instability was observed in the simulative dataset. The instability in the data interpretation was successfully resolved by developing a second algorithm based on a maximum likelihood approach. While this second algorithm is theoretically needed to reconstruct fibers which are oriented perpendicularly to the brain section, in the studied experimental datasets only small improvements were visible. Due to the analytical solution in the DFT-based algorithm, the data of a single brain section can be processed within seconds, while the optimization process in the LOriE algorithm requires up to 60 core hours[13] per brain section, thereby creating the need for high performance computing. Thus, for future studies it will be necessary to assess whether the benefits in noise stability of the second algorithm outweigh the demands on computing resources.
Another issue when investigating fiber structures oriented perpendicularly to the brain section are crossing fibers. It has been observed that even small amounts of "parasitic" fibers can influence the tilting interpretation and lead to a misleading reconstruction. By a careful examination of all available data, however, the underlying crossing fiber architecture could be inferred manually. Thus, future studies should investigate whether it is possible to derive a fiber model that allows the structure of a heterogeneous fiber architecture to be analyzed and represented based on 3D-PLI measurements and tilted data.
To summarize, two new tools for the 3D-PLI data analysis have been developed in the context of this study and their performance was assessed for both simulative and experimental datasets. While the DFT-based algorithm is better suited for high throughput applications, the second algorithm focuses on accuracy over speed. It has been demonstrated how these tools can be employed to investigate the fiber architecture and how misinterpretation especially for crossing fiber structures can be avoided.

[13] *Core hour* is a unit to measure the computing time for parallelized computer programs. E.g. a task that runs on 8 CPU cores parallel for half an hour requires 4 core hours.

5

Developing an Oblique Illumination System for 3D-PLI Microscopy

5.1 Microscopic Techniques to Complement Planar 3D-PLI Measurements

A tiltable specimen stage makes it possible to add crucial information to the 3D-PLI data analysis and thereby enhances the reconstruction of fiber orientations in histological brain sections (cf. Chap. 4). It also provides structural information by computing the parameter t_{rel}, which is indicative for the fiber density. So far, the required data for the developed algorithms can only be acquired with the LAP imaging system. However, one of the advantages of 3D-PLI over other neuroimaging techniques is the possibility of a multiscale analysis of the fiber architecture. This is achieved by employing multiple imaging systems each designed for an analysis at a different resolution scale but relying on the same polarimetric measurement principle. To obtain this advantage, each 3D-PLI imaging system must offer the same data acquisition modes. While the tiltable specimen stage data acquisition is possible in the LAP, a similar technique has yet to be implemented for microscopic 3D-PLI.
This study aims to identify a suitable experimental setup and to provide a proof of principle for the technique. Furthermore, a guideline for the optical design of the imaging system is developed to construct a fully operational high throughput microscope with an oblique illumination. In a proof of principal experiment a prototype of the microscope is validated by employing the algorithms developed in the previous chapter.

Considerations Regarding a Tiltable Specimen Stage in a Microscopy Application

Pajdzik et al. have employed a tiltable specimen stage in a polarizing microscope to analyze the birefringence of crystals [58]. In their study it was demonstrated that the

The microscope was developed in collaboration with Philipp Schloemer and *Taorad GmbH*. Philipp Schloemer helped with implementing the experimental setup on the breadboard system as well as testing the camera and the light source. *Taorad GmbH* have provided comprehensive market research for the camera, light source and quarter-wave retarder and they seek to implement the developed setup in this study.

experimental setup makes it possible to enhance the interpretation of birefringent structures similar to the algorithms that were developed in Chap. 4. However, the analyzed crystals in their study had a homogeneous structure and considerations regarding image quality and resolution were irrelevant for their application. In 3D-PLI, on the other hand, image quality is critical. Tilting the specimen would result in a decreasing image resolution towards the edges of the image due to the limited depth of field of a microscope. To illustrate this in more detail the depth of field and the shift of the sample are calculated.
In the current setup of the polarizing microscope, the objective lens which essentially defines the resolution properties is specified for a magnification of $M = 5$ and a numerical aperture[1] of $\mathrm{NA}_{obj} = 0.15$. The lateral resolution, i.e. the minimal distance necessary to distinguish between two objects in the focus plane, is limited due to diffraction at the aperture of the objective lens. This diffraction causes a point object to be imaged as a so called Airy disc (the two dimensional version of the squared sinc-function). According to the Rayleigh criterion, it is possible to distinguish two imaged points as long as the central peak of the Airy disc is not closer than the first minimum of the next Airy disc [57]. Theoretically the minimal distance to be able to resolve two imaged points is calculated by

$$d_{xy} = \frac{0.61\lambda}{\mathrm{NA}_{obj}} \approx 2.2\,\mu\mathrm{m}, \tag{5.1}$$

with $\lambda = 550\,\mathrm{nm}$ being the peak wavelength of the illumination. Several criteria have been defined to describe the depth of field i.e. the ability to resolve points located out of the focus plane. Depending on the magnification M of the imaging system the depth of field is limited by diffraction described by wave optics or by the circle of confusion which can be derived from geometrical optics [38, 57]. A theoretical calculation of the total depth of field, which includes both effects is given by

$$d_{tot} = \frac{\lambda}{\mathrm{NA}_{obj}^2} + \frac{1}{M\ \mathrm{NA}_{obj}} d_{xy} \approx 27.4\,\mu\mathrm{m}, \tag{5.2}$$

where d_{tot} is the maximal allowed distance to the focus plane of the objective lens. Given a field of view of $3.3\,\mathrm{mm} \times 3.3\,\mathrm{mm}$, tilting the sample by an angle of $\tau = 8°$ leads to an offset of $\frac{3.3\,\mathrm{mm}}{2}\tan(\tau) \approx 0.23\,\mathrm{mm}$ at the edges of the image. By comparing this value with the depth of field it becomes obvious, that tilting the sample in a microscopic imaging system is not feasible for the purpose of 3D-PLI.

Polarized Conoscopy and Polarized Light field Imaging

Historically, polarized light microscopy for crystal analysis has been practised in two different observation modes, the orthoscopic and conoscopic view. In orthoscopy the specimen is imaged directly, while in conoscopy every image point corresponds to a ray that passed through the specimen at a different angle. Thereby, the conoscopic view simultaneously reveals information similar to that gathered by tilting the specimen stage into different directions. The maximal tilting angle that can be analyzed in the

[1] The numerical aperture (NA) of a lens is a common concept in optics which describes the ability to collect light within an acceptance angle θ. It can be calculated from the clear aperture of the lens (D) and the focal length f by $\mathrm{NA} = sin(\theta) = \sin\left(\arctan\left(\frac{D}{2f}\right)\right)$.

conoscopic view depends on the numerical aperture of the objective lens which allows oblique rays to pass only if the angle between the ray and the optic axis is less than

$$\tau_{max} = \arctan(\mathrm{NA}_{obj}). \tag{5.3}$$

Similar to the tiltable specimen stage setup developed by Pajdzik et al., a conoscopic inspection suffers from the same restriction; it is limited to a homogeneous sample.
Oldenbourg et al. have demonstrated that polarized light field imaging offers the possibility to combine the orthoscopic and the conoscopic view, and thereby generate a dataset that offers both spacial and angular resolution of the sample at the same time [56]. The principle of this imaging technique is based on inserting a microlens array at the position of the sensor in a common microscope, while the sensor is moved to the back focal plane of the lens array (Oldenbourg et al. introduced an additional relay lens behind the microlens array as it allowed more flexibility in the construction). The number of micro lenses in the array is decisive for the spacial resolution, while the angular resolution is determined by the number of sensor pixels assigned to each micro lens[2].
In their study, Oldenbourg et al. have imaged a calcite film that consisted of multiple calcite crystals. Their setup employed a micro lens array consisting of 120×120 lenses and the conoscopic view of each individual lens was imaged by an array of 12×12 sensor pixels. Thereby it was possible to determine the inclination angle of each individual crystal by assessing the respective conoscopic views.
The light field technology would in principle be feasible for 3D-PLI imaging; yet two experimental constraints need to be discussed. In the optical design of a light field microscope there is an inherent trade-off between the angular and spacial sampling rate as the number of pixels on a camera sensor is limited. In contrast to a tiltable specimen stage experiment, it is not possible to manually select the oblique rays. Instead, the oblique rays are sampled at an approximately equidistant rate up to the maximum oblique angle τ_{max}. These two properties of a light field microscope have severe implications on the data storage requirements of 3D-PLI. In the current version of the PM the planar measurement of a single human brain section generates approximately 0.7 TB worth of data. Since a loss in the spacial resolution is not acceptable, a higher magnification would be required and the amount of data would increase linearly with the number of pixels per micro lens. The most significant information for the purpose of the data analysis presented in Chap. 4 is generated for large tilting angles. Thus, the equidistant angular sampling in a light field microscope would generate a large amount of redundant information, which could be used to maximize the SNR in the tilting analysis but is not necessary to obtain good results. Therefore, it is more desirable to individually select the oblique rays and only record the necessary information, which can be realized with an oblique illumination. While light field imaging generally benefits from simultaneously recording all data for real time applications, oblique illumination techniques offer more control but are only suited for stationary samples (such as the histological brain sections in 3D-PLI).

Oblique Illumination Techniques

Several studies have investigated different experimental setups to generate oblique illumination for a multitude of applications in the field of microscopy. Instead of illuminating

[2] A more comprehensive explanation of the working principles of light field microscopy has been presented by Levoy et al. [50]

the sample with a broad range of oblique rays and then differentiating them within the imaging optics (as is done in polarized light field microscopy), the basic idea is to select the rays as desired in the illumination system. In this way compromises with regards to image quality can be mostly avoided.
Levoy et al. have developed one of the most comprehensive imaging systems to control and record the light field [49]. They employed a custom build epi illumination system that is capable of shaping both spacial and angular features of the illumination beam, by projecting light from a digital light processor onto a micro lens array. Additionally a micro lens array in front of the camera sensor made it possible to record the light field behind the specimen plane. While their system facilitated the study of the reflection and scattering characteristics of a sample extensively, adapting the system for the purpose of 3D-PLI microscopy would require to overthrow almost every single aspect of the construction principle and redesign the system. Hence, for simply achieving oblique illumination in 3D-PLI microscopy other design principles are considered.
An oblique illumination system for polarized microscopy has been developed by Shribak and Oldenbourg based on liquid crystal technology [70]. In their study, the illumination cone was partially masked in the aperture plane of the condenser lens by an aperture scanning device. This device consisted of a set of three liquid crystal modulators which enable the control of polarization states. Each of the modulators was subdivided into 8 pie-shaped sectors. Thereby it was possible to mask out e.g. three quarters of the aperture and the central ray of the created illumination cone was oblique relative to the optic axis of the imaging system. It was demonstrated that this oblique illumination made it possible to determine the orientations of birefringent microtubules of an aster, a biological structure that is formed during mitosis. This technique achieved a similar purpose as desired for the 3D-PLI analysis and shows that oblique illumination might be used to enable the analysis presented in Chap. 4 for microscopic datasets. However, the device does not offer a very precise control of the incidence angle of the light. Additionally the rays around the central ray of the illuminating cone will not be evenly distributed, as the shape of the aperture is changed from a circular shape to a circle segment.
A well known technique for creating oblique illumination is achieved by slightly shifting the aperture at the stop of the condenser lens in a Koehler illumination[3] system [37]. This technique has been used by microscopists for almost a century, in order to achieve a higher contrast in images. Kawata et al. developed an oblique illumination system based on this technique for the purpose of optical tomography [39, 40]. In their system the aperture was placed off-axis and then rotated around the optic axis of the imaging system. Thereby slightly different views of the specimen were created and by computationally reversing the optical setup, these views were utilized to reconstruct the original three dimensional structure of the imaged object. While their application was very different from the one desired for 3D-PLI, their oblique illumination system allowed them precise control through the well defined offset of the pupil.
As the current version of the PM already employs a Koehler illumination to ensure a uniform background, adapting this approach for 3D-PLI seems the most promising way forward. In the following section the detailed working mechanisms of this design will be analyzed and a proof of principle setup will be presented.

[3]Further details on the working principle of the Koehler illumination are presented in Sec. 5.4.1.

5.2 Basics of Geometrical Optics

A fundamental understanding of optical principles is most important when developing an oblique illumination system. Hence, this section covers a review of the basics of optics that are used for designing a suitable optical setup. These basics do not cover a comprehensive introduction to optics but they build the foundation for theoretical considerations regarding the optical design of the oblique Koehler illumination. Furthermore, the most common lens shapes are introduced and a few principle guidelines on how to choose the correct lens for a certain application are presented. Based on these concepts, the following section (cf. Sec. 5.3) presents a simulation approach based on ray optics that is used throughout this study to simulate the optical train and to gain a better understanding on how to optimize the illumination system.
The basic concept of geometrical optics is to describe light as rays, which represent the direction of propagation and can also be characterized as the normals to the wave fronts in the description of light as an electromagnetic wave. This theoretical description does not account for diffraction and interference effects.
Image formation in geometrical optics is based on Snell's law, which describes the change in direction of a light ray at a surface between two optic media. Given the refractive indices of the two media n_1 and n_2 this change in direction is described by

$$n_1 \sin(\theta_1) = n_2 \sin(\theta_2), \tag{5.4}$$

with θ_1 and θ_2 being the respective angles between the rays and the surface normal [38, p. 23]. Consequently, it is possible to design a curved surface (i.e. the surface of a lens), which is capable of refracting rays which diverge from a single object point so that they converge in a second point - the image of the object point. The most basic shape of a lens is defined by two spherical surfaces defined by the spherical radii R_1 and R_2. As there are multiple radii combinations for such a spherical lens which yield nearly the same optical properties, lenses are rather defined by their focal length. The focal length of a lens is the distance in which collimated rays are focused into a single point. It can be computed from the lensmaker's equation

$$\frac{1}{f} = (n-1)\left(\frac{1}{R_1} - \frac{1}{R_2} + \frac{(n-1)\mathrm{CT}}{nR_1R_2}\right), \tag{5.5}$$

where n denotes the refractive index of the lens material and CT the thickness in the center of the lens [38, p. 26]. The focal length can be either positive, indicating the capability to focus a divergent beam, or negative, in which case it has a divergent effect on a light beam. If the thickness of the lens is negligible compared to its focal length, image formation can be easily expressed through the thin lens approximation. For a thin lens with focal length f, the distance of the object d_o and distance of the image d_i to the lens are interrelated by the formula

$$\frac{1}{f} = \frac{1}{d_o} + \frac{1}{d_i}. \tag{5.6}$$

For a given distance of the object to the lens, the magnification (i.e. the size of the image h_i relative to the size of the original object h_o) can be calculated by

$$\frac{h_i}{h_o} = \frac{d_i}{d_o}. \tag{5.7}$$

The ratio d_i/d_o is also called conjugate ratio and it is said to be infinite if either the object or the image are at infinity.
For a thick lens, for which the thin lens approximation does not apply, different types of aberrations occur. Spherical aberrations, describe the phenomenon that parallel rays which are refracted at the outer parts of the lens are focused to a different point than those which are closer to the optic axis. This effect is more prominent the wider the diameter of a lens is relative to its curvature. In the image this usually leads to a slight blurring. This issue can be resolved for example by replacing a single lens with multiple ones, thereby reducing the refractive angle at the different surfaces (cf. Kasunic et al. for more details [38, pp. 72-77]).
Chromatic aberrations are caused by the wavelength dependency of the refractive index, meaning that the focal length of a lens actually varies with the wavelength of the incident light. While this poses a problem for many imaging applications, for the purpose of this study it is irrelevant as the bandwidth of the illumination is limited to a few nanometers.
Off-axis aberrations such as coma - a point like object is imaged like a comet tail - occur especially in telescopes when the viewed object is not in the center of the image but rather in the periphery of the view. While off-axis aberrations are particularly relevant for telescopes, all optical systems with an infinite conjugate ratio need to consider them.
Minimizing aberrations in an optical system is very complex and the form of a spherical lens can have a huge impact. Hence, it is useful to define the Coddington shape factor

$$q = \frac{R_1 + R_2}{R_1 - R_2}, \tag{5.8}$$

which makes it possible to describe the form of a positive lens. Lenses with a shape factor of $q = \pm 1$ are called *plano-convex*, lenses with $|q| < 1$ are called *bi-convex* lenses and lenses with a shape factor of $|q| > 1$ are called *meniscus* lenses. It can be shown that a lens with a refractive index of $n \approx 1.5$ displays minimal spherical and coma aberrations for a shape factor of $q \approx 0.8$ [38, p. 82]. Such a lens is also called *best form* lens. As best form lenses require more effort in the manufacturing cycle they are often replaced by plano-convex lenses with $q = 1$, which display similar properties.
In contrast to spherical lenses, *aspheres* are a group of lenses, whose surface is conic. These surfaces make it possible to specifically address different types of aberrations and sometimes even eliminate them completely. The aspherical surface is generally being parameterized by

$$z(r) = \frac{r^2}{R\left(1 + \sqrt{1 - (1+\kappa)\frac{r^2}{R^2}}\right)} + \sum_j \epsilon_j r^{2j}, \tag{5.9}$$

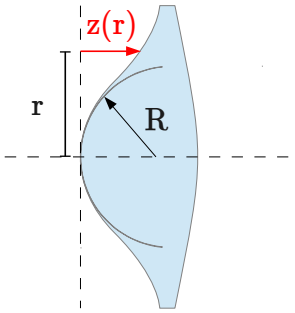

FIGURE 5.1: Illustration of an aspherical lens whose surface is defined by a function $z(r)$.

Lens Type	**Conjugate Ratio**	**Application Purpose**
Plano-Convex	5× - Infinite	Focusing a Collimated Beam, Collimating a Point Source
Bi-Convex	0.2× - 5×	Relay Imaging (Real Object and Image), Focusing a Divergent Beam
Best Form	Infinite	Focusing a Collimated Beam, Collimating a Point Source
Aspheric Condensers	Infinite	Light Collection, Collimation of Incoherent Light
Aspheric Collimators	Infinite	Optimized On-Axis Performance, Laser Diode Collimation, Fiber Coupling
Aspheric Lens Pairs	1× - 3.66×	Optimized On-Axis Performance, Relay Imaging (Real Object and Image)

TABLE 5.1: Commercially available lenses from *Thorlabs* and their designated application purpose according to the manufacturer.

where R is the radius of the surface, r is the distance to the optic axis and κ the conic constant (cf. Fig. 5.1). Depending on the conic constant the surface can assume different conic shapes:

- hyperbolic for $\kappa < -1$
- parabolic for $\kappa = -1$
- elliptic for $\kappa > -1$ and $\kappa \neq 0$
- spheric for $\kappa = 0$

Additionally, the polynomial term $\sum_j \epsilon_j r^{2j}$ makes it possible to include further corrections that cannot be accomplished by a purely conical shape. Only polynomials with even exponents are considered for surface corrections to ensure that lenses retain their axial symmetry. By adjusting the aspheric coefficients in a rigorous ray tracing optimization the performance of a lens can be improved even further for a specific application.
When developing an optic system, ideally the surfaces of each lens are adjusted to their specific purpose in the optic train and address relevant aberrations. For the development of the prototype of the illumination in this study, this is however not feasible due to the extensive costs of manufacturing single custom lenses. Hence, suitable lenses have to be chosen from a commercially available range of products. According to the manufacturer *Thorlabs* their different lenses are each optimized for a specific purpose [32], so that some aberrations can be minimized by choosing the most suited lens shapes. In Tab. 5.1 the most relevant lenses for this study are listed as well as their designated application purpose which is primarily defined by the conjugate ratio.
Assessing the performance of a lens is commonly based on calculations and ray tracing simulations. The most basic approach to analyze the ray propagation along the optical train is offered by the *paraxial approximation*, which assumes that the angle θ between a ray and the optic axis of the system is sufficiently small for approximating trigonometric functions by

$$\sin(\theta) = \tan(\theta) = \theta. \tag{5.10}$$

This approximation makes it possible to define any ray by its distance to the optic axis and its angle relative to the optic axis. Hence, a ray can be represented by a 2-D vector $(x, \theta)^\dagger$. Calculating the transition of the ray at one plane along the optic axis to another is achieved by a *ray transfer matrix* so that

$$\begin{pmatrix} x_2 \\ \theta_2 \end{pmatrix} = \begin{pmatrix} A & B \\ C & D \end{pmatrix} \begin{pmatrix} x_1 \\ \theta_1 \end{pmatrix}. \tag{5.11}$$

Examples for such a ray transfer matrix are [24]

- $\begin{pmatrix} 1 & d \\ 0 & 1 \end{pmatrix}$ when the ray propagates a distance d in free space,
- $\begin{pmatrix} 1 & 0 \\ \frac{n_2 - n_1}{R n_1} & \frac{n_2}{n_1} \end{pmatrix}$ when the ray is refracted at a curved surface with radius R between two optic media with refractive indices n_1 and n_2.

As the ray transfer matrix analysis depends on the paraxial approximation, it is susceptible to errors when larger angles occur. To avoid this fallacy, simulations in this study are instead based on Snell's law in vector form, which makes it possible to accurately refract rays at any surface. Given the original direction of propagation of a ray (represented by the vector $\hat{\mathbf{l}_1}$) and the local surface normal of a refractive surface ($\hat{\mathbf{n}}$) the new direction of propagation is calculated by

$$\hat{\mathbf{l}}_2 = \frac{n_1}{n_2}\hat{\mathbf{l}}_1 + \left(-\frac{n_1}{n_2}\hat{\mathbf{n}} \cdot \hat{\mathbf{l}}_1 - \sqrt{1 - \frac{n_1^2}{n_2^2}\left(1 - (\hat{\mathbf{n}} \cdot \hat{\mathbf{l}}_1)^2\right)} \right) \hat{\mathbf{n}}, \tag{5.12}$$

with n_1 and n_2 as the refractive indices of the respective optical media [26, p. 140]. Based on this equation a simulation toolkit was developed in the context of this thesis which is presented in Sec. 5.3.

5.3 Simulating the Optical Train

Open source software for simulation in optics is scarce and commercially available software is very expensive and often lacks key features needed for this study (such as off-axis placement of elements). Hence, a custom simulation toolkit was developed to examine the path of light through the optical train. All figures in this chapter that display parts of the optical train were created with this toolkit.
The simulation presented here has been limited to a two dimensional representation, as most optical effects can be understood based on such a 2D-model due to the rotational symmetry of optic elements. The toolkit has been implemented in python and utilizes the *NumPy* and *SciPy* packages for mathematical calculations and the *Matplotlib* package for visualization [35].
The structure of the simulation is depicted in Fig. 5.2 as an UML-diagram. The core of the simulation toolkit is the `Manager` class which has two public methods to register light sources and objects ("`add_source`" and "`add_object`").
In the context of this simulation a light source is a collection of light rays. It is represented by the `ABC_source` class[4] which has to provide a method "`init_rays`" to initiate

[4] An *abstract base class (ABC)* in python is a class that can enforce derived classes to implement certain methods (which are defined as abstract methods in the ABC) that are required so it provides the features needed by another class (in this case the `Manager` class).

the rays relative to the position of this particular source.
The `Ray` class has a list of segments (points in 2D-space) which when connected track the light path of the represented light ray. The orientation of a ray is always the direction of propagation from the last segment as the next segment has yet to be determined. A ray can be terminated which means that it will no longer propagate through the optical train.
The derived class `Directed_source` initiates rays all at the same origin with their orientations being distributed according to an angular distribution function. Every ray is initiated at a quantile of the cumulative distribution function whereas the ray for the 50%-quantile usually coincides with the primary orientation of the directed light source. In this study two source models have been used which each represent a model for the angular irradiance characteristic of a commercially available diffuser. The first model is a uniform model which initializes the rays in equidistant steps around the primary orientation of the source within a given opening angle. The second model is used to represent a Gaussian shaped angular irradiance characteristic.
This directed source class was used to model the light sources in this study. In principle, however, the concept of the simulation makes it possible to implement broad range of source models by subclassing `ABC_source` implementing the respective source model when initiating the rays.
An object represented by the `ABC_Object` class has attributes that define its positioning and size. The method `propagate_ray` specifies how the object modifies a ray and the method `draw` defines how the object is visualized on the canvas. Objects are further subdivided into two classes. Those which can be represented by a planar surface (that is to say a line in 2D-space) are derived from the class `ABC_plane_surf` and all others are derived from `ABC_curved_surf`. The primary function of this subdivision is to provide suitable methods to calculate the impact point of a ray with the surface. This is straight forward for a planar surface (one simply needs to calculate the intersection of two lines). For a curved surface, the intersection with a "front" and a "back" plane is calculated, which constitute the boundaries for the object. This initial information is used to compute the actual collision point of a ray with the more complex surface.
The planar surfaces implemented for this study were absorbers which absorb (that is to say terminate) all rays upon impact, apertures which only allow rays within the inner radius to pass, and thin lenses which are able to refract rays as governed by Eq. (5.6) and Eq. (5.7). Curved surfaces are used in this study for the sole purpose of modelling the different lens shapes. A refracting surface (represented by the class `ABC_refracting_surf`) defines a surface function $z(r)$ which calculates the distance relative to a plane surface (analogue to the definition of an aspherical surface, cf. Fig. 5.1). For a spherical surface this function is given by

$$z(r) = R - \sqrt{R^2 - r^2} \tag{5.13}$$

with R as the radius of the spherical surface. For aspherical surfaces the function is given by Eq. (5.9). Once the surface function is defined, the impact point of a ray on the surface can be determined by a root finding algorithm (Brent's method was used which is readily implemented in the SciPy package [35]). At this location the surface normal is calculated and the vector form of Snell's law Eq. (5.12) is employed to determine the new orientation of the ray. The refractive index N-BK7 glass assumed in this calculation was $n_{N-BK7} = 1.5195$ at a wavelength of $\lambda = 532\,\mathrm{nm}$ according to Polyanskiy et al. [61].
Upon starting the routine "`simulate`" of the `Manager` class, it iterates over all rays of all sources and passes them through the optical train. The objects are passed sequentially

in the order they were registered to the `Manager`, which means that registration of the objects must correspond to the alignment of the components. Finally calling the "`draw`" routine visualizes the scene on the canvas.
The simulation toolkit has been used for the simulative assessment of optical components and for all illustrations of the light path in this chapter.

5.4 Designing an Oblique Koehler Illumination

The Koehler illumination is frequently used in microscopes due to its homogeneity, as well as the possibility to control spot size and numerical aperture. The optic principles and basic setup of the Koehler illumination are described in this section, followed by a discussion on how to introduce modifications to achieve oblique illumination. In a third step, the individual components are analyzed for their properties and inherent trade-offs and an optical design for an oblique illumination system for 3D-PLI microscopy is proposed.

5.4.1 The Standard Koehler Illumination

Along the optical path of a microscope there are two distinct sets of so called "conjugate" focal planes, which occur alternatingly along the optical train. Planes of each set are superimposed in the image formation and an object placed in one of these planes will be visible in all consecutive focal planes of the considered set. The first set can be observed in the "normal mode" (also referred to as orthoscopic mode) of the microscope. Commonly only the specimen plane is visible in this set; however, if needed a scale can be placed in a conjugated plane to superimpose with the image of the specimen, making it possible to measure the length of certain features.
Optical filters on the other hand are often afflicted with dust particles, finger prints or other defects which would result in image artifacts if these were placed in the normal conjugate set. Thus, optical filters are commonly placed in a plane reciprocal to the specimen plane, which is completely out of focus in the normal observation mode. This other conjugate set, which is reciprocal to the first, can be observed by using an eyepiece telescope instead of ocular. As the rear aperture of the objective lens is in focus, this mode is also referred to as "aperture mode" (or alternatively "conoscopic mode"). The reciprocal nature of the two sets can be expressed through a two dimensional Fourier transformation which transforms the spacial domain into an angular spectrum [30, p. 1.75]. Knowledge of the interrelation between the two conjugate sets is very useful when trying to manipulate the optical setup to accommodate custom features.
In his essay from 1893, August Koehler formulated the three basic properties that are required of an illumination system in optical microscopy [44]. He stated that

- the numerical aperture of the illumination needs to be adaptable to fit the numerical aperture of the current objective lens.
- the size of the illuminated spot should match the field of view in the microscope to avoid reflections and minimize light exposure of the specimen.
- the illumination conditions need to be the same for every spot of image point.

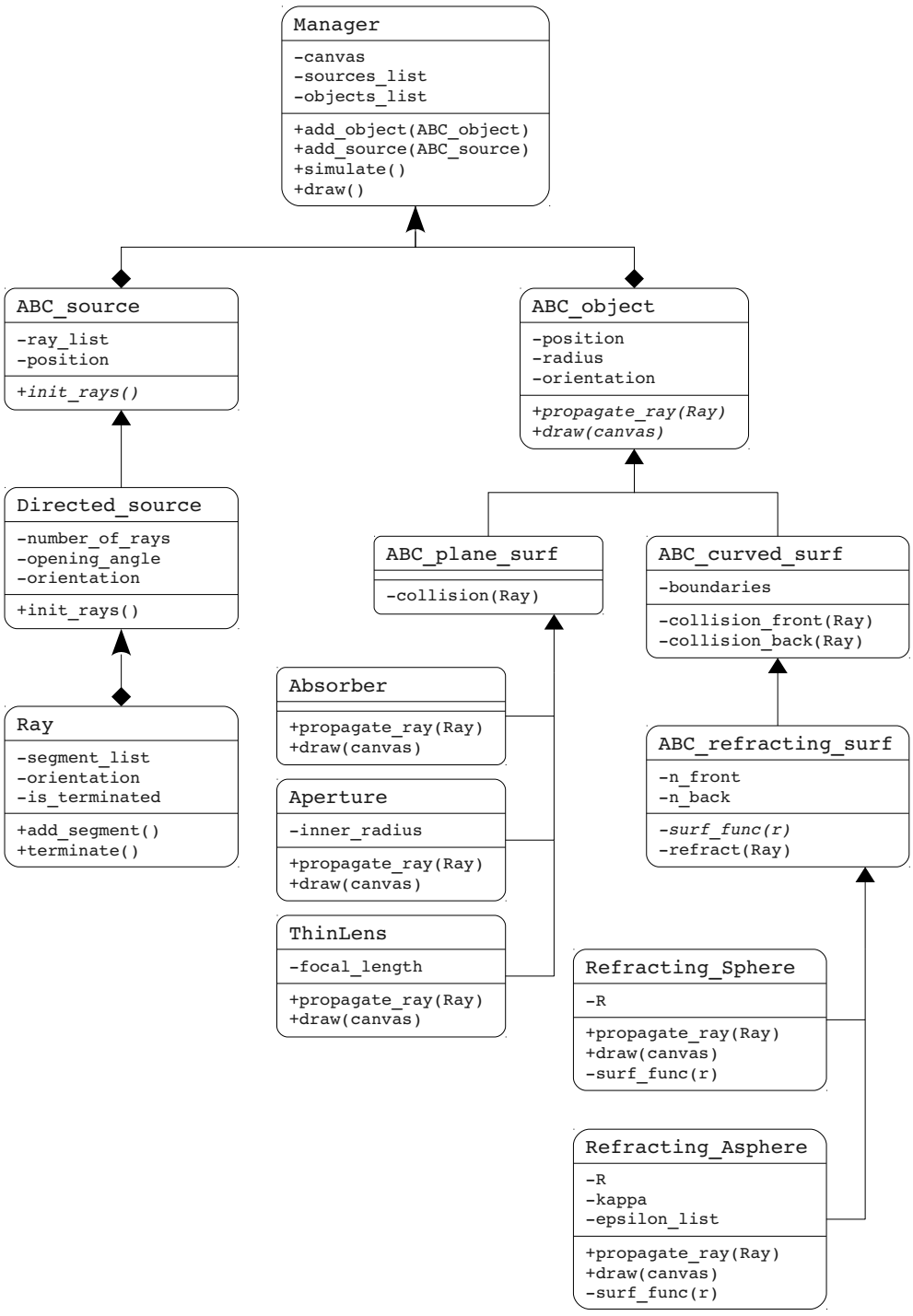

FIGURE 5.2: UML diagram of the developed simulation framework for geometrical optics.

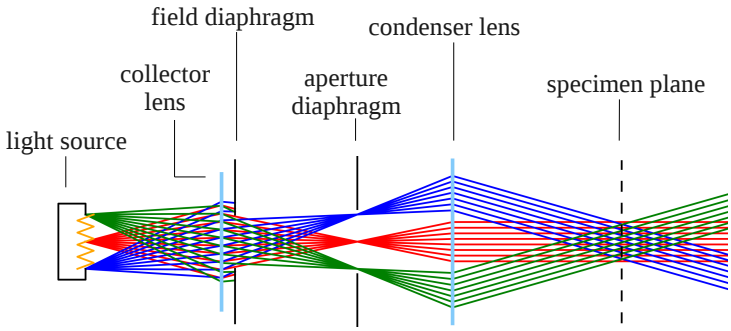

FIGURE 5.3: Standard optical setup of the Koehler illumination in the thin lens approximation. The light path of rays irradiated from three distinct points of the light source is visualized (red, green and blue rays).

These conditions are met in the so called Koehler illumination which utilizes the concept of conjugated planes. By placing the light source in a plane of the aperture set, every point is completely out of focus in the image plane, thereby creating a very even illumination. A diaphragm placed in the aperture set makes it possible to adjust the numerical aperture of the illumination while a diaphragm placed in a preceding conjugated plane of the specimen makes it possible to adjust the size of the illumination spot. In the standard optical setup of the Koehler illumination an image of the light source is created with a collector lens as depicted in Fig. 5.3. The optical elements of the illumination system are arranged in such a way that the image created by the collector lens is in the focal plane of the condenser lens. Hence every point of the light source is mapped onto the whole field of view and an uneven irradiance of the light source will be homogenized in the image.
A field diaphragm is placed right after the collector lens. The image of this field stop is created by the condenser lens in the focal plane of the objective lens, thereby enabling the control of the illumination spot size. The aperture diaphragm on the other hand is placed in the plane of the image of the light source making it possible to control the numerical aperture of the system.

5.4.2 Realizing an Oblique Illumination

In the Koehler illumination the numerical aperture usually is selected to match that of the objective lens. However, if the numerical aperture is reduced, it is possible to realize oblique illumination by displacing the aperture stop off-axis. This concept is depicted in Fig. 5.4 where it can be seen that the specimen is now illuminated at an angle τ. By centering the aperture diaphragm and widening its diameter the imaging system works like a standard polarizing microscope. This poses an advantage over other oblique illumination systems as one can convert the system to a standard already established for 3D-PLI at any time.
Realizing this oblique illumination has implications that need to be considered. While most of the Koehler illumination works as before, the numerical aperture is significantly reduced in order to select individual angular segments of the illumination cone. The lateral resolution of a microscope depends on the numerical aperture of both the illumi-

nation system (NA_{illu}) and the objective lens (NA_{obj}) and is calculated by[5]

$$d_{xy} = \frac{1.22\lambda}{\mathrm{NA}_{obj} + \mathrm{NA}_{illu}}. \tag{5.14}$$

Considering the limit of a pinhole aperture diaphragm ($\mathrm{NA}_{illu} = 0$) and neglecting other diffraction effects, this design of an oblique illumination results in a maximal loss of lateral resolution by a factor of 2. This trade off seems to be acceptable when compared to the loss of pixel resolution in a light field microscope, yet it is still a trade-off that needs to be kept in mind.
As the aperture stop is moved to different positions, thereby creating different angles for the oblique illumination, it also selects different parts of the light source image. Given an inhomogeneous light source this means, that different oblique angles may have different background intensity levels, while the field of view is still illuminated in a homogeneous manner. To avoid having very different intensities for different oblique angles, therefore it is desirable to employ a light source that is as homogeneous as possible to begin with. If quantitative comparability between intensity values is necessary, this issue can be compensated for by an intensity calibration (i.e. scaling the observed intensity values with suitable calibration factors).

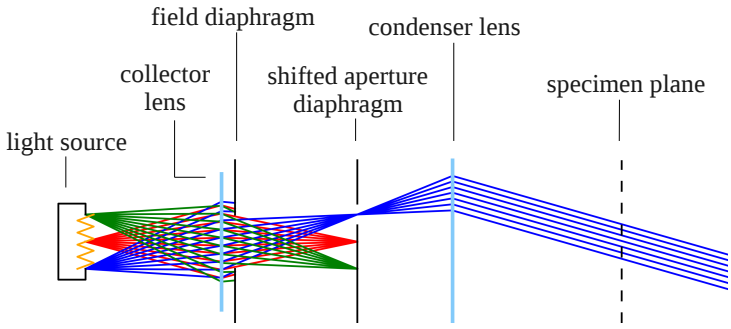

FIGURE 5.4: Schematic of an oblique Koehler illumination setup. By reducing the diameter of the aperture diaphragm and shifting it off-center an oblique illumination is accomplished.

5.4.3 Engineering and Optimization of the Optical Design

When designing the optical setup of the polarizing microscope a comprehensive assessment of the individual components is necessary to achieve the best illumination properties for 3D-PLI microscopy. In this section the different optical elements and their influence on the illumination is analyzed with the simulation toolkit presented in Sec. 5.3. To study the different components experimentally, a prototype of the optical train was built on a breadboard system from *Thorlabs, Inc.*

[5] In Eq. (5.1) it was presumed that both numerical apertures were identical in order to simplify the formula.

Principle Alignment of the Optical Components

In the Koehler illumination the position of several optical elements is predefined by the positions of the conjugated planes (cf. Sec. 5.4.1). By approximating the optics as thin lenses the spacing between optical elements can be described mathematically. Essentially there are three degrees of freedom - the focal length of the collector and condenser lens (f_{coll} and f_{cond}) and the distance between light source and condenser d^o_{coll}. The position of the aperture diaphragm is given by the position of the image of the light source created by the collector lens. This distance can be calculated by

$$d^i_{coll} = \left(\frac{1}{f_{coll}} - \frac{1}{d^o_{coll}} \right)^{-1}. \tag{5.15}$$

If h^o_{coll} is the diameter of the light source, the size of the generated image is given by

$$h^i_{coll} = h^o_{coll} \, \frac{d^i_{coll}}{d^o_{coll}}. \tag{5.16}$$

As the image of the light source has to be in the focal plane of the condenser lens, the distance between the condenser lens and the aperture diaphragm is predetermined by the focal length f_{cond}. The field diaphragm is positioned closely (i.e. at a distance Δ) behind the collector lens to control the size of the illumination spot. As the sample has to be placed in its conjugate plane, the sample position can be calculated by determining the position at which the image of the field diaphragm is created by the condenser lens by

$$d^i_{cond} = \left(\frac{1}{f_{cond}} - \frac{1}{d^o_{cond}} \right)^{-1}. \tag{5.17}$$

Knowing the position of the different components now enables us to compute the size of the illuminated spot h^i_{cond} in the sample plane depending on the diameter of the field diaphragm h^o_{cond}. This spot size can be calculated by

$$h^i_{cond} \;=\; h^o_{cond} \frac{d^i_{cond}}{d^o_{cond}}, \tag{5.18}$$

whereas the position of the field diaphragm relative to the condenser lens is given by

$$d^o_{cond} = d^i_{coll} + f_{cond} - \Delta. \tag{5.19}$$

To give a better overview, the respective positions of the different optical elements are depicted in Fig. 5.5. The length of the complete illumination system is therefore given by

$$l_{illu} = d^o_{coll} + d^i_{coll} + f_{cond} + d^i_{cond}. \tag{5.20}$$

As a constructional requirement this length was kept below 300 mm, in order to avoid an oversized system. The comprehensive description of these distances in the Koehler system makes it possible to simulate the illumination in the thin lens approximation and also provides a good indication for the placement of components in the experimental setup.

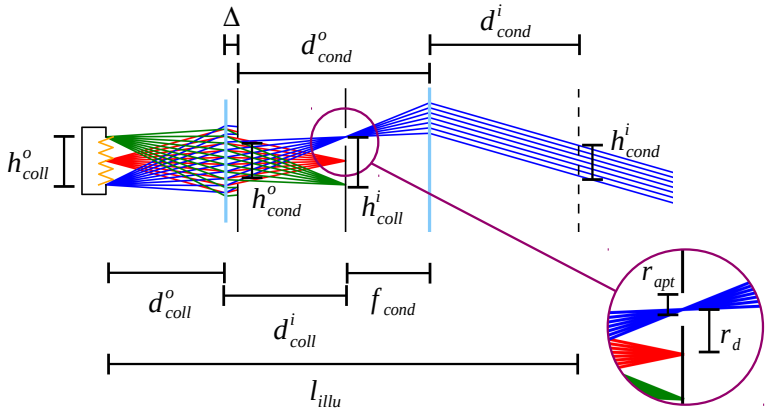

FIGURE 5.5: The designated distances in the oblique Koehler illumination setup.

The Imaging System

Starting with the imaging part of the microscope, the camera (*SVS-vistek* evo 4070 MFLGEC) has been chosen for its capability of fast image acquisition at a high resolution. The sensor consists of an array of 2048 × 2048 pixels and has a size of 15.2 mm × 15.2 mm. For the optical imaging components an objective lens (*Nikon* Plan Apo 4× 0.2NA) and an according tube lens (*Nikon* CFI60) were acquired. The objective lens has been chosen for its high numerical aperture[6] of $\mathrm{NA}_{obj} = 0.2$, which is particularly important for this application, as it not only limits the resolution and depth of field but also the possibility to capture oblique rays. Given the size of the sensor and the magnification factor of the objective lens of $M = 4\times$ the field of view is 3.8 mm × 3.8 mm wide. Hence, the requirements for the illumination system are to create a suitable spot size diameter to illuminate the complete field of view (i.e. $h^i_{cond} \geq 3.8\,\mathrm{mm}\sqrt{2}$) and the capability to exploit the numerical aperture to the full extent (i.e. maximize the oblique angle between the rays and the optic axis which is theoretically limited by $\tau \leq \arcsin(\mathrm{NA}_{obj})$). The polarization filters in the imaging path are placed between objective and tube lens reciprocal to the imaging plane. The employed quarter-wave retarder (*Newport* 10RP34-532) was chosen for its large clear aperture of 17.8 mm while at the same time having a high retardation accuracy of $\pm\lambda/350$. A large clear aperture of the filter is important as it is placed in the imaging path of the microscope and can therefore place a limit on the numerical aperture in addition to the objective lens. A linear polarizer (*Thorlabs* LPVISE100-A) with an extinction ratio of $> 5000 : 1$ was placed at an angle of 45° relative to the retarder, thereby forming a circular analyzer.

The Light Source

For the light source, output power is critical to enable short exposure times and thereby facilitate rapid measurements. Hence, an ultra high powered LED source (*Prizmatix* UHP-Mic-LED-520) is employed, which delivers collimated light with an optical output power of > 900 mW at a central peak wavelength of 520 nm and a spectral bandwidth

[6]While this numerical aperture is not high in general, it is high at 4× magnification. Employing a lens with a higher magnification would also yield a higher numerical aperture with the possibility to increase the oblique angle but also dramatically increase the data storage requirements.

of 36 nm (full width half maximum). High quality quarter-wave retarders are not commercially available at this particular wavelength. Hence, a bandpass filter (*Thorlabs* FL532-10) is employed to shift the central peak to the more common wavelength of 532 nm with a bandwidth of 10 nm (full width half maximum).
The Koehler illumination in general is not designed for a collimated light source. In fact, due to the reciprocal nature between the angular and spacial distribution in the two conjugated plane sets, it is important that the light source has a homogeneous angular distribution which transforms into a homogeneous spacial illumination in the specimen plane. Hence, it is necessary to employ a diffuser to create a divergent light source.
To analyze the influence of this relationship in more detail, a standard Koehler illumination was simulated. In the illumination setup the lenses were modelled as thin lenses to avoid an overlay with effects caused by lens aberrations. The source was modelled by 1000 individual directed point sources each emitting 1000 rays. The directed point sources emit rays according to a uniform angular spectrum with a bandwidth of $\pm 10°$ for the first and a Gaussian shaped angular spectrum with a bandwidth of $\pm 7.5°$ for the second simulation scenario. The two angular spectra are modelled to emulate the experimentally measured angular distributions of two considered diffusers (*Thorlabs* ED1-C20 and *Thorlabs* DG10-600) as provided by the manufacturer (cf. Appx. B.2).
In Fig. 5.6 it can be seen, how the angular distribution of the light source and the illumination uniformity in the specimen plane are interrelated. For a Gaussian shaped angular spectrum of the diffuser (which emulates a standard ground glass diffuser) the intensity profile in the specimen plane follows also a (clipped) Gaussian distribution (cf. Fig. 5.6b and Fig. 5.6c). To avoid this issue, a windowed uniform diffuser (*Thorlabs* ED1-C20) is employed which in contrast to standard issue diffusers scatters the light to a windowed uniform distribution across the different angles. The simulation shows that for such a uniform diffuser the background illumination in the specimen plane is also uniform (cf. Fig. 5.6b and Fig. 5.6c). According to the manufacturer this engineered diffuser consists of microlens units, whose surface profiles and positions are individually specified to achieve the desired beam shaping. By introducing a certain level of randomization, the properties of the diffuser are made impervious to different illumination conditions.
For all following considerations regarding the alignment of components in the Koehler setup, the surface of this diffuser constitutes the origin of the light source, rather than the LED itself.

The Collector and Condenser Lens

So far, the principle of the Koehler illumination has only been discussed on the basis of the thin lens approximation. This is usually sufficient for applications where only a homogeneous illumination is required. However, in our case a much higher level of control over the illumination beam is required which comes at the cost of being more sensitive to perturbations. Hence, determining suitable lens shapes for the collector and condenser lens is important.
The collector lens creates an image of the light source. The optimal conjugate ratio depends on two factors:

- For a conjugate ratio of approximately 1 the length of the illumination system (cf. Eq. (5.20)) is minimal.

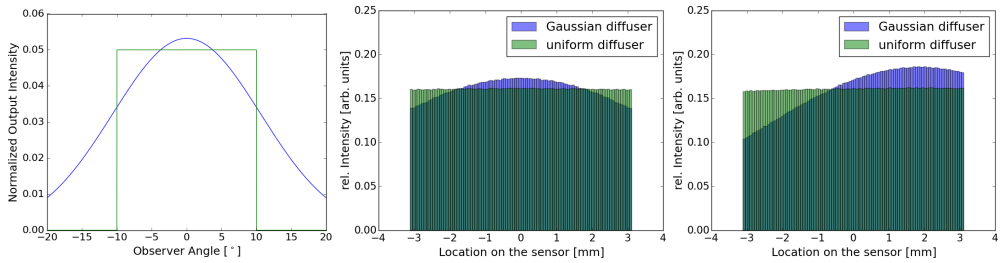

FIGURE 5.6: This simulation data demonstrates the interrelation between the angular spectrum of the source (a) and the resulting illumination uniformity in the specimen plane. The relative intensity observable across the sensor is presented in (b) for a centered aperture diaphragm and in (c) for an off-set aperture diaphragm (i.e. an oblique illumination).

- For optimizing the radiometric properties of the illumination it is desirable that the size of the image is only as large as necessary. The irradiance is anti-proportional to $(h^i_{coll})^2$ as the light is distributed across the illuminated area. Hence the best conjugate ratio from a radiometric point of view would be defined by the image size in relation to the maximal displacement of the aperture diaphragm ($h^i_{coll} = r_d + r_{apt}$).

In any case, according to Tab. 5.1 a bi-convex lens is best suited for relay imaging with a conjugate ratio between 0.2 and 5.0. In this study a conjugate ratio of ≈ 1 was chosen to allow scope for experimental adjustments rather than optimizing the radiometric output. The collector lens employed in this study is a spherical bi-convex lens (*Thorlabs* LB1761-A) with a focal length of $f_{coll} \approx 25.4\,\text{mm}$.
In the alignment of the Koehler illumination, the condenser lens is inserted at an infinite conjugate ratio. For this purpose the overview in Tab. 5.1 suggests to utilize either best form lenses, plano-convex condensers or aspheric condensers. As best form lenses are only available at a diameter of 25.4 mm, using such a lens would significantly limit the maximal possible shift of the aperture diaphragm. Plano-convex condenser lenses and aspheric condenser lenses are essentially designed for the same purpose. Aspheric condensers offer better performance whereas plano-convex condensers are usually more cost efficient. As the performance of the condenser lens is critical for the illumination quality, an asphere is better suited for our application. However, to ensure that such a lens is indeed the best match for the application both lens forms were tested in a simulation (cf. complementary data in Appx. B.3). It was found that both lenses offer good on-axis performance, while an oblique illumination scenario leads to an inhomogeneous background for the spherical lens.
The aspheric lens chosen in this study (*Thorlabs* ACL4532-A) offers a high numerical aperture of NA = 0.6. The high numerical aperture is particularly useful, as the best performance is usually achieved in the center of a lens and decreases towards the periphery. While the numerical aperture exceeds the requirements (the numerical aperture of the objective lens is $\text{NA}_{obj} = 0.2$), it allows us to only use the central part of the lens and avoid significant deviations.

The Complete Optical Train

After carefully specifying all components, the illumination system and microscope optics can be set up. The CAD drawing in Fig. 5.7 visualizes the complete optical train as constructed on the breadboard system. In this setup the aperture diaphragm was connected to a manual x-y-stage to enable radial off-sets in arbitrary directions, which has to be motorized in the final design of the microscope.
The linear analyzer and quarter-wave plate were placed in the infinity path of the microscope optics. The angle between waveplate and linear analyzer (which needs to be exactly 45°) was calibrated by using a known circular polarizer as a sample and adjusting the angle to achieve maximal obliteration.
The linear polarizer was placed together with the bandpass filter into a motorized rotation stage between field and aperture diaphragm. The motorized rotation stage was driven by an axes controller, that was programmed[7] to trigger the camera to facilitate a continuous image acquisition for the 18 images of a standard 3D-PLI measurement.
The size of the aperture diaphragm influences several properties of the illumination system. As the aperture diaphragm is located in a reciprocal plane to the specimen, it controls the angular spectrum of the illumination. Therefore, an increase in its diameter leads to a larger numerical aperture of the illumination. This is in general beneficial for the irradiance of the illumination system, but also implies a broader distribution of rays around the desired oblique illumination angle. Additionally, due to the wave properties of light, this diaphragm can also cause diffraction effects which are more pronounced the smaller the diameter of the diaphragm.
Based on the implementation of the optical train, the effects of the aperture diaphragm were studied experimentally. The diameter of the aperture diaphragm was varied from $d_{apt} = 1\,\text{mm}$ to $d_{apt} = 7\,\text{mm}$. The illumination homogeneity was evaluated based on a diagonal profile of the measured intensity values.
Fig. 5.8 features the measured background intensity profile for different diameters of the aperture diaphragm. The data shows that for diameters between $d_{apt} = 1\,\text{mm}$ and $d_{apt} = 4\,\text{mm}$ the background uniformity increases, while diameters above $d_{apt} = 5\,\text{mm}$ yield no significant changes in the intensity profile. In principle a non-uniform background can be easily compensated by an intensity based calibration (i.e. measured intensity values are divided by the background intensity cf. Chap. 3). However, post measurement data cleaning has secondary side effects such as a loss in the signal noise ratio. Therefore the reduction of necessary calibration efforts to a minimum is preferred. Based on the measured profiles a diameter of $d_{apt} = 4\,\text{mm}$ is chosen as the best compromise between a uniform background illumination and a well defined oblique angle.
In first experimental tests it was determined that with this setup the maximal possible shift of the aperture diaphragm is $r_d = 3\,\text{mm}$, before the field of view is partly shadowed. By simulating the setup with the exact lenses and spacings as those in the experiment, the respective oblique angle was determined to $\tau_{ext} = 5.7°$ (cf. Fig. 5.9). This value is significantly lower than the maximal accepted angle of the objective lens given by $\arcsin(\text{NA}_{obj}) \approx 11.5°$. By considering that the illumination in the specimen plane is not collimated, but also has a numerical aperture, the observed discrepancy can be explained. In the simulation of the experimental setup the opening angle of the illumination was determined to $\theta_{illu} \approx 3.5°$, given an aperture diaphragm opening of $r_{apt} = 2\,\text{mm}$. For every oblique angle τ not only the central ray but also rays with an angle of $\tau \pm \theta_{illu}$ need to be within the acceptance range of the objective lens or illu-

[7] Philipp Schloemer programmed the script for the axes controller.

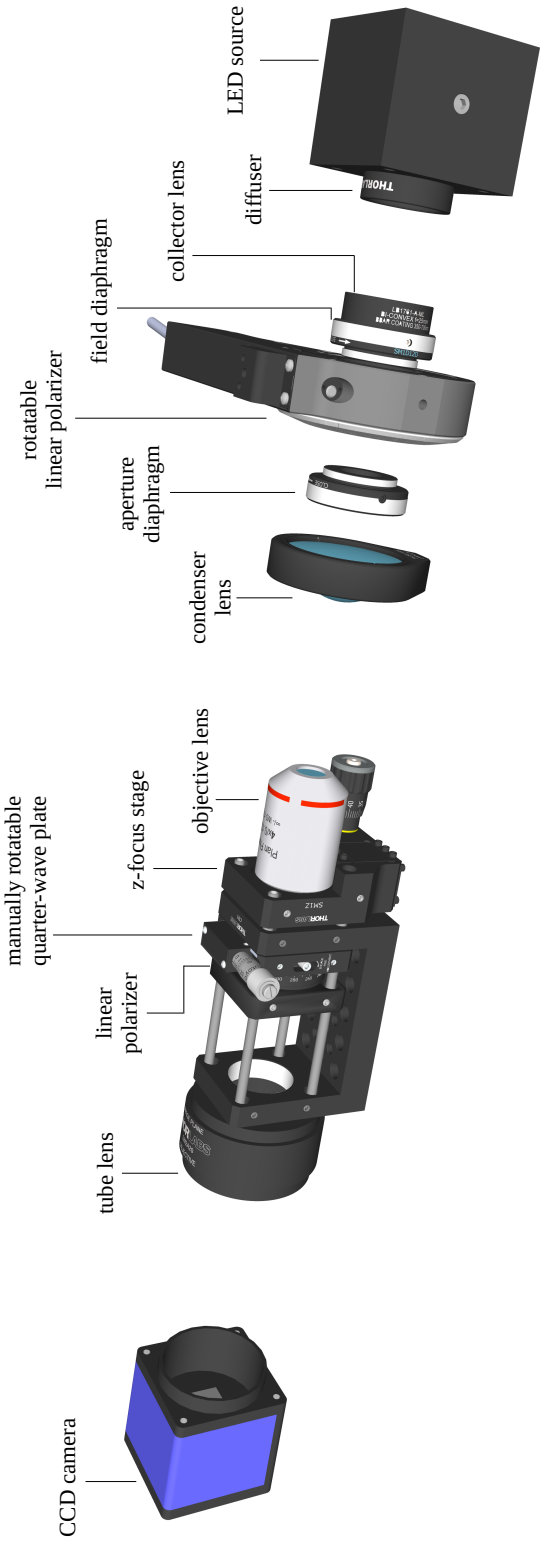

FIGURE 5.7: CAD drawing of the optical setup. The rotation stage for the quarter-wave retarder makes it possible to calibrate the angle between waveplate and linear polarizer to 45°. The manual z-stage at the objective lens allows the specimen to be brought into focus. The aperture diaphragm is connected to an x-y-stage (which is not visible in the drawing for visualization purposes) thereby making it possible to shift the diaphragm off center. The linear polarizer is mounted in an automated rotation-stage and can be triggered to conduct a standard 3D-PLI measurement automatically.

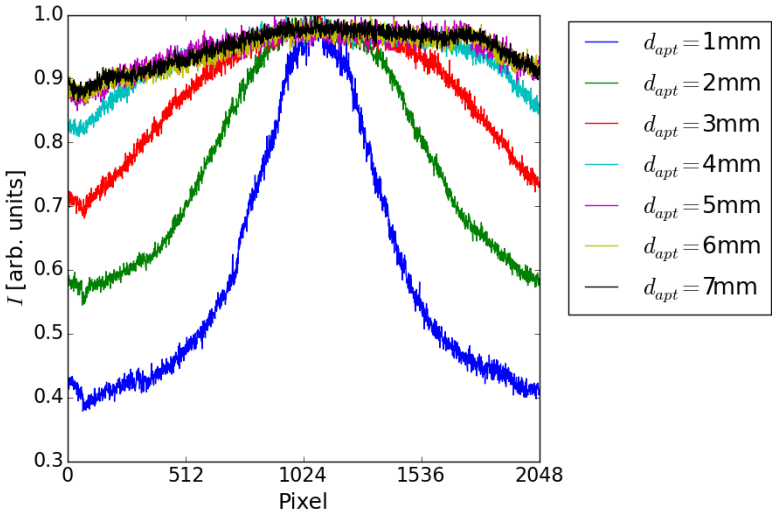

FIGURE 5.8: Measured background intensity profiles for different diameters of the aperture diaphragm. The uniformity improves with an increase in the diameter up to $d_{apt} = 4\,\text{mm}$. A further increase yields no major changes in the profile.

mination artifacts are likely to occur. Taking this into account the experimental setup ($5.7° + 3.5° = 9.2°$) is close to the theoretical limit placed by the objective lens (11.5°). The remaining difference can be explained by a component (e.g. the diameter of a filter mount) in the imaging path additionally limiting the acceptance angle.
The polarizing microscope is now equipped with a fully functional oblique illumination system that achieves an oblique angle of up to $\tau = 5.7°$. While the system was carefully optimized, it still needs to be examined whether such an oblique illumination system is capable of providing additional measurements that improve the interpretation of nerve fiber orientations in a histological brain specimen.

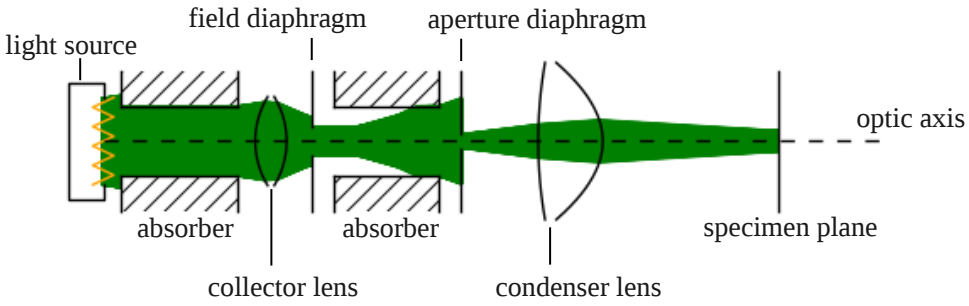

(a)

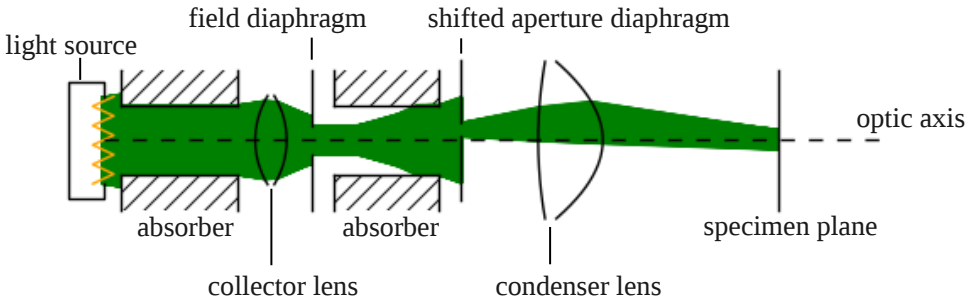

(b)

FIGURE 5.9: Simulation of the experimental setup for a centered (a) and an off-set aperture diaphragm (b).

5.5 Validating the Oblique Illumination System for 3D-PLI

The illumination system has been designed and carefully optimized from an engineering point of view. In the next step, the validity of the approach for its application in 3D-PLI is tested experimentally by measuring and analyzing actual brain tissue. By applying the algorithms developed in Chap. 4 to the acquired data, it is assessed whether data acquired with the oblique illumination is equivalent to the data acquired with the tiltable specimen stage in the LAP.

Methods

For evaluating the capabilities of the oblique illumination system, a coronal section of a rat brain was examined. This section features the corpus callosum (cc), external capsule (ec) and the caudate-putamen (CPu), thereby providing both in-plane and out-of-plane oriented structures (regions were labeled according to [60, p. 31]). As the developed microscopic system was only a prototype on a bread board, acquiring a complete tiled scan of the sample was not possible. Instead only a single field of view was recorded.
The measurement with the prototype was carried out according to the standard 3D-PLI procedure (i.e. images were recorded for 18 different rotation angles of the polarizer with a sampling step size of 10°). One measurement was conducted with the aperture diaphragm in the central position and $N_t = 12$ oblique measurements with the aperture diaphragm being displaced along a circle with radius $r_d = 3\,\text{mm}$. Consequently, the x- and y-position of the aperture diaphragm were determined by

$$x = r_d \cos(\psi_i),$$
$$y = r_d \sin(\psi_i),$$

with $\psi_i = \frac{2\pi(i-1)}{N_t}$ as the direction of the oblique illumination (which is equivalent to the tilting direction in Chap. 4), whereas $i \in [1, 2, ..., N_t]$.
In the developed microscope it is only possible to rotate the polarizer but not the analyzer, hence the polarimetric calibration developed in Sec. 3.2 could not be applied. As only high quality polarization filters are employed, a full polarimetric treatment of the calibration is not required and the data is only corrected by an intensity based calibration as presented in Sec. 3.1. Due to the limited automation of this preliminary setup, only one flat frame was recorded for every position of the polarizer instead of 100.
In order to analyze the generated data with the algorithms, it is necessary to know the oblique angle τ that results from a given radial displacement r_d of the aperture diaphragm. To determine the best possible estimate for this angle, the experimental setup was simulated with respect to the employed lenses (cf. Sec. 5.4.3) and the spacing between the optical elements. For $r_d = 3.0\,\text{mm}$ the oblique angle generated by the aperture displacement was determined to $\tau_{ext} \approx 5.7°$. This external oblique angle translates to an internal angle of $\tau_{int} = \arcsin(\sin(\tau_{ext})/n_{brain}) \approx 3.9°$ (cf. Sec. 4.2)
With the determination of these angles, measured signals can be interpreted by the LORIE and the DFT-based algorithms that have been introduced in Chap. 4. Based on the results of the algorithms, t_{rel}-weighted FOMs are created for an initial screening. For a more quantitative analysis, the statistical distribution of the determined inclination values is examined and the results of both algorithms are compared. The retardation

signals for different oblique angles (specified by τ and ψ_i) are compared to the theoretically model in exemplary pixels.
The working principle of the oblique illumination was validated by comparing it with a LAP measurement of the same sample. While the data acquisition with the tiltable specimen stage in the LAP is well understood, it also provides less information due to its limited resolution. In order to ensure the comparability between the two imaging systems, the acquired microscopic images were downscaled by a factor of 32 (grayscale values in neighboring pixels were averaged) so that the pixel size in object space is almost identical to the one of the LAP. The resulting inclination maps were evaluated by comparing FOMs and histograms. To analyze the process of downscaling the microscopic data, the *cumulative distribution functions (CDF)* of the calculated inclinations were compared for a downscaling factor of 2^m with $m \in \{2, 3, 4, 5\}$.
By calculating the variance pixelwise across all generated retardation maps for the different oblique illumination directions, it is possible to visualize regions with a drastic change in retardation. This approach makes it possible to reveal certain artifacts such as perspective shifts for an otherwise stationary specimen.

Results

After calculating the inclination and the t_{rel} map from the acquired data with the two algorithms, t_{rel} weighted FOMs were generated for visualization[8]. Fig. 5.10 features the resulting FOMs for the DFT-based algorithm in the left column and for the LOriE algorithm in the right column. When examining the complete field of view (first row in Fig. 5.10), it is can be seen that both algorithms yielded similar orientations for the corpus callosum (the dense fiber tract that is visible in the upper right corner) and the external capsule (the fiber tract at the left boundary of the image). In contrast, the calculated orientations in the CPu (the region in the center of the image) displayed differences between the two algorithms. While several of the white matter tracts are colored similarly, overall the DFT-based results are dominated by a strong z-component (indicated by the blue hue). The orientations calculated by the LOriE algorithm on the other hand, indicate the presence of in-plane fiber structures (indicated generally by the more disperse coloring and especially the green hue in some areas).
The ROIs presented in Fig. 5.10 (second and third row) make it possible to examine the results in more detail. In the first ROI a part of the cortex bordering the external capsule is presented. The FOM that is generated based on the results of the LOriE algorithm shows that a few fibers (visible as dark green lines) branch from the white matter into the cortex. These fibers are oriented within the section plane and the t_{rel} weighting causes a darker coloring in comparison with similar oriented white matter fibers. In the FOM generated by the DFT-based algorithm these fibers are barely visible and noise dominates the signal in the cortex.
The second ROI (third row of images in Fig. 5.10) features a part of the CPu. In this region, both algorithms calculated a large out of plane component (indicated by the blue coloring) for the truncated fiber bundles. However, the reconstruction is not uniform across each fiber bundle and the coloring is different towards a specific edge of each bundle. In the area between these fiber bundles a field of birefringent in-plane fibers is visible in the LOriE reconstruction whereas in the FOM of the DFT-based approach only noise is observed between the truncated fiber bundles.
For a statistical overview of the results Fig. 5.11 shows histograms of the reconstructed

[8] cf. Sec. 4.3.3 for details on t_{rel} weighted FOMs.

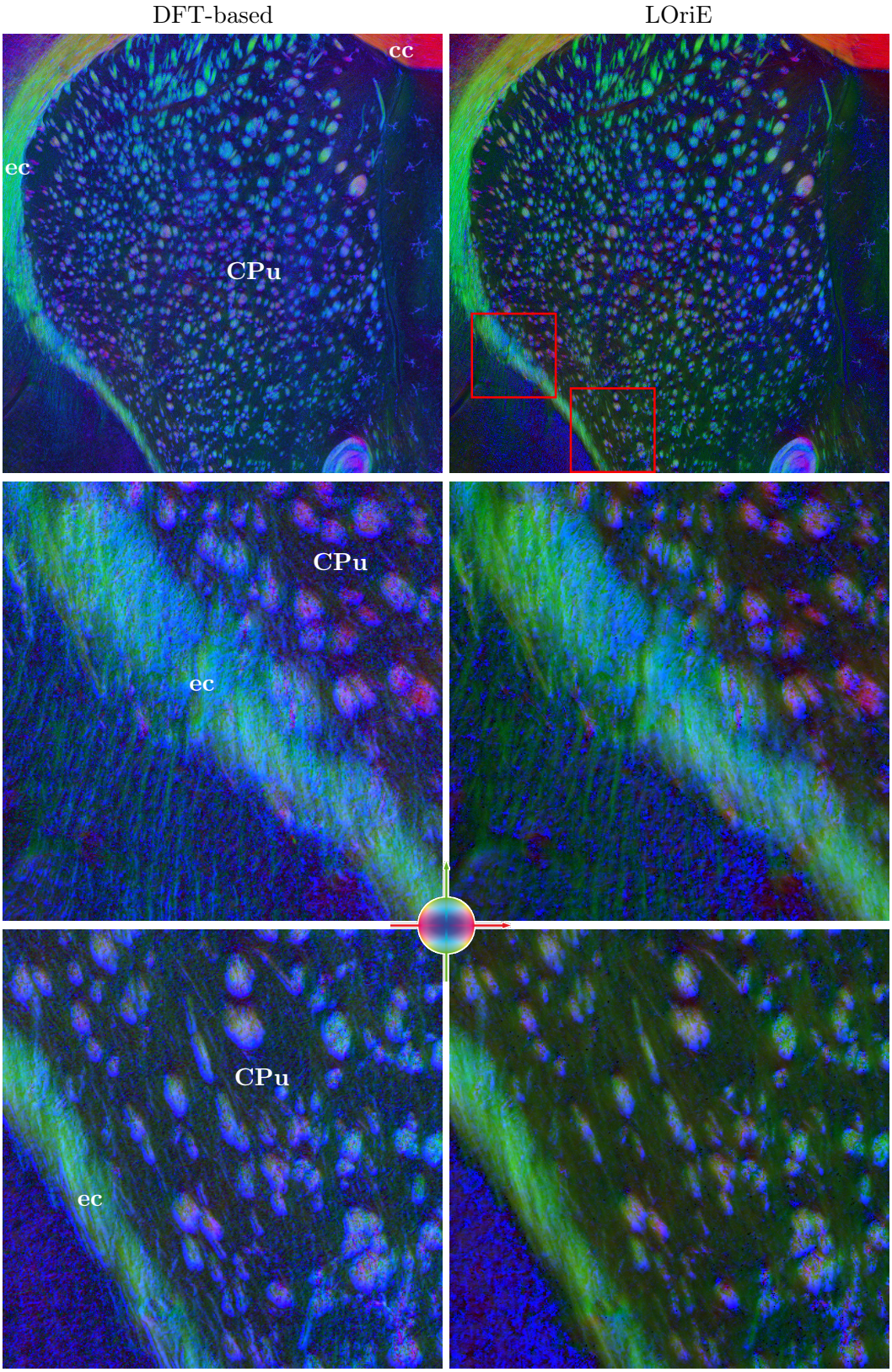

FIGURE 5.10: t_{rel}-weighted FOMs generated from the results of the DFT-based algorithm (left column) and from the results of the LOriE algorithm (right column). The coloring represents the orientation while the brightness of the colors indicates the respective t_{rel} value. The first row features the complete field of view, while the second and third rows display two ROIs to visualize the results in more detail.

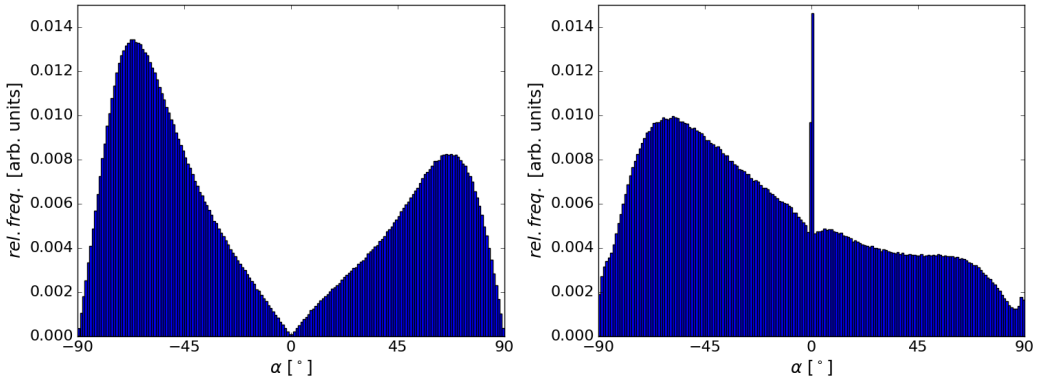

(a) DFT-based algorithm (b) LOriE algorithm

FIGURE 5.11: Histogram of the inclination across the whole field of view. The inclination was calculated from the oblique measurements by employing the DFT-based algorithm (a) and the LOriE algorithm (b).

inclination angles across the entire field of view. The inclinations reconstructed with the DFT-based algorithm assume most frequently values of $\alpha \approx \pm 70°$, while values of $\alpha = 0°$ and $\alpha = \pm 90°$ are virtually non-existent (cf. Fig. 5.11a). In between these boundary values the relative frequency of occurrence scales almost linearly.
On the other hand the LOriE reconstruction offers a more disperse range of inclinations. While there is a clear maximum at $\alpha \approx -70°$, all other inclination values are still quite common. Additionally it is noticeable that there is a singular peak at an inclination value of $\alpha = 0°$ which disrupts the otherwise smooth distribution (cf. Fig. 5.11b).
Overall there are significant differences in the fiber orientation reconstruction with the two algorithms, but there is also a common ground with $\alpha \approx -70°$ being the most frequent inclination value in both reconstructions.
In order to understand why the two algorithms display these differences in their respective results, the underlying retardation values were examined. Fig. 5.12 shows the retardation values for the different oblique measurements in two exemplary pixels, as well as the models describing the expected retardation values. The reconstructed values of the model parameters α and t_{rel} are given in the table below.
For both algorithms the square root of the mean squared error $\Delta \sin(\delta)$ was calculated as a measure for the deviation between measurement and theory. In all cases the deviation is quite high and about an order of magnitude larger than the one observed in the LAP (cf. Sec. 4.3.3). For both pixels the deviation for the LOriE algorithm is slightly lower than for the DFT-based algorithm. Additionally both algorithms calculate values of $t_{\text{rel}} > 1$, which violates the premise of $t_{\text{rel}} \leq 1$ that has been made to avoid ambiguities in the theory (cf. Sec. 4.3.1).
After downscaling the measurement data and recalculating the inclinations with the LOriE algorithm, the t_{rel} weighted FOM for the LAP and the developed oblique PM deliver comparable results (cf. Fig. 5.13). Based on the FOMs no significant differences in the reconstructed orientations are visible. The resolution in the downscaled microscopic image (cf. Fig. 5.13a) is higher than in the LAP image (cf. Fig. 5.13b), as the downscaling procedure of the oblique PM data was only conducted with respect to the sampling rate but not the optical resolution.
Comparing the relative frequency of occurrence of the inclination values by considering the histograms in Fig. 5.14a yields similar observations. The main difference between

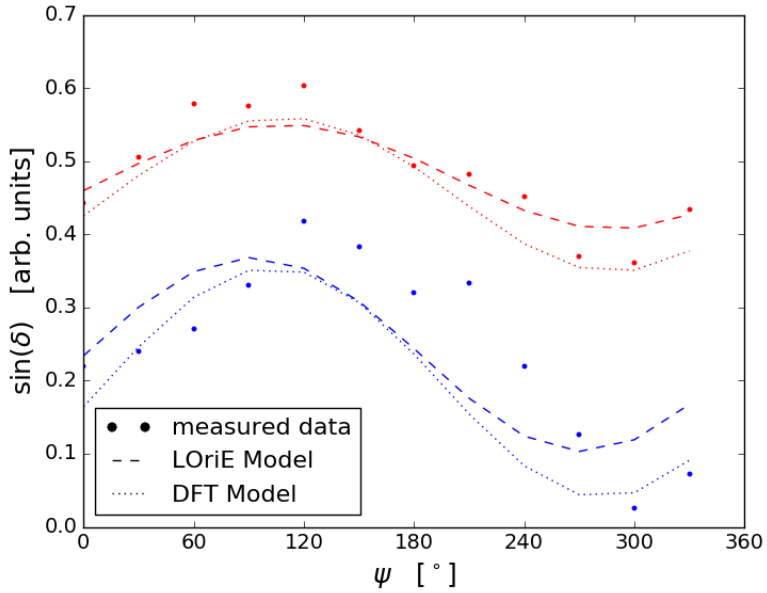

	Red data			Blue data		
	α	t_{rel}	$\Delta \sin(\delta)$	α	t_{rel}	$\Delta \sin(\delta)$
LOriE	$-50.2°$	0.78	0.09	$-77.7°$	3.06	0.15
DFT	$-61.7°$	1.33	0.11	$-82.2°$	5.64	0.17

FIGURE 5.12: The plot shows the measured retardation values of the oblique measurements for two different pixels (red and blue data points). The dashed line indicates the theoretically expected retardation values based on the inclination and t_{rel}-value reconstructed by the LOriE algorithm. The dotted line represents the theoretical model for the DFT-based algorithm. The table below contains the model parameters reconstructed by the respective algorithm and the deviation between measurement and theory.

the two histograms is the slightly more pronounced peak at $\alpha \approx -35°$ in the LAP data. To evaluate the role of downscaling the data, the cumulative distribution function (CDF) of the inclination is evaluated for multiple resolution steps in Fig. 5.14b. At the original microscopic resolution the CDF represents a broad distribution of inclination values (a uniform inclination distribution would be represented by a linear CDF). By artificially downscaling the data, the CDF converges continuously towards the CDF for the LAP. At a scaling factor of 32 which represents approximately equal pixel sizes in object space, only minor differences between the CDF for the LAP and the CDF for the oblique PM are still visible. In the microscopic data a small step increase in the CDF is observable at $\alpha = 0$, which is not present in the LAP data and which becomes smaller with higher downscaling factors.
The inclinations reconstructed with the DFT-based algorithm are distributed differently (as was shown in Fig. 5.11) but they converge to the distribution for the LAP as well when downscaling the image data. The respective results can be found in Appx. B.4. Fig. 5.15 displays the variance of the retardation across all oblique measurements. While the variance in the background assumes values between $\text{Var}[\sin(\delta)] = 0$ and $\text{Var}[\sin(\delta)] = 0.2 \times 10^{-2}$ the variance observed for truncated fiber bundles reaches values of $\text{Var}[\sin(\delta)] = 1.0 \times 10^{-2}$. At the edges of the bundles, the observed variance increases even further and values of $\text{Var}[\sin(\delta)] = 2.0 \times 10^{-2}$ and above are observed. Hence, the truncated fiber bundles of the CPu are clearly visible in this variance map

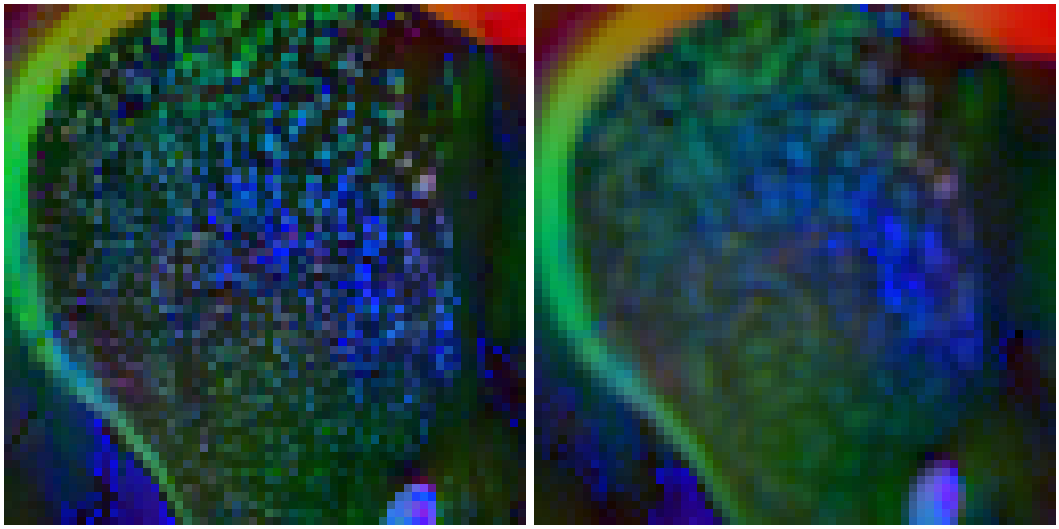

(a) (b)

FIGURE 5.13: t_{rel}-weighted FOM for the downscaled microscopic data (a) and the LAP data (b) based on inclinations derived with the LOriE algorithm. The LAP image is blurred in contrast to the downscaled microscope, as the limited optical resolution of the LAP was not considered when downscaling the microscopic images. Overall, the coloring is very similar, meaning that the reconstructed orientations are comparable.

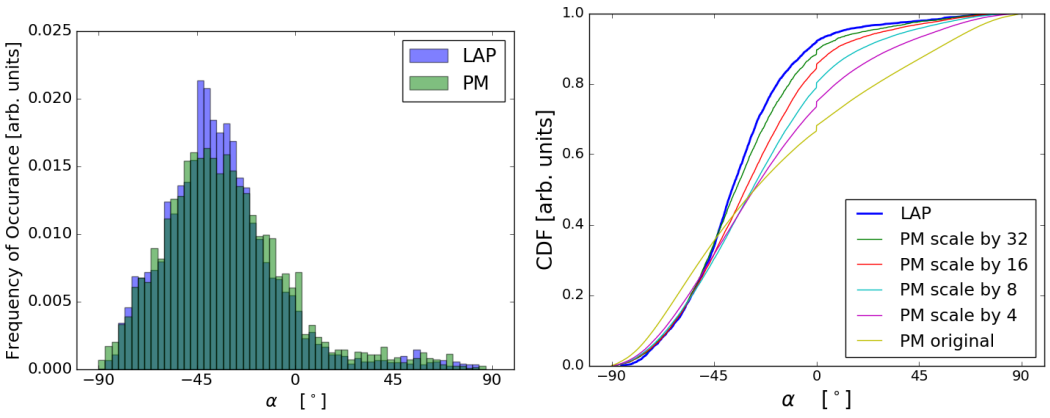

(a) (b)

FIGURE 5.14: Analysis of the distribution of inclinations that were calculated by the LOriE algorithm. The distribution of inclinations derived on the bases of the downscaled data of the oblique illumination system resembles the distribution that is based on the data acquired with the tiltable specimen stage in the LAP (a). The CDFs in (b) show that the original distribution of inclinations derived from the microscopic data converges to the CDF of inclinations in the LAP.

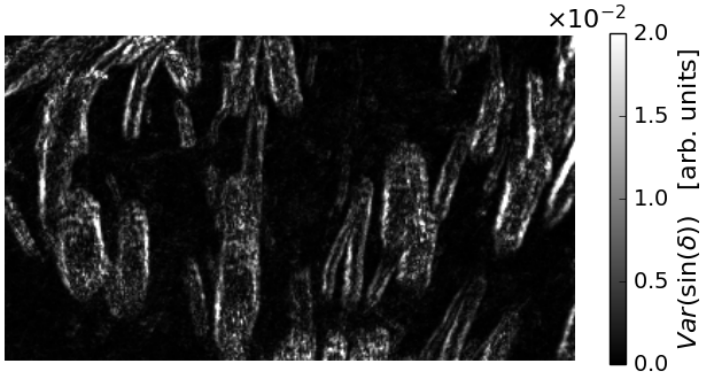

FIGURE 5.15: Variance across all retardation maps of the different oblique measurements. In the displayed ROI the boundaries of truncated fiber bundles in the CPu are clearly highlighted.

and especially their boundaries are highlighted.

Discussion

In this proof of principle measurement the new oblique illumination system made it possible to acquire a dataset that could be analyzed with the algorithms presented in Chap. 4. By downscaling the original data to the resolution of the LAP and comparing the results of both systems, it has been demonstrated that the developed oblique illumination system provides the same advantages as the tiltable specimen stage in the LAP. The derived FOMs and the histograms of the inclination are very similar for both systems. In the FOMS at the original resolution, the LOriE algorithm in particular provided a graphic representation of the fiber structure which is rich in detail and makes it possible to reconstruct even single nerve fibers. While the visualization of single nerve fibers has been achieved in previous studies on 3D-PLI microscopy [5], now for the first time a bias free reconstruction of the orientation vectors has been performed.
Upon comparison of the results of the two available algorithms major differences in the data interpretation are revealed as well. Overall the DFT-based algorithm predicts more inclined fibers than the LOriE algorithm with a strong bias towards an inclination of $\alpha \approx \pm 70°$. While the value $\alpha \approx -70°$ is also predominant for the inclinations calculated by the LOriE algorithm, overall the distribution is much more uniform. The distinct value of $\alpha \approx -70°$ is plausible for the field of truncated fiber bundles in the CPu, which explains its predominance in both modalities.
On the other hand, the external capsule and the fiber structures visible in the cortex suggest also the presence of fibers with a strong in-plane component (i.e. an inclination of $\alpha \approx 0°$). However, such orientations were only reconstructed by the LOriE algorithm. The strong peak in the distribution of the LOriE-reconstructed inclinations at $\alpha = 0°$ indicates a lack of sensitivity when trying to distinguish between in-plane fibers with slightly different inclinations. In proximity to this peak a small dip in the histogram is observed which supports this interpretation (cf. Fig. 5.11b).
While overall the inclination values provided by the LOriE analysis are more plausible, it is important to recognize that the ground truth is unknown. Hence, the scenarios implied by the two modalities are both possible. Furthermore, the strong discrepancy

between the two modalities indicates that the theoretical model, which both algorithms are based on, is incomplete. This interpretation is supported by the observation of values $t_{\mathrm{rel}} > 1$ which are inconsistent with the premises of the model. The strong discrepancy observed between the measured retardation values and those predicted by the model also indicates that the model is not well-suited to describe the experimental results with a sufficient precision.
Noise sensitivity has been shown to be a source of error, which can lead to discrepancies between the two employed algorithms (cf. Sec. 4.4.4). However, mere detection noise is not sufficient to explain the observed differences. A clue for the major source of error is provided by the variance map across all oblique retardation maps. In general a variance in the retardation is expected from the theoretical model (cf. Sec. 4.3.1) when changing the direction of the oblique illumination. This change should be particularly visible in white matter fiber bundles such as the truncated bundles in the CPu. The strong variance that is solely observed at the edges of fiber bundles on the other hand can only be attributed to a perspective shift when observing the sample for different settings of the oblique illumination.
Such a parallax effect is expected to occur as it is the basis for the optical tomography method developed by Kawata et al. [39] and for light field microscopy [50]. While those imaging techniques utilize the parallax for their respective methodology, in our case it is an undesired secondary effect as it becomes problematic to differentiate between the optical and the polarization effects.
The origin of the perspective shift can be understood by considering the scenario in Fig. 5.16. Two distinct features (red and blue dot) have the same x and y position but one is located in the focal plane while the other is at the surface of the sample. When imaged with a straight illumination, the two features will be superimposed in the final image as they are both in the path of the same ray. For an oblique illumination on the other hand, the two features will appear as separate features in the microscope as they are imaged by different rays. The feature in the focal plane (blue dot) will maintain its position for every oblique illumination, while the apparent position of the surfaces feature depends on the respective illumination settings and will be different for every oblique angle[9].
The magnitude of the shift depends on the distance of the considered object to the focal plane (i.e. at most half of the sample thickness) and on the angle of the oblique illumination. Considering the typical sample thickness of $t = 70\,\mu\mathrm{m}$ and an oblique angle of $\tau = 5.7°$ this means that the apparent displacement for a feature at the sample surface is approximately $t/2 \cdot \tan(\tau) \approx 3.5\,\mu\mathrm{m}$, which corresponds to roughly two to three image pixels. In the experiment this effect can become larger if the focal plane is not placed exactly in the center of the sample, or if the sample is not exactly parallel to the focal plane. While this shift is particularly problematic at the boundaries of any fiber structure where large variations in the birefringence occur, it is bound to lead to deviations from the theoretical model in almost any case, as even thick white matter fiber bundles cannot be considered as homogeneous on a microscopic resolution.
To resolve this issue several approaches can be considered. While reducing the sample thickness seems the most straightforward, to date the lowest section thickness that has been achieved for 3D-PLI at a steady quality is $t = 70\,\mu\mathrm{m}$ for human brains and $t = 60\,\mu\mathrm{m}$ for rodent brains. This limitation is mostly due to the cryogenic preparation technique used in 3D-PLI (cf. Sec. 2.5) and is unlikely to change in the near future.

[9] As a secondary effect, the feature located at the surface of the specimen will be blurred. However, in this application the depth of field still makes it possible to image features located close to the surface of the specimen.

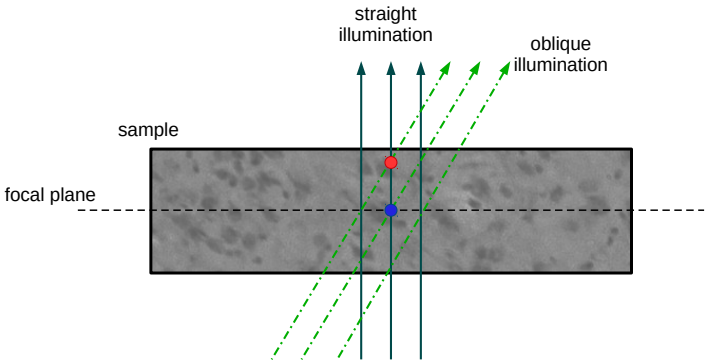

FIGURE 5.16: When imaging a histological specimen with oblique illumination, parallax effects can cause an apparent displacement of certain features. In this example, one feature of the histological brain section is located exactly in the focal plane of the microscope (blue dot) while a second feature (red dot) is located close to the surface of the specimen. When imaged with a straight illumination these two features will be superimposed. An oblique illumination on the other hand will image the two features next to each other, as they are no longer in the light path of the same ray.

Reducing the camera resolution so that the shift of structures is below the resolution limit of the imaging system would also be possible. As one big advantage of 3D-PLI over other imaging techniques is its rich detail in microscopic images, this solution is not considered as it would trade a main advantage of 3D-PLI in favor of an easier data interpretation. While applying the LOriE analysis seems to provide reasonable results, in future studies the data analysis should be adapted with respect to a suitable model that describes both parallax and polarimetric effects in a polarizing microscope equipped with an oblique illumination system. Eventually, exploring such a comprehensive model might not only make it possible to calculate fiber orientations free of aberrations but also allow a z-axis resolution that exceeds the section thickness.
By studying the cumulative distribution function of the inclination values it was also possible to reveal a resolution dependent effect in the reconstruction. This effect can be explained in part by the parallax effect described above. As this effect is only relevant at a microscopic resolution, its influence should not extend to the mesoscopic scale. However, downscaling the microscopic data by a factor of 32 still leaves minor differences in the reconstruction between the oblique PM and the LAP. Hence, a large part of the difference in the CDFs is probably attributed to the increased sensitivity of the microscopic system towards small fiber structures that are oriented differently than the surrounding structures. When downscaling the data for such diverse structures, a gradual change of the CDF would be expected as was observed in Fig. 5.14b.
Overall, this proof of principle experiment demonstrated that the developed microscopic system is capable of providing additional data to the established microscopic 3D-PLI measurement, similar to the tiltable specimen stage system employed in the LAP. It has been shown that the measured data can be interpreted to some extent with algorithms originally developed for the LAP. While the analysis methodology still needs to be improved, the developed illumination system is a major step in ensuring that the capabilities of the microscope do not fall short in comparison with the LAP.

5.6 Conclusion

In this chapter an oblique illumination system was developed in order to enable measurements similar to those provided by the tiltable specimen stage in the LAP. The designed setup was based on the Koehler illumination and chosen as it does not significantly change the image acquisition and still makes it possible to perform standard 3D-PLI measurements. This advantage means that most of the standard 3D-PLI workflow can be maintained and ensures the comparability to the previous microscopic 3D-PLI measurements. The steps described in Sec. 5.4.3 not only enabled us to build this specific oblique illumination system, but also provide a general approach on how to design such a system for any given microscope. In the future, this might lead to advances in other microscopy applications, that could benefit from a well adjusted oblique illumination system.
It has been demonstrated that the oblique illumination can be utilized in a polarizing microscope to deliver similar information to that provided by the tiltable specimen stage in the LAP. On the basis of the acquired data it was possible to reconstruct the fiber orientations in an exemplary brain specimen by employing the same analysis methods that were developed for the LAP. Hence, the developed illumination system is an important step to ensure that the microscopic system offers the same features as the LAP and thereby enables the scalability of 3D-PLI. While these results are promising it was also discovered that the theoretical model developed for the LAP falls short of including optical effects in addition to the polarimetric theory. To utilize the additional data generated with the oblique illumination to the full extent, the theoretical model and the analysis algorithms will need to be refined to account for the observed parallax effects. Extending the theoretical model and respective data analytics in the future will not only improve the accuracy of reconstructed orientation but also offers the possibility to increase the z-axis resolution.

6

Impact on Future 3D-PLI Data Interpretation Techniques

Until now, the reconstruction of 3D-PLI orientation vector fields was only quantitatively reliable in deep white matter regions with a steady fiber density. This limitation was inherent in the 3D-PLI analysis as the polarimetric effects of fiber orientation and fiber density are always combined to a single measurand. In this work, it was demonstrated that complementing a planar 3D-PLI measurement with additional measurements from a tiltable specimen stage yields information that makes it possible to separate the orientation vector field from the fiber density. By exploiting the additional information, for the first time it was possible to access these two types of information independently of each other.

For the required data analysis, two algorithmic approaches were developed, which differ in terms of noise sensitivity and required computational resources. The first *DFT-based* algorithm utilized an analytical calculation derived from the polarimetric model of a 3D-PLI measurement, whereas the second *LOriE* algorithm employed a probabilistic approach. Proof of principle experiments provided conclusive evidence that utilizing this framework makes it possible to reconstruct the fiber architecture in a multitude of different fiber scenarios.

While the working principle of this algorithmic framework has been thoroughly investigated, it is desirable to conduct further studies in the future that focus on the possibility to exploit more of the information provided by the tiltable specimen stage especially for the purpose of investigating crossing fiber scenarios. To this end, analyzing simulations of the 3D-PLI pipeline with the *SimPLI* toolkit developed by Dohmen et al. [19] is particularly interesting as measured signals can be simulated for a broad variety of fiber constellations. Eventually this approach might make it possible to extend the current model of a single fiber orientation per voxel towards a comprehensive model that is also capable of describing a disperse distribution of fibers within one voxel.

In this context, it is also interesting to investigate the applicability of a full Mueller polarimeter as described by Chipman et al. [13] in contrast to the partial Mueller polarimeter currently used for 3D-PLI measurements. While the current polarimetric approach is sufficient for a purely birefringent specimen, other (minor) effects such as depolarization and diattenuation cannot be investigated. It has been theorized [25] that especially depolarization might be indicative for the dispersity of the fiber architecture.

As this study has for the first time presented a comprehensive treatment of the 3D-PLI data analysis with the Mueller-Stokes calculus, a first step towards such an approach has been made. Though the benefit of the Mueller-Stokes calculus in this study was

limited to the calibration procedure, it also opens up the possibility of employing state of the art polarimetric techniques in future studies on 3D-PLI.
So far, the benefit of a tiltable specimen stage for 3D-PLI data analytics has been restricted to mesoscopic setups due to the inherent optical limitations of a microscope. In the course of this thesis an oblique illumination system was specifically developed for 3D-PLI microscopy in order to facilitate equivalent data analytics at a high resolution. It has been demonstrated that the collected data can be used to apply the same information processing principles as in a mesoscopic system. However, it was also discovered, that due to the high resolution further optical effects occur which inhibit the current data analytics at full resolution but might also carry valuable additional information.
An important issue for 3D-PLI is that while the resolution in the x-y plane is dependant on the optical setup, the z-axis resolution is determined by the thickness of the examined histological brain section. At the mesoscale this leads to an approximately isotropic resolution whereas at the microscale the height of a voxel exceeds its x-y dimensions by a factor of approximately 50. By introducing optical tomography methods to 3D-PLI microscopy, it might be possible to resolve this impairment and increase the z-axis resolution. However, this requires a novel theoretical approach as the oblique illumination system introduces a combination of optical and polarimetric effects that have not been described yet.
The new methods that have been explored in this study have demonstrated that linking theoretical models and experimental data yields huge benefits for 3D-PLI data analytics and will advance the capabilities of this imaging method in the future.

Acknowledgments

First and foremost, I would like to thank Dr. Markus Axer and Prof. Dr. Uwe Pietrzyk for their guidance and support during the whole project, as well as Dr. Kurt Hoffmann from Taorad GmbH for the collaboration on the microscope and the lab resources that were provided for me.

Furthermore, I would like to express my sincere gratitude towards my colleagues for the stimulating discussions and the moral support I received in the last four years. In particular, I want to thank Philipp Schlömer for the many lab hours we spent together on the construction of the microscope and the oblique illumination, as well as Tim Hütz and Stefan Köhnen who implemented a HPC interface for the LOriE algorithm.

For their help in revising the manuscript, a special thanks goes to Julia Reckfort, Philipp Schlömer, Markus Axer, Stefan Köhnen, Miriam Menzel, Giuseppe Tabbi and Ken Plaxton. Their many insightful comments helped to significantly improve this thesis.

The study has been made possible by the financial support of the PhD scholarship initiative of the University of Wuppertal and the Helmholtz Association through the Helmholtz Portfolio Theme “Supercomputing and Modeling for the Human Brain”.

Appendix A

Mathematical Derivations

A.1 Derivation of $n_e(\alpha) - n_o \approx (n_E - n_o) \cdot \cos^2(\alpha)$

For a uniaxial index ellipsoid the rotational symmetry makes it possible to reduce the problem to a two dimensional cross section of the indicatrix. Fig. A.1 features the resulting ellipse, which is described by the equation

$$\frac{x^2}{n_E^2} + \frac{y^2}{n_o^2} = 1. \tag{A.1}$$

Using the trigonometric relations

$$\sin(\alpha) = \frac{y}{n_e},$$

and

$$\cos(\alpha) = \frac{x}{n_e},$$

Eq. (A.1) can be written as

$$\frac{n_e^2 \cos(\alpha)^2}{n_E^2} + \frac{n_e^2 \sin(\alpha)^2}{n_o^2} = 1.$$

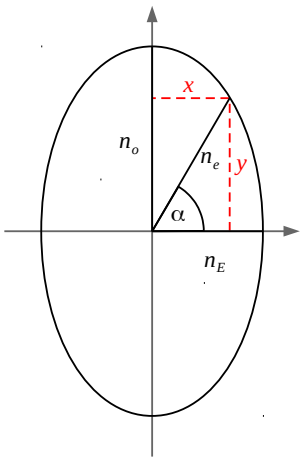

FIGURE A.1: Cross section of the index ellipsoid in order to derive the extra ordinary index from the equation of an ellipse.

From this equation we obtain the inclination dependent refractive index for the extra ordinary ray

$$n_e(\alpha) = \frac{1}{\sqrt{\frac{\cos(\alpha)^2}{n_E^2} + \frac{\sin(\alpha)^2}{n_o^2}}}. \tag{A.2}$$

When trying to approximate this equation for small differences in the refractive indices, we view it as a scalar function $f(n_o, n_E)$. The Taylor expansion of this function in a point (n_o, n_o) to the linear order is given by

$$f(n_o, n_E) \approx f(n_o, n_o) + J_f|_{n_o,n_o} \cdot \begin{pmatrix} n_o - n_o \\ n_E - n_o \end{pmatrix}, \tag{A.3}$$

where J_f denotes the Jacobian matrix

$$J_f = \begin{pmatrix} \frac{\partial f(n_o,n_E)}{\partial n_o} & \frac{\partial f(n_o,n_E)}{\partial n_E} \end{pmatrix}. \tag{A.4}$$

With the partial derivatives

$$\begin{aligned} \tfrac{\partial f(n_o,n_E)}{\partial n_o} &= -\tfrac{1}{2} \cdot \frac{1}{\sqrt{\frac{\sin^2(\alpha)}{n_o^2} + \frac{\cos^2(\alpha)}{n_E^2}}^3} \cdot (-2) \frac{\sin^2(\alpha)}{n_o^3} \\ &= \frac{\sin^2(\alpha) \cdot n_o^{-3}}{\sqrt{\frac{\sin^2(\alpha)}{n_o^2} + \frac{\cos^2(\alpha)}{n_E^2}}^3} \\ \tfrac{\partial f(n_o,n_E)}{\partial n_E} &= -\tfrac{1}{2} \cdot \frac{1}{\sqrt{\frac{\sin^2(\alpha)}{n_o^2} + \frac{\cos^2(\alpha)}{n_E^2}}^3} \cdot (-2) \frac{\cos^2(\alpha)}{n_E^3} \\ &= \frac{\cos^2(\alpha) \cdot n_E^{-3}}{\sqrt{\frac{\sin^2(\alpha)}{n_o^2} + \frac{\cos^2(\alpha)}{n_E^2}}^3} \end{aligned} \tag{A.5}$$

this leads to the linear Taylor expansion of $f(n_o, n_E)$ in (n_o, n_o):

$$\begin{aligned} f(n_o, n_E) &\approx f(n_o, n_o) + J_f|_{n_o,n_o} \cdot \begin{pmatrix} n_o - n_o \\ n_E - n_o \end{pmatrix} \\ &= \tfrac{n_o}{\sqrt{\sin^2(\alpha)+\cos^2(\alpha)}} + \begin{pmatrix} \frac{\sin^2(\alpha) \cdot n_o^{-3}}{\sqrt{\frac{\sin^2(\alpha)}{n_o^2} + \frac{\cos^2(\alpha)}{n_o^2}}^3} & \frac{\cos^2(\alpha) \cdot n_o^{-3}}{\sqrt{\frac{\sin^2(\alpha)}{n_o^2} + \frac{\cos^2(\alpha)}{n_o^2}}^3} \end{pmatrix} \cdot \begin{pmatrix} 0 \\ n_E - n_o \end{pmatrix} \\ &= \tfrac{n_o}{\sqrt{1}} + \begin{pmatrix} , \frac{\sin^2(\alpha) \cdot n_o^{-3}}{\sqrt{n_o^{-2}}^3} & \frac{\cos^2(\alpha) \cdot n_o^{-3}}{\sqrt{n_o^{-2}}^3} \end{pmatrix} \cdot \begin{pmatrix} 0 \\ n_E - n_o \end{pmatrix} \\ &= n_o + \left(\sin^2(\alpha), \cos^2(\alpha)\right) \cdot \begin{pmatrix} 0 \\ n_E - n_o \end{pmatrix} \\ &= n_o + (n_E - n_o) \cos^2(\alpha). \end{aligned} \tag{A.6}$$

Hence, the difference of the refractive indices can be approximated by

$$\begin{aligned} n_e(\alpha) - n_o &\approx (n_o + (n_E - n_o) \cdot \cos^2(\alpha)) - n_o \\ &= (n_E - n_o) \cdot \cos^2(\alpha). \end{aligned} \tag{A.7}$$

A.2 The Intensity Profile for Imperfect Polarization Filters

In order to account for partial polarization and a mismatched quarter-wave retarder in the LAP, the observable intensity profile is derived. According to Eq. (2.18), the birefringent tissue is represented by the Mueller matrix

$$\mathbf{M}_{fiber} = e^{-\mu t}\begin{pmatrix} 1 & 0 & 0 & 0 \\ 0 & \cos^2(2\varphi)+\cos(\delta)\sin^2(2\varphi) & (1-\cos(\delta))\sin(2\varphi)\cos(2\varphi) & -\sin(\delta)\sin(2\varphi) \\ 0 & (1-\cos(\delta))\sin(2\varphi)\cos(2\varphi) & \sin^2(2\varphi)+\cos(\delta)\cos^2(2\varphi) & \sin(\delta)\cos(2\varphi) \\ 0 & \sin(\delta)\sin(2\varphi) & -\sin(\delta)\cos(2\varphi) & \cos(\delta) \end{pmatrix}.$$

As explained in Sec. 3.2 the polarization state generator and analyzer are represented by the Stokes vectors

$$\tilde{\mathbf{S}}_{PSG_{LAP}}(\rho_k) = \frac{I_0}{2}\begin{pmatrix} 1 \\ p\cos(\gamma)\cos(2\rho_k) \\ p\cos(\gamma)\sin(2\rho_k) \\ -p\sin(\gamma) \end{pmatrix},$$

$$\tilde{\mathbf{S}}^{\dagger}_{PSA_{LAP}}(\rho_k) = \frac{1}{2}\begin{pmatrix} 1 & -p\cos(2\rho_k) & -p\sin(2\rho_k) & 0 \end{pmatrix}.$$

Next, the intensity profile for these states has to be calculated. In an intermediate step, we calculate:

$$\tilde{\mathbf{S}}^{\dagger}_{PSA_{LAP}}\mathbf{M}_{fiber} = \frac{e^{-\mu t}}{2}\begin{pmatrix} 1 \\ -p\cos(2\rho_k)\left(\cos^2(2\varphi)+\cos(\delta)\sin^2(2\varphi)\right) - p\sin(2\rho_k)\left(1-\cos(\delta)\right)\sin(2\varphi)\cos(2\varphi) \\ -p\cos(2\rho_k)\left(1-\cos(\delta)\right)\sin(2\varphi)\cos(2\varphi) - p\sin(2\rho_k)\left(\sin^2(2\varphi)+\cos(\delta)\cos^2(2\varphi)\right) \\ p\cos(2\rho_k)\sin(\delta)\sin(2\varphi) - p\sin(2\rho_k)\sin(\delta)\cos(2\varphi) \end{pmatrix}^{\dagger}.$$

With this equation, it is possible to calculate the expected intensity profile:

$$\begin{aligned} \tilde{I}(\rho_k) =& \tilde{\mathbf{S}}^{\dagger}_{PSA_{LAP}}\mathbf{M}_{fiber}\tilde{\mathbf{S}}_{PSG_{LAP}} \\ =& \frac{I_0 e^{-\mu t}}{4}\Big[1 \\ & - p^2\cos(\gamma)\cos(2\rho_k)^2\left(\cos^2(2\varphi)+\cos(\delta)\sin^2(2\varphi)\right) \\ & - p^2\cos(\gamma)\cos(2\rho_k)\sin(2\rho_k)\left(1-\cos(\delta)\right)\sin(2\varphi)\cos(2\varphi) \\ & - p^2\cos(\gamma)\sin(2\rho_k)\cos(2\rho_k)\left(1-\cos(\delta)\right)\sin(2\varphi)\cos(2\varphi) \\ & - p^2\cos(\gamma)\sin(2\rho_k)^2\left(\sin^2(2\varphi)+\cos(\delta)\cos^2(2\varphi)\right) \\ & - p^2\sin(\gamma)\cos(2\rho_k)\sin(\delta)\sin(2\varphi) \\ & + p^2\sin(\gamma)\sin(2\rho_k)\sin(\delta)\cos(2\varphi)\Big]. \end{aligned}$$

By using the trigonometric identities

$$\begin{aligned} \sin(2\rho_k)^2 &= \frac{1}{2}\left(1-\cos(4\rho_k)\right), \\ \cos(2\rho_k)^2 &= \frac{1}{2}\left(1+\cos(4\rho_k)\right), \\ \sin(2\rho_k)\cos(2\rho_k) &= \frac{1}{2}\sin(4\rho_k), \end{aligned}$$

in ρ_k we obtain the formula:

$$\begin{aligned}\tilde{I}(\rho_k) =& \frac{I_0 e^{-\mu t}}{4}\Big[1 \\ &- p^2\cos(\gamma)\frac{1}{2}\left(1+\cos(4\rho_k)\right)\left(\cos^2(2\varphi)+\cos(\delta)\sin^2(2\varphi)\right) \\ &- p^2\cos(\gamma)\frac{1}{2}\sin(4\rho_k)\left(1-\cos(\delta)\right)\sin(2\varphi)\cos(2\varphi) \\ &- p^2\cos(\gamma)\frac{1}{2}\sin(4\rho_k)\left(1-\cos(\delta)\right)\sin(2\varphi)\cos(2\varphi) \\ &- p^2\cos(\gamma)\frac{1}{2}\left(1-\cos(4\rho_k)\right)\left(\sin^2(2\varphi)+\cos(\delta)\cos^2(2\varphi)\right) \\ &- p^2\sin(\gamma)\cos(2\rho_k)\sin(\delta)\sin(2\varphi) \\ &+ p^2\sin(\gamma)\sin(2\rho_k)\sin(\delta)\cos(2\varphi)\Big].\end{aligned}$$

Simplifying this equation yields

$$\begin{aligned}\tilde{I}(\rho_k) =& \frac{I_0 e^{-\mu t}}{4}\Big[1 - p^2\cos(\gamma)\frac{1}{2}\left(1+\cos(\delta)\right) \\ &- p^2\cos(\gamma)\frac{1}{2}\left(\cos(4\rho_k)\right)\left(1-\cos(\delta)\right)\left(\cos^2(2\varphi)-\sin^2(2\varphi)\right) \\ &- p^2\cos(\gamma)\sin(4\rho_k)\left(1-\cos(\delta)\right)\sin(2\varphi)\cos(2\varphi) \\ &- p^2\sin(\gamma)\cos(2\rho_k)\sin(\delta)\sin(2\varphi) \\ &+ p^2\sin(\gamma)\sin(2\rho_k)\sin(\delta)\cos(2\varphi)\Big].\end{aligned}$$

Using the trigonometric identities

$$\begin{aligned}\cos(2\varphi)^2-\sin(2\varphi)^2 &= \cos(4\varphi), \\ \sin(2\varphi)\cos(2\varphi) &= \frac{1}{2}\sin(4\varphi),\end{aligned}$$

the intensity profile can be rewritten as

$$\begin{aligned}\tilde{I}(\rho_k) =& \frac{I_0 e^{-\mu t}}{4}\Big[1 - p^2\cos(\gamma)\frac{1}{2}\left(1+\cos(\delta)\right) \\ &- p^2\cos(\gamma)\frac{1}{2}\left(\cos(4\rho_k)\right)\left(1-\cos(\delta)\right)\cos(4\varphi) \\ &- p^2\cos(\gamma)\frac{1}{2}\sin(4\rho_k)\left(1-\cos(\delta)\right)\sin(4\varphi) \\ &- p^2\sin(\gamma)\cos(2\rho_k)\sin(\delta)\sin(2\varphi) \\ &+ p^2\sin(\gamma)\sin(2\rho_k)\sin(\delta)\cos(2\varphi)\Big].\end{aligned}$$

A Fourier analysis on this profile yields the coefficients:

$$\begin{aligned}\tilde{a}_0 &= \frac{I_0 e^{-\mu t}}{4}\left(1-\frac{p^2\cos(\gamma)}{2}\left(1+\cos(\delta)\right)\right) \\ \tilde{a}_1 &= -\frac{I_0 e^{-\mu t}}{4}p^2\sin(\gamma)\sin(\delta)\sin(2\varphi) \\ \tilde{b}_1 &= \frac{I_0 e^{-\mu t}}{4}p^2\sin(\gamma)\sin(\delta)\cos(2\varphi) \\ \tilde{a}_2 &= -\frac{I_0 e^{-\mu t}}{8}p^2\cos(\gamma)(1-\cos(\delta))\sin(4\varphi) \\ \tilde{b}_2 &= -\frac{I_0 e^{-\mu t}}{8}p^2\cos(\gamma)(1-\cos(\delta))\cos(4\varphi).\end{aligned} \tag{A.8}$$

By analyzing these Fourier coefficients it is now possible to calculate the correct values of the retardation and the transmittance. For this purpose, the following terms are calculated first:

$$\begin{aligned}
&\sqrt{\tilde{a}_2^2 + \tilde{b}_2^2} \\
=&\sqrt{\left(-\frac{I_0 e^{-\mu t}}{8} p^2 \cos(\gamma)(1-\cos(\delta))\sin(4\varphi)\right)^2 + \left(-\frac{I_0 e^{-\mu t}}{8} p^2 \cos(\gamma)(1-\cos(\delta))\cos(4\varphi)\right)^2} \\
=&\frac{I_0 e^{-\mu t}}{8} p^2 \left|\cos(\gamma)\right| (1-\cos(\delta)),
\end{aligned}$$

with $(1-\cos(\delta)) \geq 0$ for all $\delta \in [0, \pi/2]$. Furthermore, we determine:

$$\begin{aligned}
\sqrt{\tilde{a}_1^2 + \tilde{b}_1^2} &= \sqrt{\left(-\frac{I_0 e^{-\mu t}}{4} p^2 \sin(\gamma)\sin(\delta)\sin(2\varphi)\right)^2 + \left(\frac{I_0 e^{-\mu t}}{4} p^2 \sin(\gamma)\sin(\delta)\cos(2\varphi)\right)^2} \\
&= \frac{I_0 e^{-\mu t}}{4} p^2 \left|\sin(\gamma)\right| \sin(\delta).
\end{aligned}$$

With the help of these expressions, the transmittance can be calculated by:

$$\begin{aligned}
&2\frac{\tilde{a}_0 - \operatorname{sign}(\cos(\gamma))\sqrt{\tilde{a}_2^2 + \tilde{b}_2^2}}{1 - p^2\cos(\gamma)} \\
=&2\frac{\frac{I_0 e^{-\mu t}}{4}\left(1 - \frac{p^2\cos(\gamma)}{2}(1+\cos(\delta))\right) - \frac{I_0 e^{-\mu t}}{8} p^2 \operatorname{sign}(\cos(\gamma))\left|\cos(\gamma)\right|(1-\cos(\delta))}{1 - p^2\cos(\gamma)} \\
=&2\frac{\frac{I_0 e^{-\mu t}}{4}\left(1 - \frac{p^2\cos(\gamma)}{2}(1+\cos(\delta))\right) - \frac{I_0 e^{-\mu t}}{4}\frac{p^2\cos(\gamma)}{2}(1-\cos(\delta))}{1 - p^2\cos(\gamma)} \\
=&2\frac{\frac{I_0 e^{-\mu t}}{4}\left(1 - \frac{p^2\cos(\gamma)}{2}(1+\cos(\delta)+1-\cos(\delta))\right)}{1 - p^2\cos(\gamma)} \\
=&2\frac{\frac{I_0 e^{-\mu t}}{4}\left(1 - p^2\cos(\gamma)\right)}{1 - p^2\cos(\gamma)} \\
=&\frac{I_0 e^{-\mu t}}{2} \\
=&I_T.
\end{aligned}$$

Once the transmittance is known, deriving the retardation is straight forward:

$$\frac{\sqrt{\tilde{a}_1^2 + \tilde{b}_1^2}}{\frac{I_T}{2}\left|\sin(\gamma)\right| p^2} = \frac{\frac{I_0 e^{-\mu t}}{4} p^2 \left|\sin(\gamma)\right| \sin(\delta)}{\frac{I_0 e^{-\mu t}}{4}\left|\sin(\gamma)\right| p^2} = \sin(\delta).$$

A.3 Proof of Bijectivity for $\alpha, t_{\mathbf{rel}} \rightarrow \sin(\delta), \partial \sin(\delta)/\partial\alpha$

We want to demonstrate that the transformation

$$f : \alpha, t_{\text{rel}} \rightarrow \sin(\delta), \frac{\partial \sin(\delta)}{\partial \alpha},$$

is bijective for $\alpha \in (-\pi/2, \pi/2)$ and $t_{\text{rel}} \in (0, 1]$, with

$$\delta = \frac{\pi}{2} t_{\text{rel}} \cos(\alpha)^2,$$

and the partial derivative

$$\frac{\partial \sin(\delta)}{\partial \alpha} = -\cos\left(\frac{\pi}{2} t_{\text{rel}} \cos(\alpha)^2\right) \pi \; t_{\text{rel}} \sin(\alpha)\cos(\alpha).$$

Proving surjectivity for the transformation f is trivial. For injectivity it must be proven that $f(\alpha_1, t_{\text{rel}1}) = f(\alpha_2, t_{\text{rel}2}) \Rightarrow \alpha_1, t_{\text{rel}1} = \alpha_2, t_{\text{rel}2}$:

$$f\begin{pmatrix}\alpha_1 \\ t_{\text{rel}1}\end{pmatrix} = f\begin{pmatrix}\alpha_2 \\ t_{\text{rel}2}\end{pmatrix}$$

$$\Rightarrow \begin{pmatrix} \sin\left(\frac{\pi}{2} t_{\text{rel}1} \cos(\alpha_1)^2\right) \\ -\cos\left(\frac{\pi}{2} t_{\text{rel}1} \cos(\alpha_1)^2\right) \pi \; t_{\text{rel}1} \sin(\alpha_1)\cos(\alpha_1) \end{pmatrix} = \begin{pmatrix} \sin\left(\frac{\pi}{2} t_{\text{rel}2} \cos(\alpha_2)^2\right) \\ -\cos\left(\frac{\pi}{2} t_{\text{rel}2} \cos(\alpha_2)^2\right) \pi \; t_{\text{rel}2} \sin(\alpha_2)\cos(\alpha_2) \end{pmatrix}.$$

For $\alpha \in (-\pi/2, \pi/2)$ and $t_{\text{rel}} \in (0, 1]$ it directly follows that $\delta \in (0, \pi/2]$. On this interval both the sin- and the cos-function are bijective. Hence, we can conclude that

$$\begin{aligned} \sin\left(\frac{\pi}{2} t_{\text{rel}1} \cos(\alpha_1)^2\right) &= \sin\left(\frac{\pi}{2} t_{\text{rel}2} \cos(\alpha_2)^2\right) \\ \Rightarrow -\cos\left(\frac{\pi}{2} t_{\text{rel}1} \cos(\alpha_1)^2\right) &= -\cos\left(\frac{\pi}{2} t_{\text{rel}2} \cos(\alpha_2)^2\right). \end{aligned}$$

With this information the previous equation can be simplified to

$$\begin{aligned} &\Rightarrow \begin{pmatrix} \frac{\pi}{2} t_{\text{rel}1} \cos(\alpha_1)^2 \\ \pi \; t_{\text{rel}1} \sin(\alpha_1)\cos(\alpha_1) \end{pmatrix} = \begin{pmatrix} \frac{\pi}{2} t_{\text{rel}2} \cos(\alpha_2)^2 \\ \pi \; t_{\text{rel}2} \sin(\alpha_2)\cos(\alpha_2) \end{pmatrix} \\ &\Rightarrow \begin{pmatrix} t_{\text{rel}1} \cos(\alpha_1)^2 \\ t_{\text{rel}1} \sin(\alpha_1)\cos(\alpha_1) \end{pmatrix} = \begin{pmatrix} t_{\text{rel}2} \cos(\alpha_2)^2 \\ t_{\text{rel}2} \sin(\alpha_2)\cos(\alpha_2) \end{pmatrix}. \end{aligned}$$

Dividing the second equation by the first equation, leads to

$$\begin{aligned} &\Rightarrow \tan(\alpha_1) = \tan(\alpha_2) \\ &\Rightarrow \alpha_1 = \alpha_2 \quad \forall \alpha_1, \alpha_2 \in \left(-\frac{\pi}{2}, \frac{\pi}{2}\right). \end{aligned}$$

Inserting this result into one of the previous equations directly implies

$$\begin{aligned} &\Rightarrow t_{\text{rel}1} \cos(\alpha_1)^2 = t_{\text{rel}2} \cos(\alpha_1)^2 \\ &\Rightarrow t_{\text{rel}1} = t_{\text{rel}2}. \end{aligned}$$

Hence, the transformation f is bijective and can be inverted.

A.4 Transformation between Tilting Coordinate Systems.

In Sec. 4.3.1, two different coordinate systems were used to describe the position of the tiltable specimen stage. The first one is based on the experimental setup, with a rotation around the y-axis followed by one around the x-axis:

$$\begin{aligned}\mathbf{R}(\tau_x,\tau_y) &= \begin{pmatrix}1 & 0 & 0\\ 0 & \cos(\tau_x) & -\sin(\tau_x)\\ 0 & \sin(\tau_x) & \cos(\tau_x)\end{pmatrix}\cdot\begin{pmatrix}\cos(\tau_y) & 0 & \sin(\tau_y)\\ 0 & 1 & 0\\ -\sin(\tau_y) & 0 & \cos(\tau_y)\end{pmatrix}\\ &= \begin{pmatrix}\cos(\tau_y) & 0 & \sin(\tau_y)\\ \sin(\tau_x)\sin(\tau_y) & \cos(\tau_x) & -\sin(\tau_x)\cos(\tau_y)\\ -\cos(\tau_x)\sin(\tau_y) & \sin(\tau_x) & \cos(\tau_x)\cos(\tau_y)\end{pmatrix}.\end{aligned}$$

However, for theoretical calculations the following description is more useful:

$$\begin{aligned}\mathbf{R}(\psi,\tau) &= \mathbf{R}^z(\psi)\mathbf{R}^y(\tau)\mathbf{R}^z(-\psi)\\ &= \begin{pmatrix}\cos(\psi) & -\sin(\psi) & 0\\ \sin(\psi) & \cos(\psi) & 0\\ 0 & 0 & 1\end{pmatrix}\cdot\begin{pmatrix}\cos(\tau) & 0 & \sin(\tau)\\ 0 & 1 & 0\\ -\sin(\tau) & 0 & \cos(\tau)\end{pmatrix}\cdot\begin{pmatrix}\cos(\psi) & \sin(\psi) & 0\\ -\sin(\psi) & \cos(\psi) & 0\\ 0 & 0 & 1\end{pmatrix}\\ &= \begin{pmatrix}\cos(\tau)\cos(\psi)^2+\sin(\psi)^2 & (\cos(\tau)-1)\sin(\psi)\cos(\psi) & \cos(\psi)\sin(\tau)\\ (\cos(\tau)-1)\sin(\psi)\cos(\psi) & \cos(\tau)\sin(\psi)^2+\cos(\psi)^2 & \sin(\psi)\sin(\tau)\\ -\cos(\psi)\sin(\tau) & -\sin(\psi)\sin(\tau) & \cos(\tau)\end{pmatrix}.\end{aligned}$$

Hence, we need to find a parameter set (τ_x,τ_y) for every (τ,ψ) so that both expression equate to the same rotation matrix, i.e.

$$\mathbf{R}(\psi,\tau)=\mathbf{R}(\tau_x,\tau_y).$$

Comparing the first row of these matrices yields

$$(\cos(\tau)-1)\sin(\psi)\cos(\psi)=0,$$

which is obviously is not valid for arbitrary values of ψ and τ. It was argued in Sec. 4.3.1 that it is sufficient if the third row of both matrices is equal. Comparing the third row yields the three equations

$$\begin{aligned}-\cos(\psi)\sin(\tau) &= -\cos(\tau_x)\sin(\tau_y),\\ -\sin(\psi)\sin(\tau) &= \sin(\tau_x),\\ \cos(\tau) &= \cos(\tau_x)\cos(\tau_y).\end{aligned}$$

In order to find a solution, the approach

$$\begin{aligned}\tau_x &= -\arcsin(\sin(\tau)\sin(\psi)),\\ \tau_y &= \arctan(\tan(\tau)\cos(\psi)),\end{aligned}\tag{A.9}$$

is used in combination with the trigonometric identities

$$\sin(\arctan(x))=\frac{x}{\sqrt{1+x^2}}\qquad\text{and}\qquad\cos(\arctan(x))=\frac{1}{\sqrt{1+x^2}}.$$

This approach yields

$$\begin{aligned}
-\cos(\tau_x)\sin(\tau_y) &= -\cos(-\arcsin(\sin(\tau)\sin(\psi)))\sin(\arctan(\tan(\tau)\cos(\psi))) \\
&= -\sqrt{1-\sin(-\arcsin(\sin(\tau)\sin(\psi)))^2}\frac{\tan(\tau)\cos(\psi)}{\sqrt{1+\tan(\tau)^2\cos(\psi)^2}} \\
&= -\sqrt{1-\sin(\tau)^2\sin(\psi)^2}\frac{\sin(\tau)\cos(\psi)}{\cos(\tau)\sqrt{1+\tan(\tau)^2\cos(\psi)^2}} \\
&= -\frac{\sqrt{1-\sin(\tau)^2\sin(\psi)^2}}{\sqrt{\cos(\tau)^2+\sin(\tau)^2\cos(\psi)^2}}\ \sin(\tau)\cos(\psi) \\
&= -\frac{\sqrt{1-\sin(\tau)^2\sin(\psi)^2}}{\sqrt{1-\sin(\tau)^2+\sin(\tau)^2(1-\sin(\psi)^2)}}\ \sin(\tau)\cos(\psi) \\
&= -\frac{\sqrt{1-\sin(\tau)^2\sin(\psi)^2}}{\sqrt{1-\sin(\tau)^2\sin(\psi)^2}}\ \sin(\tau)\cos(\psi) \\
&= -\sin(\tau)\cos(\psi),
\end{aligned}$$

for the first equation. The second equation can be validated by

$$\begin{aligned}
\sin(\tau_x) &= \sin(-\arcsin(\sin(\tau)\sin(\psi))) \\
&= -\sin(\tau)\sin(\psi),
\end{aligned}$$

and the third equation can be confirmed as well:

$$\begin{aligned}
\cos(\tau_x)\cos(\tau_y) &= \cos(-\arcsin(\sin(\tau)\sin(\psi)))\cos(\arctan(\tan(\tau)\cos(\psi))) \\
&= \sqrt{1-\sin(-\arcsin(\sin(\tau)\sin(\psi)))^2}\frac{1}{\sqrt{1+\tan(\tau)^2\cos(\psi)^2}} \\
&= \sqrt{1-\sin(\tau)^2\sin(\psi)^2}\frac{\cos(\tau)}{\cos(\tau)\sqrt{1+\tan(\tau)^2\cos(\psi)^2}} \\
&= \cos(\tau)\frac{\sqrt{1-\sin(\tau)^2\sin(\psi)^2}}{\sqrt{\cos(\tau)^2+\sin(\tau)^2\cos(\psi)^2}} \\
&= \cos(\tau)\frac{\sqrt{1-\sin(\tau)^2\sin(\psi)^2}}{\sqrt{1-\sin(\tau)^2+\sin(\tau)^2(1-\sin(\psi)^2)}} \\
&= \cos(\tau)\frac{\sqrt{1-\sin(\tau)^2\sin(\psi)^2}}{\sqrt{1-\sin(\tau)^2\sin(\psi)^2}} \\
&= \cos(\tau).
\end{aligned}$$

Hence, Eq. (A.9) is a valid transformation, in order to achieve an identical z-component for both coordinate systems.

A.5 The Derivation of the Phase Retardance Signal and Its Analysis

Tilting the sample by an angle τ in the tilting direction ψ_i results in a three dimensional rotation of the fiber orientation vector according to

$$\mathbf{x}_i = \mathbf{R}^z(\psi_i)\mathbf{R}^y(\tau)\mathbf{R}^z(-\psi_i)\mathbf{x_0}.$$

By considering the vectors $\mathbf{x}_0$ and $\mathbf{x}_i$ in spherical coordinates we obtain:

$$\begin{pmatrix}\cos(\alpha_i)\cos(\varphi_i)\\ \cos(\alpha_i)\sin(\varphi_i)\\ \sin(\alpha_i)\end{pmatrix} = \begin{pmatrix}\cos(\tau)\cos(\psi)^2+\sin(\psi)^2 & (\cos(\tau)-1)\sin(\psi)\cos(\psi) & \cos(\psi)\sin(\tau)\\ (\cos(\tau)-1)\sin(\psi)\cos(\psi) & \cos(\tau)\sin(\psi)^2+\cos(\psi)^2 & \sin(\psi)\sin(\tau)\\ -\cos(\psi)\sin(\tau) & -\sin(\psi)\sin(\tau) & \cos(\tau)\end{pmatrix}\cdot\begin{pmatrix}\cos(\alpha_0)\cos(\varphi_0)\\ \cos(\alpha_0)\sin(\varphi_0)\\ \sin(\alpha_0)\end{pmatrix}.$$

Hence, the z-component of the rotated vector $\mathbf{x_i}$ is given by

$$\begin{aligned}\sin(\alpha_i) &= -\cos(\psi)\sin(\tau)\cos(\alpha_0)\cos(\varphi_0) - \sin(\psi)\sin(\tau)\cos(\alpha_0)\sin(\varphi_0) + \cos(\tau)\sin(\alpha_0)\\ &= \cos(\tau)\sin(\alpha_0) - \sin(\tau)\cos(\alpha_0)\cos(\psi_i-\varphi_0).\end{aligned}$$

This result can be used to calculate the phase retardance of a tilted measurement:

$$\begin{aligned}\delta_i =& \frac{\pi}{2}t_{\text{rel}}\cos(\alpha_i)^2\\ =& \frac{\pi}{2}t_{\text{rel}}(1-\sin(\alpha_i)^2)\\ =& \frac{\pi}{2}t_{\text{rel}}\big\{1-(\cos(\tau)\sin(\alpha_0)-\sin(\tau)\cos(\alpha_0)\cos(\psi_i-\varphi_0))^2\big\}\\ =& \frac{\pi}{2}t_{\text{rel}}\Big\{1-\cos(\tau)^2\sin(\alpha_0)^2+2\cos(\tau)\sin(\alpha_0)\sin(\tau)\cos(\alpha_0)\cos(\psi_i-\varphi_0)\\ &-\sin(\tau)^2\cos(\alpha_0)^2\cos(\psi_i-\varphi_0)^2\Big\}\\ =& \frac{\pi}{2}t_{\text{rel}}\Big\{1-\cos(\tau)^2\sin(\alpha_0)^2\\ &+2\cos(\tau)\sin(\alpha_0)\sin(\tau)\cos(\alpha_0)[\cos(\psi_i)\cos(\varphi_0)+\sin(\psi_i)\sin(\varphi_0)]\\ &-\sin(\tau)^2\cos(\alpha_0)^2\frac{1}{2}[1+\cos(2\psi_i-2\varphi_0)]\Big\}\\ =& \frac{\pi}{2}t_{\text{rel}}\left\{1-\cos(\tau)^2\sin(\alpha_0)^2-\frac{1}{2}\sin(\tau)^2\cos(\alpha_0)^2\right.\\ &+2\cos(\tau)\sin(\alpha_0)\sin(\tau)\cos(\alpha_0)[\cos(\psi_i)\cos(\varphi_0)+\sin(\psi_i)\sin(\varphi_0)]\\ &\left.-\frac{1}{2}\sin(\tau)^2\cos(\alpha_0)^2[\cos(2\psi_i)\cos(2\varphi_0)+\sin(2\psi_i)\sin(2\varphi_0)]\right\}.\end{aligned}$$

The first order Fourier coefficients of this signal are:

$$\begin{aligned}a_{\delta,1} =& \frac{2}{N}\sum_{i=1}^{N_t}\delta_i\cos(\psi_i) = \pi t_{\text{rel}}\sin(\tau)\cos(\tau)\sin(\alpha_0)\cos(\alpha_0)\cos(\varphi_0),\\ b_{\delta,1} =& \frac{2}{N}\sum_{i=1}^{N_t}\delta_i\sin(\psi_i) = \pi t_{\text{rel}}\sin(\tau)\cos(\tau)\sin(\alpha_0)\cos(\alpha_0)\sin(\varphi_0).\end{aligned}$$

A.6 Error Propagation of Detection Noise

In this section, it is demonstrated how the detection noise specified by $\sigma_{I_{k,i}} = \sqrt{gI_{k,i}}$ propagates to the measurand

$$A_i = \frac{a_{1,i}}{a_{0,i}} = \frac{2}{N}\frac{1}{\frac{1}{N}\sum\limits_k I_{k,i}}\sum_k I_{k,i}\cos(2\rho_k).$$

In the following calculations these formulas are used:

$$\begin{aligned} I_{k,i} &= \frac{I_{T,i}}{2}\left(1+\sin(\delta_i)\sin(2\rho_k - 2\varphi_i)\right) \\ I_{T,i} &= 2a_0 = \frac{2}{N}\sum_k I_{k,i} \\ \cos(2\rho_k)^2 &= \frac{1}{2}\left(1+\cos(4\rho_k)\right) \\ \sum_k I_{k,i}\cos(4\rho_k) &= 0. \end{aligned} \tag{A.10}$$

For the Gaussian error propagation, the derivative $\partial_{I_{k,i}} A_i$ needs to be calculated:

$$\begin{aligned} \partial_{I_{k,i}} A_i =& \frac{2}{N}\frac{\cos(2\rho_k)\frac{1}{N}\sum\limits_k I_{k,i} - \frac{1}{N}\sum\limits_k I_{k,i}\cos(2\rho_k)}{\left(\frac{1}{N}\sum\limits_k I_{k,i}\right)^2} \\ =& \frac{2}{N}\frac{\cos(2\rho_k) - \frac{1}{2}A_i}{\frac{1}{N}\sum\limits_k I_{k,i}} \\ =& \frac{4}{N}\frac{\cos(2\rho_k) - \frac{1}{2}A_i}{I_{T,i}} \end{aligned}$$

with this intermediate step, the error of the measurand can be calculated:

$$\begin{aligned} \sigma_{A_i} =& \sqrt{\sum_k \left(\partial_{I_{k,i}} A_i \ \sigma_{I_{k,i}}\right)^2} \\ =& \sqrt{\sum_k \left(\frac{4}{N}\frac{\cos(2\rho_k) - \frac{1}{2}A_i}{I_{T,i}}\right)^2 gI_{k,i}} \\ =& \sqrt{\frac{4\,g}{N\,I_{T,i}}\sum_k \frac{4}{N}\frac{\left(\cos(2\rho_k) - \frac{1}{2}A_i\right)^2}{I_{T,i}} I_{k,i}} \\ =& \sqrt{\frac{4\,g}{N\,I_{T,i}}\sum_k \frac{4}{N}\frac{\cos(2\rho_k)^2 - \cos(2\rho_k)A_i + \frac{1}{4}A_i^2}{I_{T,i}} I_{k,i}} \end{aligned}$$

By using Eq. (A.10) this term can be simplified further:

$$
\begin{aligned}
&= \sqrt{\frac{4\,g}{N\,I_{T,i}} \sum_k \frac{4}{N} \frac{\frac{1}{2}(1+\cos(4\rho_k)) - \cos(2\rho_k)A_i + \frac{1}{4}A_i^2}{I_{T,i}} I_{k,i}} \\
&= \sqrt{\frac{4\,g}{N\,I_{T,i}} \frac{I_{T,i} - 2a_{1,i}A_i + \frac{1}{2}A_i^2 I_{T,i}}{I_{T,i}}} \\
&= \sqrt{\frac{4\,g}{N\,I_{T,i}} \left(1 - A_i^2 + \frac{1}{2}A_i^2\right)} \\
&= \sqrt{\frac{4\,g}{N\,I_{T,i}} \left(1 - \frac{1}{2}A_i^2\right)}
\end{aligned}
$$

Appendix B

Complementary Data

B.1 A Direct Comparison between the LOriE and the DFT-based Algorithm

The dataset in Sec. 4.3.3 has been reexamined with the LOriE algorithm. In Fig. B.2, Fig. B.3 and Fig. B.4 a direct comparison between the results of the DFT-based algorithm and the LOriE algorithm is presented. Significant differences in the results are not observable. Only in Fig. B.4, the vector field reconstructed by the LOriE algorithm seems to fit slightly better with the course of the bundle.

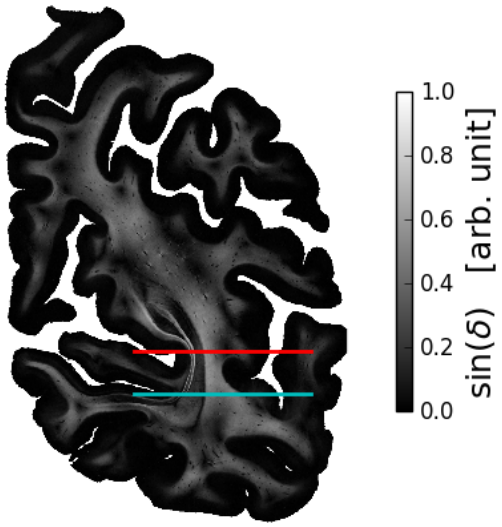

FIGURE B.1: Overview of the analyzed hemisphere. The colored lines indicate the position of the resliced views in Fig. B.2 and Fig. B.4.

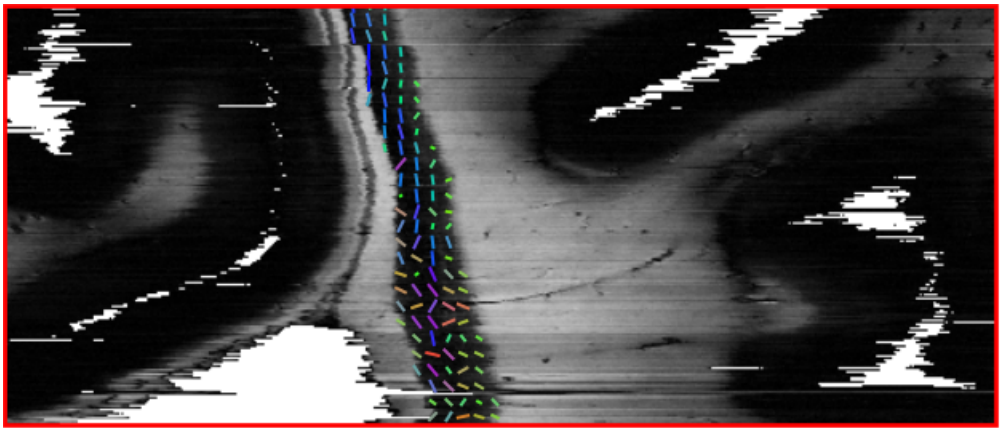

(a) DFT-based algorithm

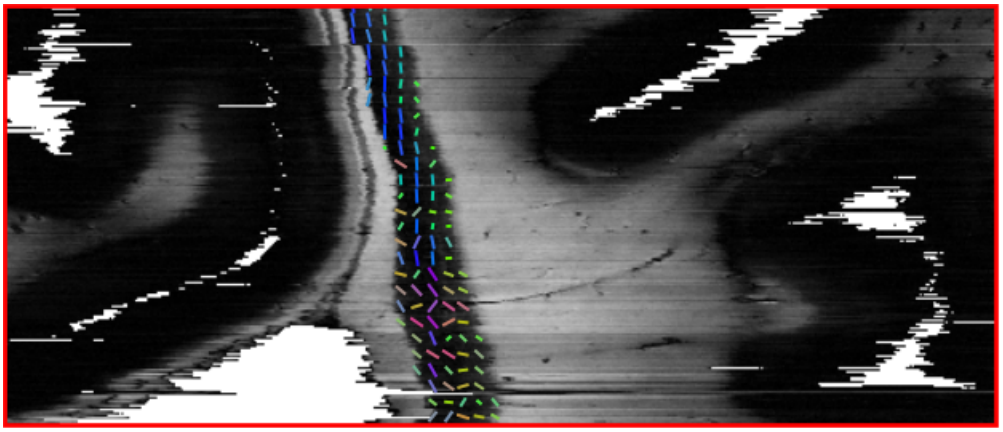

(b) LOriE algorithm

FIGURE B.2: Resliced view of Fig. B.1 (red line) featuring the vector field in the sagittal stratum of a fiber bundle inclined by approximately 90° (every 8th vector is plotted).

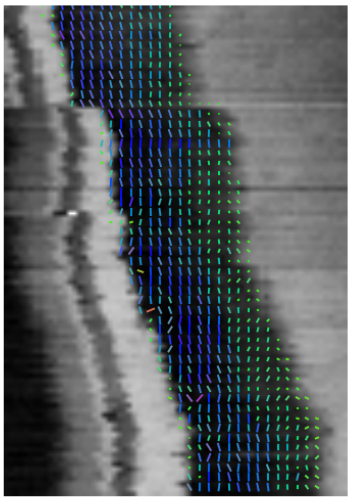

(a) DFT-based algorithm

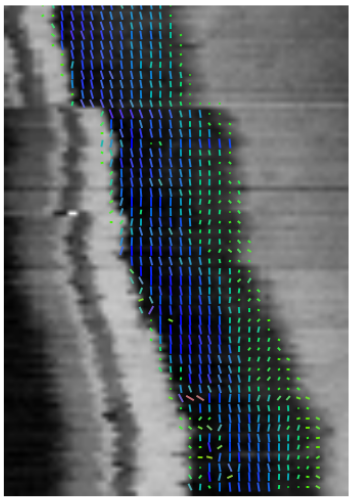

(b) LORIE algorithm.

FIGURE B.3: Zooms of the vector fields in Fig. B.2a and Fig. B.2b.

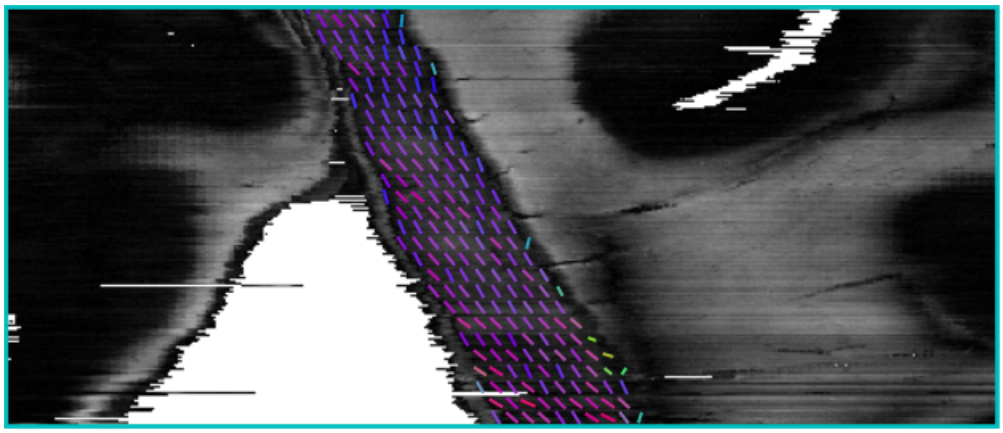

(a) DFT-based algorithm

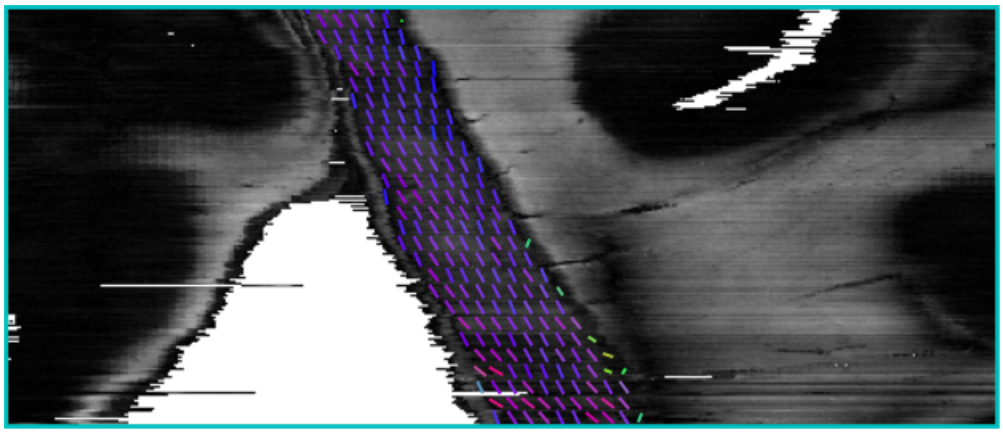

(b) LOriE

FIGURE B.4: Resliced view of Fig. B.1 (red line) featuring the vector field in the sagittal stratum of a fiber bundle inclined by approximately 60° (every 8th vector is plotted).

B.2 Angular Spectrum of the Diffuser

In Sec. 5.4.3 a simulation was performed to assess the influence of different diffusers. The angular spectrum for each diffuser was modeled to resemble the characteristics provided by the manufacturer, which is shown in Fig. B.5.

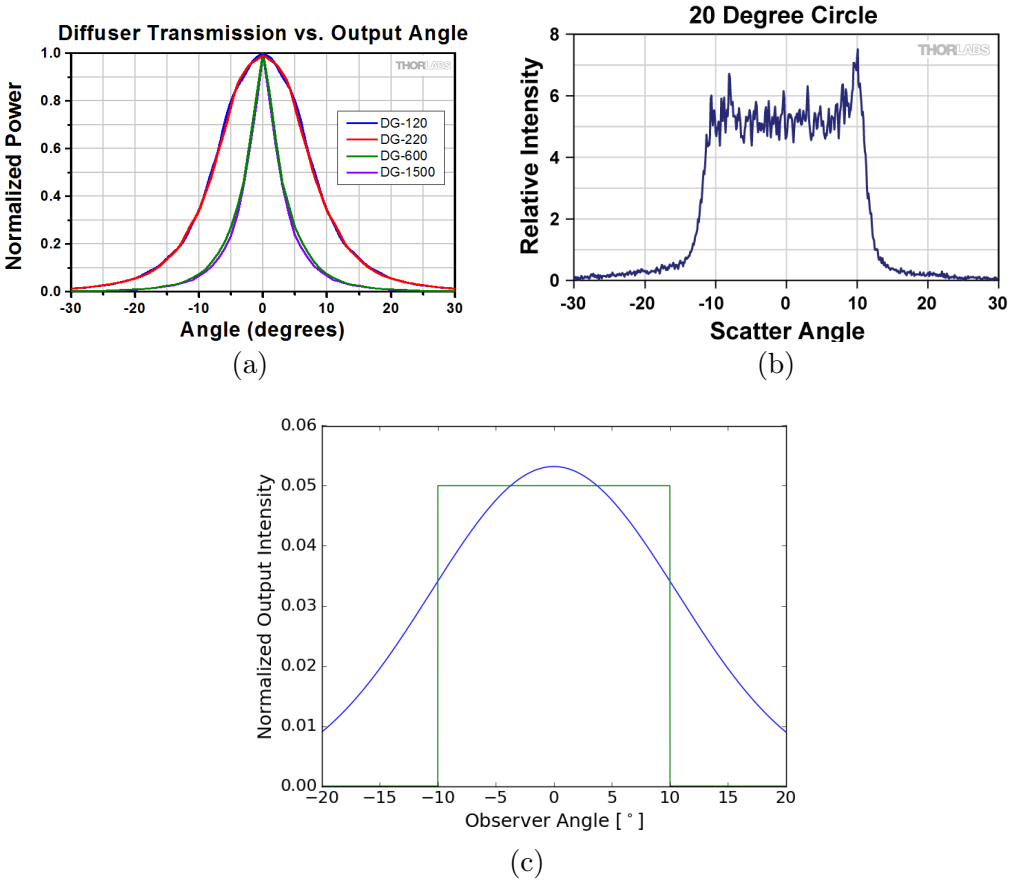

FIGURE B.5: The angular spectra of standard issue ground glass diffusers (*Thorlabs* DG10-600) in (a) and an engineered diffuser (*Thorlabs* ED1-C20) in (b) were provided by Thorlabs. (c) shows the respective source models that were used in the simulation in order to emulate the diffuser.

B.3 Shape of the Condenser Lens

In Fig. B.6 the influence of the shape of the condenser lens is studied. When using an aspheric condenser lens, the specimen is illuminated evenly by both central rays and oblique rays. When a spherical condenser lens is employed, the central rays are still parallel and illuminate the specimen in a uniform manner. The oblique rays on the other hand are slightly focused, causing the size of the illuminated spot to be reduced and the uniformity to decrease. Due to the longer focal length ($f = 60\,\mathrm{mm}$ instead of $f = 32\,\mathrm{mm}$) the oblique angle is reduced as well. When aiming to achieve the same oblique angle as for the aspheric lens (i.e. $\tau = 5.7°$), the quality of the oblique illumination is reduced even further.

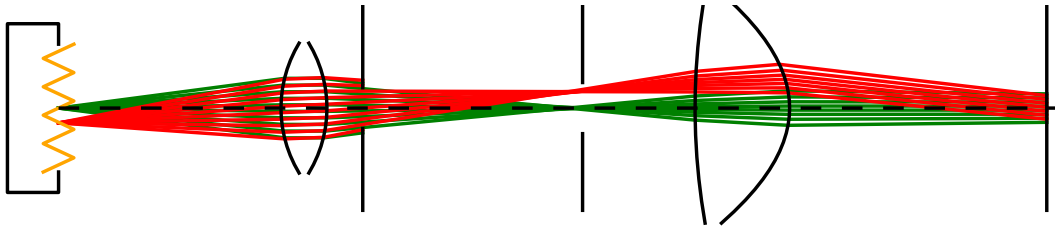

(a)

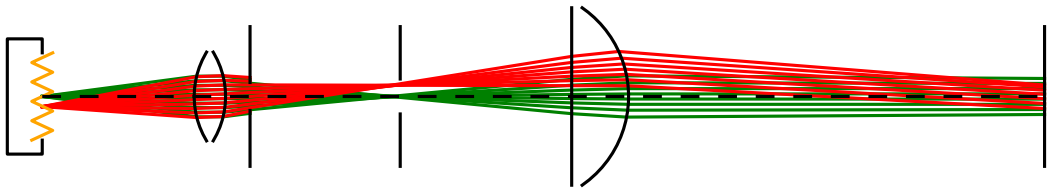

(b)

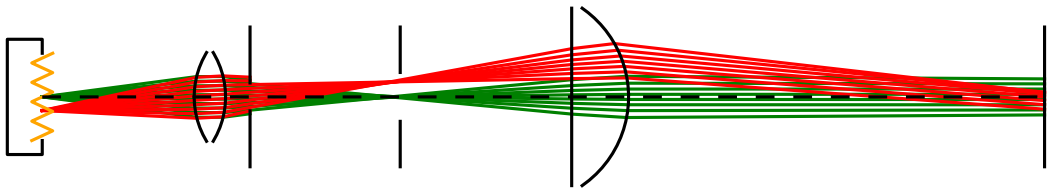

(c)

FIGURE B.6: Simulation of the experimental setup for different condenser lenses. (a) features the simulation for an aspheric condenser lens (*Thorlabs* ACL4532-A). In (b) a spherical plano convex condenser lens (*Thorlabs* LA1401-A) was used instead. Due to the different lens shape the oblique angle is reduced to $\tau \approx 4°$ when the same set-up is considered. (c) features the same condenser lens as (b), but the oblique angle now matches the one achieved for the aspheric condenser lens.

B.4 Influence of the Resolution

When scaling down the data that was recorded with the new microscope, the distribution of the reconstructed inclinations converges towards the one determined in the LAP (as it has been observed for the LOriE algorithm in Sec. 5.5).

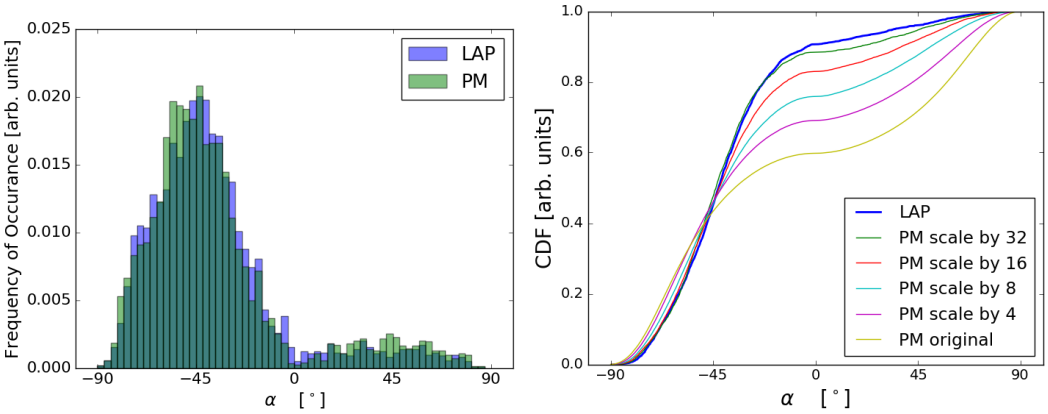

(a) (b)

FIGURE B.7: Analysis of the distribution of inclinations that were calculated by the DFT-based algorithm. The distribution of inclinations derived on the bases of the downscaled data of the oblique illumination system resembles the distribution that is based on the data acquired with the tiltable specimen stage in the LAP (a). The CDFs in (b) show that the original distribution of inclinations derived from the microscopic data converges to the CDF of inclinations in the LAP.

List of Symbols

Symbol	Explanation
$\mathbf{E}(z, \tilde{t})$	electric field vector
$\mathbf{E}_0$	Jones vector
E_{0x}, E_{0y}	components of the Jones vector
k	wavenumber
z	z-coordinate
ω	angular frequency of a wave
$\tilde{t}$	time parameter
$\mathbf{S}$	Stokes vector
S_0, S_1, S_2, S_3	components of the Stokes vector
p	degree of polarization
I	intensity
I_0	initial intensity
$\mathbf{M}$	an arbitrary Mueller matrix
$\mathbf{M}_{\text{pol}}(p_x, p_y)$	Mueller matrix of a polarizing element, with p_x and p_y as the polarization efficiency in the respective directions
$\mathbf{M}_{\text{wp}}(\delta)$	Mueller matrix of a retarder with retardance δ
$\mathbf{M}_{\text{rot}}(\theta)$	Mueller matrix of a rotator at an angle θ
$\mathbf{M}(\theta)$	the rotated version of an arbitrary Mueller matrix
$\mathbf{M}_{\text{wp}}(\delta, \theta)$	Mueller matrix of a rotated retarder
$\mathbf{M}_{\text{pol},x}(\theta)$	Mueller matrix of an ideal polarizer
$\mathbf{M}_{\text{pol},x}(p, \theta)$	Mueller matrix of a non-ideal polarizer
$\mathbf{S}_{\text{source}}$	Stokes vector of the light source
$\mathbf{S}_{\text{PSG}}$	Stokes vector of the polarization state generator
$\mathbf{M}_{\text{PSG}}$	Mueller matrix of the polarization state generator
$\mathbf{S}^{\dagger}_{\text{PSA}}$	Stokes vector of the polarization state analyzer
$\mathbf{M}_{\text{PSA}}$	Mueller matrix of the polarization state analyzer
I_k	intensity of the k-th measurement defined by the respective states $\mathbf{S}^{\dagger}_{\text{PSA},k}$ and $\mathbf{S}_{\text{PSG},k}$
$\mathbf{M}_{\text{sample}}$	Mueller matrix of an arbitrary sample
n_x, n_y, n_z	main axes of a refractive index ellipsoid of a birefringent material
n_o, n_E	main axes of a uniaxial index ellipsoid
$n_e(\alpha)$, n_e	both symbols represent the refractive index for the extraordinary wave (the second notation is the short form)
$\mathbf{E_o}$, $\mathbf{E_e}$	the components of the Jones vector split up into ordinary and extraordinary wave

Abbreviations	Explanation
$\mathbf{x}$	orientation vector of the indicatrix, therefore also denotes the presumed fiber orientation within a voxel
t	thickness of the birefringent sample
λ	wavelength of the light
Δn	birefringence
α	inclination angle of the fiber (or the respective indicatrix)
φ	in-plane direction angle of the fiber (or the respective indicatrix)
μ	attenuation coefficient of the sample
ρ_k	rotation angle of the polarization filters
δ	phase retardance
$\sin(\delta)$	retardation
t_{rel}	relative thickness
I_T	transmittance
$\mathbf{S}_{\text{PSG}_{\text{LAP}}}$, $\mathbf{S}^{\dagger}_{\text{PSA}_{\text{LAP}}}$	Stokes vectors of the PSA and PSG for the LAP
$\mathbf{S}_{\text{PSG}_{\text{PM}}}$, $\mathbf{S}^{\dagger}_{\text{PSA}_{\text{PM}}}$	Stokes vectors of the PSA and PSG for the PM
a_0, a_1, b_1	Fourier coefficients of the measured intensity profile in a standard measurement
λ_{ret}	specified wavelength of the retarder
λ_{source}	wavelength of the source
γ	actual phase retardance of the waveplate
$\tilde{\mathbf{S}}_{PSG_{LAP}}$, $\tilde{\mathbf{S}}^{\dagger}_{PSA_{LAP}}$	Stokes vectors of the PSA and PSG for the LAP, considering non-ideal polarization filters
$\tilde{I}(\rho_k)$	intensity profile for non-ideal polarization filters
$\tilde{a}_0$, $\tilde{a}_1$, $\tilde{b}_1$, $\tilde{a}_2$, $\tilde{b}_2$	Fourier coefficients of the signal $\tilde{I}(\rho_k)$
$I^p(\rho_k)$	intensity profile for two linear polarizers
a_1^p, a_0^p	Fourier coefficients of the signal $I^p(\rho_k)$
n_{sample}	refractive index of the specimen
τ	angle of the tiltable specimen stage
τ_{ext}	externally applied tilting angle
τ_{int}	tilting angle within the tissue
$\mathbf{R}$	rotation matrix that describes the tilting
$\mathbf{x}_0$, $\mathbf{x}_i$	orientation vector for the planar and tilted positions of the specimen stage
α_0, α_i	inclination angle for the planar and tilted positions of the specimen stage
φ_0, φ_i	direction angle for the planar and tilted positions of the specimen stage
δ_0, δ_i	phase retardance for the planar and tilted positions of the specimen stage
ψ_i	tilting direction
$a_{\delta,1}$, $b_{\delta,1}$	Fourier coefficients of the phase retardance signal
β	acute angle between two orientation vectors
$\bar{\beta}$	average acute angle between two orientation vectors across severel measurements

Abbreviations	Explanation
$\bar{I}$	sample mean
S^2	sample variance
σ	standard deviation
A_i, B_i	normalized Fourier coefficients
$\langle A_i \rangle$, $\langle B_i \rangle$	expectation values of A_i, B_i
σ_{A_i}, σ_{B_i}	standard deviation of A_i, B_i
P	probability
$\tilde{\alpha}$, $\tilde{\varphi}$, $\tilde{t}_{\mathrm{rel}}$	unbounded versions of α, φ and t_{rel}
d_{xy}	in-plane resolution
d_{tot}	total depth of field
NA_{obj}	numerical aperture of the objective lens
M	magnification of the imaging system
D	clear aperture of a lens
n	refractive index of the lens material
$z(r)$	function describing the lens curvature
κ	conic constant
NA_{illu}	numerical aperture of the illumination system
τ_{max}	maximal possible oblique angle
f	focal length of a lens
h_o	size of an object that is imaged
h_i	size of an image created by a lens
d_o	distance between object and lens
d_i	distance between image and lens
d_{apt}, r_{apt}	diameter and radius of the aperture diaphragm
r_d	radial offset of the aperture diaphragm
Δ	distance between collector lens and field diaphragm

List of Abbreviations

Abbreviations	Explanation
3D-PLI	Three Dimensional Polarized Light Imaging
ABC	Abstract Base Class
BOLD	Blood Oxygen Level Dependent
cc	corpus callosum
CCD	Charge-Coupled Device
CDF	Cumulative Distribution Function
CPu	caudate-putanem
DFT	Discrete Fourier Transform
dMRI	diffusion MRI
DMSO	Dimethyl sulfoxide
DTI	Diffusion Tensor Imaging
ec	external capsule
fMRI	functional MRI
FOM	Fiber Orientation Map
HARDI	High Angular Resolution Diffusion Imaging
LAP	Large Area Polarimeter
LED	Light Emitting Diode
LOriE	Likelihood Orientation Estimation
MRI	Magnetic Resonance Imaging
ODF	Orientation Distribution Function
pliODF	polarized light imaging ODF
PM	Polarizing Microscope
PSA	Polarization State Analyzer
PSG	Polarization State Generator
RGB	Red Green Blue
ROI	Region of Interest
SNR	Signal Noise Ratio
UML	Unified Modeling Language

List of Figures

List of Tables

References

[1] Figure of a neuron published under creative commons, attribution unknown. [https://commons.wikimedia.org/wiki/File%3ANeuron_(deutsch)-1.svg; accessed 2016-05-18].

[2] Human brain project - report, 2013. https://www.humanbrainproject.eu/.

[3] Katrin Amunts, Claude Lepage, Louis Borgeat, Hartmut Mohlberg, Timo Dickscheid, Marc-Etienne Rousseau, Sebastian Bludau, Pierre-Louis Bazin, Lindsay B. Lewis, Ana-Maria Oros-Peusquens, Nadim J. Shah, Thomas Lippert, Karl Zilles, and Alan C. Evans. BigBrain: An Ultrahigh-Resolution 3D Human Brain Model. *SCIENCE*, 340(6139):1472–1475, JUN 21 2013.

[4] M. Axer, K. Amunts, D. Graessel, C. Palm, J. Dammers, H. Axer, U. Pietrzyk, and K. Zilles. A novel approach to the human connectome: Ultra-high resolution mapping of fiber tracts in the brain. *NeuroImage*, 54(2):1091–1101, 2011.

[5] M. Axer, D. Graessel, M. Kleiner, J. Dammers, T. Dickscheid, J. Reckfort, T. Huetz, B. Eiben, U. Pietrzyk, K. Zilles, and K. Amunts. High-resolution fiber tract reconstruction in the human brain bymeans of three-dimensional polarized light imaging. *Frontiers in NEUROINFORMATICS*, 5(34):1–13, 2011.

[6] Markus Axer, Sven Strohmer, David Graessel, Oliver Buecker, Melanie Dohmen, Julia Reckfort, Karl Zilles, and Katrin Amunts. Estimating Fiber Orientation Distribution Functions in 3D-Polarized Light Imaging. *FRONTIERS IN NEUROANATOMY*, 10, APR 19 2016.

[7] H. Bay, A. Ess, T. Tuytelaars, and L. Van Gool. Speeded-Up Robust Features (SURF). *Computer Vision and Image Understanding*, 110(3):346–359, 2008.

[8] R.S. Bear and F.O. Schmitt. The optics of nerve myelin. *J.O.S.A.*, 26:206–212, 1936.

[9] M. Born and E. Wolf. *Principles of Optics - Electromagnetic Theory of Propagation, Interference and Diffraction of light.* Cambridge University Press, 7th expanded edition, 1999.

[10] Matthew D. Budde and Joseph A. Frank. Examining brain microstructure using structure tensor analysis of histological sections. *Neuroimage*, 63:1–10, 2012.

[11] G. Casella and R.L. Berger. *Statistical Inference.* Duxbury advanced series in statistics and decision sciences. Thomson Learning, 2 edition, 2002.

[12] P Chinn and FO Schmitt. On the birefringence of nerve sheaths as studied in cross sections. *JOURNAL OF CELLULAR AND COMPARATIVE PHYSIOLOGY*, 9(2):289–296, FEB 1937.

[13] Russel A. Chipman. *Handbook of Optics - Volume II - Devices, Measurements, Properties*, volume 2, chapter 15.23 Dual rotating retarder polarimeter, pages 22.1–22.38. The McGraw-Hill companies, 2 edition, 1995.

[14] Kwanghun Chung, Jenelle Wallace, Sung-Yon Kim, Sandhiya Kalyanasundaram, Aaron S. Andalman, Thomas J. Davidson, Julie J. Mirzabekov, Kelly A. Zalocusky, Joanna Mattis, Aleksandra K. Denisin, Sally Pak, Hannah Bernstein, Charu Ramakrishnan, Logan Grosenick, Viviana Gradinaru, and Karl Deisseroth. Structural and molecular interrogation of intact biological systems. *NATURE*, 497(7449):332+, MAY 16 2013.

[15] E. Collett. *Field Guide to Polarization*, volume FG05. SPIE Press, September 2005.

[16] J. Dammers, M. Axer, D. Graessel, C. Palm, K. Zilles, K. Amunts, and U. Pietrzyk. Signal enhancement in polarized light imaging by means of independent component analysis. *NeuroImage*, 49(2):1241–1248, 2010.

[17] B. De Campos Vidal, M.L. Silveira Mello, A.C. Caseiro-Filho, and C. Godo. Anisotropic properties of the myelin sheath. *Acta Histochemica*, 66(1):32–39, 1980. cited By 17.

[18] Benedicto de Campos Vidal, Maria Luiza Silveira Mello, Alberto Costa Caseiro-Filho, and Carlos Godo. Anisotropic properties of the myelin sheath. *Acata histochem.*, 66:32–39, 1980.

[19] Melanie Dohmen, Miriam Menzel, Hendrik Wiese, Julia Reckfort, Frederike Hanke, Uwe Pietrzyk, Karl Zilles, Katrin Amunts, and Markus Axer. Understanding fiber mixture by simulation in 3D Polarized Light Imaging. *NEUROIMAGE*, 111:464–475, MAY 1 2015.

[20] D. Drenckhahn, K. Akert, and A. Benninghoff. *Anatomie: makroskopische Anatomie, Embryologie und Histologie des Menschen. Niere, Reproduktionsorgane, endokrine Drüsen, Nervensystem, Sinnesorgane, Haut.* Anatomie : Makroskopische Anatomie, Embryologie und Histologie des Menschen. Urban & Schwarzenberg, 1994.

[21] SB Eickhoff, KE Stephan, H Mohlberg, C Grefkes, GR Fink, K Amunts, and K Zilles. A new SPM toolbox for combining probabilistic cytoarchitectonic maps and functional imaging data. *NEUROIMAGE*, 25(4):1325–1335, MAY 1 2005.

[22] Marco Feuerstein, Tim Hauke Heibel, Jose Gardiazabal, Nassir Navab, and Martin Groher. Reconstruction of 3-d histology images by simultaneous deformable registration. In *MICCAI (2)*, volume 6892 of *Lecture Notes in Computer Science*, pages 582–589. Springer, 2011.

[23] M.A. Geday, W. Kaminsky, J.G. Lewis, and A.M. Glazer. Images of absolute retardance l delta n, using the rotating polariser method. *Journal of Microscopy*, 198(1):1–9, 2000. cited By 56.

[24] A. Gerrard and J.M. Burch. *Introduction to Matrix Methods in Optics.* Dover Books on Physics. Dover, 1975.

[25] Nirmalya Ghosh and I. Alex Vitkin. Tissue polarimetry: concepts, challenges, applications, and outlook. *JOURNAL OF BIOMEDICAL OPTICS*, 16(11), NOV 2011.

[26] A.S. Glassner. *An Introduction to Ray Tracing*. Academic Press. Academic Press, 1989.

[27] Ben Glocker, Nikos Komodakis, Georgios Tziritas, Nassir Navab, and Nikos Paragios. Dense image registration through mrfs and efficient linear programming. *Medical image analysis*, 12(6):731–741, December 2008.

[28] G.F. Goethlin. Die Doppelbrechenden Eigenschaften des Nervengewebes - Ihre Ursachen und ihre biologischen Konsequenzen. *Kungl. Svenska Vetenskapsakad. Handl.*, 51:1–92, 1913.

[29] Dennis Goldstein. *Polarized light*. CRC Press Taylor & Francis Group 6000 Broken Sound Parkway NW, Suite 300 Boca Raton, FL 33487-2742, 3rd edition, 2011.

[30] Douglas S. Goodman. *Handbook of Optics - Volume I - Geometrical and Physical Optics, Polarized light, Components and Instruments*, volume 1, chapter 1 GENERAL PRINCIPLES OF GEOMETRIC OPTICS, pages 1.3 – 1.109. The McGraw-Hill companies, 2010.

[31] Alessandra Griffa, Philipp S. Baumann, Jean-Philippe Thiran, and Patric Hagmann. Structural connectomics in brain diseases. *NEUROIMAGE*, 80:515–526, OCT 15 2013.

[32] Thorlabs Inc. Lens tutorial. [`http://www.thorlabs.de/newgrouppage9.cfm?objectgroup_id=8790`; accessed 2016-05-18].

[33] Giacomo Indiveri, Bernabe Linares-Barranco, Robert Legenstein, George Deligeorgis, and Themistoklis Prodromakis. Integration of nanoscale memristor synapses in neuromorphic computing architectures. *NANOTECHNOLOGY*, 24(38, SI), SEP 27 2013.

[34] Johannes D. Johansson. Spectroscopic method for determination of the absorption coefficient in brain tissue. *JOURNAL OF BIOMEDICAL OPTICS*, 15(5), SEP-OCT 2010.

[35] Eric Jones, Travis Oliphant, Pearu Peterson, et al. SciPy: Open source scientific tools for Python, 2001. [`http://www.scipy.org/`; accessed 2016-04-11].

[36] R.C. Jones. A new calculus for the treatment of optical systems I. description and discussion of the calculus. *Journal of the Optical Society of America*, 31(7):488–493, 1941.

[37] B. Kachar. ASYMMETRIC ILLUMINATION CONTRAST - A METHOD OF IMAGE-FORMATION FOR VIDEO LIGHT-MICROSCOPY. *SCIENCE*, 227(4688):766–768, 1985.

[38] K. Kasunic. *Optical Systems Engineering*. McGraw-Hill Education, 2011.

[39] S KAWATA and S MINAMI. THE PRINCIPLE AND APPLICATIONS OF OPTICAL MICROSCOPE TOMOGRAPHY. *ACTA HISTOCHEMICA ET CYTOCHEMICA*, 19(1):73–81, 1986.

[40] S KAWATA, O NAKAMURA, and S MINAMI. OPTICAL MICROSCOPE TOMOGRAPHY .1. SUPPORT CONSTRAINT. *JOURNAL OF THE OPTICAL SOCIETY OF AMERICA A-OPTICS IMAGE SCIENCE AND VISION*, 4(1):292–297, JAN 1987.

[41] R Kimmel. Demosaicing: Image reconstruction from color CCD samples. *IEEE TRANSACTIONS ON IMAGE PROCESSING*, 8(9):1221–1228, SEP 1999.

[42] Melanie Kleiner, Markus Axer, David Graessel, Julia Reckfort, Uwe Pietrzyk, Katrin Amunts, and Timo Dickscheid. Classification of ambiguous nerve fiber orientations in 3d polarizedlight imaging. *Proceeding Medical Image Computing and Computer Assisted Science (MICCAI)*, 7510:206–213, 2012.

[43] H Kluver and E Barrera. A METHOD FOR THE COMBINED STAINING OF CELLS AND FIBERS IN THE NERVOUS SYSTEM. *JOURNAL OF NEUROPATHOLOGY AND EXPERIMENTAL NEUROLOGY*, 12(4):400–403, 1953.

[44] A. Koehler. Ein neues beleuchtungsverfahren fuer mikrophotographische zwecke. *Zeitschrift fuer wissenschaftliche Mikroskopie und fuer mikroskopische Technik*, 10:433–440, 1893.

[45] TG Kolda, RM Lewis, and V Torczon. Optimization by direct search: New perspectives on some classical and modern methods. *SIAM REVIEW*, 45(3):385–482, SEP 2003.

[46] L. Larsen, L. D. Griffin, D. Graessel, O. W. Witte, and H. Axer. Polarized light imaging of white matter architecture. *Microscopy research and technique*, 70(10):851–863, 2007.

[47] Yann LeCun, Yoshua Bengio, and Geoffrey Hinton. Deep learning. *NATURE*, 521(7553):436–444, MAY 28 2015.

[48] Trygve B. Leergaard, Nathan S. White, Alex de Crespigny, Ingeborg Bolstad, Helen D'Arceuil, Jan G. Bjaalie, and Anders M. Dale. Quantitative histological validation of diffusion MRI fiber orientation distributions in the rat brain. *PLoS ONE*, 5(1):e8595, 2010.

[49] M. Levoy, Z. Zhang, and I. Mcdowall. Recording and controlling the 4D light field in a microscope using microlens arrays. *JOURNAL OF MICROSCOPY*, 235(2):144–162, AUG 2009.

[50] Marc Levoy, Ren Ng, Andrew Adams, Matthew Footer, and Mark Horowitz. Light field microscopy. *ACM TRANSACTIONS ON GRAPHICS*, 25(3):924–934, JUL 2006.

[51] NK Logothetis, J Pauls, M Augath, T Trinath, and A Oeltermann. Neurophysiological investigation of the basis of the fMRI signal. *NATURE*, 412(6843):150–157, JUL 12 2001.

[52] Jennifer A. McNab, Saad Jbabdi, Sean C. L. Deoni, Gwenaelle Douaud, Timothy E. J. Behrens, and Karla L. Miller. High resolution diffusion-weighted imaging in fixed human brain using diffusion-weighted steady state free precession. *NEUROIMAGE*, 46(3):775–785, JUL 1 2009.

[53] M. Menzel, K. Michielsen, H. De Raedt, J. Reckfort, K. Amunts, and M. Axer. A jones matrix formalism for simulating three-dimensional polarized light imaging

of brain tissue. *JOURNAL OF THE ROYAL SOCIETY INTERFACE*, 12(111), OCT 6 2015.

[54] JA Nelder and R Mead. A simplex-method for function minimization. *COMPUTER JOURNAL*, 7(4):308–313, 1965.

[55] NIH. Brain initative. http://www.nih.gov/science/brain/, 2013.

[56] R. Oldenbourg. Polarized light field microscopy: An analytical method using a microlens array to simultaneously capture both conoscopic and orthoscopic views of birefringent objects. *Journal of Microscopy*, 231(3):419–432, 2008. cited By 13.

[57] Rudolf Oldenbourg and Michael Shribak. *Handbook of Optics - Volume I - Geometrical and Physical Optics, Polarized light, Components and Instruments*, volume 1, chapter 28 - Microscopes, pages 28.1 – 28.24. The McGraw-Hill companies, 2010.

[58] L.A. Pajdzik and A.M. Glazer. Three-dimensional birefringence imaging with a microscope tilting-stage. i. uniaxial crystals. *Journal of Applied Crystallography*, 39(3):326–337, 2006. cited By 15.

[59] Christoph Palm, Markus Axer, David Graessel, Juergen Dammers, Johannes Lindemeyer, Karl Zilles, Uwe Pietrzyk, and Katrin Amunts. Towards ultra-high resolution fibre tract mapping of the human brain - registration of polarised light images and reorientation of fibre vectors. *FRONTIERS IN HUMAN NEUROSCIENCE*, 4, APR 2010.

[60] G. Paxinos and C. Watson. *The Rat Brain in Stereotaxic Coordinates: Hard Cover Edition*. Elsevier Science, 2006.

[61] M. N. Polyanskiy. Refractive index database. [`http://refractiveindex.infoaccessed2015-08-27`].

[62] J.G. Proakis and D.G. Manolakis. *Digital Signal Processing: Principles, Algorithms, and Applications*. Pearson Prentice Hall, 2007.

[63] Julia Reckfort. *New approaches to the interpretation of 3D-polarized light imaging signals for an advanced extraction of fiber orientation*. Wuppertal, 2015. Verfasserangabe: Julia Reckfort ; Online-Ausg. Reckfort, Julia: New approaches to the interpretation of 3D-polarized light imaging signals for an advanced extraction of fiber orientation ; Wuppertal, Univ., Diss., 2015 ; Quelldatenbank: SEARCH_UBWU-x ; Format:marcform: print ; Umfang: VIII, 179 S. : Ill., graph. Darst.

[64] Julia Reckfort, Hendrik Wiese, Uwe Pietrzyk, Karl Zilles, Katrin Amunts, and Markus Axer. A multiscale approach for the reconstruction of the fiber architecture of the human brain based on 3D-PLI. *FRONTIERS IN NEUROANATOMY*, 9, SEP 3 2015.

[65] HH Rosenbrock. AN AUTOMATIC METHOD FOR FINDING THE GREATEST OR LEAST VALUE OF A FUNCTION. *COMPUTER JOURNAL*, 3(3):175–184, 1960.

[66] Juergen Schmidhuber. Deep learning in neural networks: An overview. *NEURAL NETWORKS*, 61:85–117, JAN 2015.

[67] W.J. Schmidt. Zur Doppelbrechung des Nervenmarks. *Zeitschrift fuer wissenschaftliche Mikroskopie und mikroskopische Technik*, 41:29–38, 1923.

[68] F.O. Schmitt and R.S. Bear. The optical properties of vertebrate nerve axons as related to fiber size. *Journal of Cellular and Comparative Physiology*, 9(2):261–273, 1937.

[69] Martin Schober, Philipp Schloemer, Markus Cremer, Hartmut Mohlberg, Anh-Minh Huynh, Nicole Schubert, Karl Zilles, and Katrin Amunts. How to generate a reference volume for subsequent 3d-reconstruction of histological sections. *Proceeding BVM*, 2015.

[70] M Shribak and R Oldenbourg. Mapping polymer birefringence in three-dimensions using a polarizing microscope with oblique illumination. In Anselmetti, D, editor, *BIOPHOTONICS MICRO-AND NANO-IMAGING*, volume 5462 of *PROCEEDINGS OF THE SOCIETY OF PHOTO-OPTICAL INSTRUMENTATION ENGINEERS (SPIE)*, pages 57–67. SPIE, 2004. Conference on Biophotonics Micro-and Nano-Imaging, Strasbourg, FRANCE, APR 28, 2004.

[71] Olaf Sporns, Giulio Tononi, and Rolf Koetter. The human connectome: A structural description of the human brain. *PLoS Computational Biology*, 1(4), 09 2005.

[72] H. J. C. M. Sterenborg, M. J. C. Van Gemert, W. Kamphorst, J. G. Wolbers, and W. Hogervorst. The spectral dependence of the optical properties of human brain. *Lasers in Medical Science*, 4:221–227, 1989,.

[73] D. S. Tuch, T. G. Reese, M. R. Wiegell, N. Makris, J. W. Belliveau, and J. Van Wedeen. High angular resolution diffusion imaging reveals intravoxel white matter fiber heterogeneity. *Magnetic Resonance in Medicine*, 48(4):577–582, 2002.

[74] DS Tuch. Q-Ball imaging. *MAGNETIC RESONANCE IN MEDICINE*, 52(6):1358–1372, DEC 2004.

[75] Kamil Ugurbil, Junqian Xu, Edward J. Auerbach, Steen Moeller, An T. Vu, Julio M. Duarte-Carvajalino, Christophe Lenglet, Xiaoping Wu, Sebastian Schmitter, Pierre Francois Van de Moortele, John Strupp, Guillermo Sapiro, Federico De Martino, Dingxin Wang, Noam Harel, Michael Garwood, Liyong Chen, David A. Feinberg, Stephen M. Smith, Karla L. Miller, Stamatios N. Sotiropoulos, Saad Jbabdi, Jesper L. R. Andersson, Timothy E. J. Behrens, Matthew F. Glasser, David C. Van Essen, Essa Yacoub, and WU-Minn HCP Consortium. Pushing spatial and temporal resolution for functional and diffusion MRI in the Human Connectome Project. *NEUROIMAGE*, 80:80–104, OCT 15 2013.

[76] H. Wiese, D. Graessel, U. Pietrzyk, K. Amunts, and M. Axer. Polarized light imaging of the human brain: A new approach to the data analysis of tilted sections. volume 9099, 2014.

[77] John R. Willison. *Handbook of Optics - Volume I - Geometrical and Physical Optics, Polarized light, Components and Instruments*, volume 1, chapter 18 SIGNAL DETECTION AND ANALYSIS, pages 18.1 – 18.16. The McGraw-Hill companies, 2010.

[78] Margarete Wolecke. Eine neue Method der Markscheidenfaerbung. *Journal fuer Psychologie und Neurologie*, 51:199–204, 1942.

[79] JR Wolpaw, N Birbaumer, DJ McFarland, G Pfurtscheller, and TM Vaughan. Brain-computer interfaces for communication and control. *CLINICAL NEUROPHYSIOLOGY*, 113(6):767–791, JUN 2002.

[80] J. Joshua Yang, Dmitri B. Strukov, and Duncan R. Stewart. Memristive devices for computing. *NATURE NANOTECHNOLOGY*, 8(1):13–24, JAN 2013.

[81] Karl Zilles and Katrin Amunts. Receptor mapping: architecture of the human cerebral cortex. *CURRENT OPINION IN NEUROLOGY*, 22(4):331–339, AUG 2009.